FREQUENCY CONTENT IN THE WAKES OF ROTATING BLUFF BODY HELICOPTER HUB MODELS

By

CHRISTOPHER E. PETRIN

BACHELORS OF SCIENCE IN AEROSPACE ENGINEERING
Oklahoma State University
Stillwater, Ok
2015

Submitted to the Faculty of the
Graduate College of
Oklahoma State University
in partial fulfillment of
the requirements for
the Degree of
MASTER OF SCIENCE
JULY, 2017

FREQUENCY CONTENT IN THE WAKES OF ROTATING BLUFF BODY HELICOPTER HUB MODELS

Thesis Approved:

Dr. Brian Elbing

Thesis Advisor

Dr. Jamey Jacob

Dr. Kurt Rouser

ACKNOWLEDGEMENTS

I would like to thank my family, and, in particular, my parents, who have supported me in the stressful and difficult undertaking that is graduate school. I know that I would not have made it far without their love, trust, and care. I would also like to thank all of my friends and colleagues, but particularly Matt and Sam Robertson and Nathan Poulos for encouragement and commiserating during the hard times. Next, a special thanks to my advisor, Dr. Elbing, who has provided a truly immeasurable amount of wisdom, guidance, and patience over the past two years. I also thank Dr. Jacob, Dr. Santhanakrishnan, and Dr. Rouser for their aid in developing this thesis and their service on my committee, and Dr. Arena for his encouragement and loaning of critical components to this work. I am grateful to Jacob Niles for his timely work in printing the fairing, and to all the staff at the DML who aided me in fabrication of the hub models and to David Reich for his initial help in familiarizing me with this problem. Finally, I thank God for giving me energy and peace of mind, and I pray that this work will somehow bring glory to Him.

Acknowledgements reflect the views of the author and are not endorsed by committee members or Oklahoma State University.

Name: Christopher E. Petrin

Date of Degree: JULY, 2017

Title of Study: FREQUENCY CONTENT IN THE WAKES OF ROTATING BLUFF BODY HELICOPTER HUB MODELS

Major Field: Mechanical and Aerospace Engineering

It is estimated that the rotor hub of a helicopter is responsible for up to 30% of the parasite drag of a helicopter. This is because the hub is a group of rotating bluff-body shapes exposed to high-velocity flow, which may produce hub revolution-dependent flow structures in the hub wake. These structures also interact with a helicopters empennage and tail rotor, negatively impacting stability and performance. While some specific helicopter hubs have been studied, no study of a generalized hub shape has taken place. Because the hubs that have been studies are very geometrically complex, computational prediction of hub flow physics is not yet mature enough to be of use to industry. The objective of this study is to characterize the long-age wake of a geometrically simple configuration of canonical bluff bodies to model a helicopter hub. Three scale models were examined, each with four larger arms to represent rotor blade shanks and two smaller arms to represent scissor links. The models were identical in dimension, but one had a smoother arm profile and another had a variation in phase angle between the two sets of arms. The models were mounted in the Experimental Flow Physics Laboratory Large Water Tunnel, and tested at a hub diameter-based Reynolds number of 7.6×10^5. Time-resolved velocity measurements were taken 14 hub radii downstream of one model, while phase-averaged velocity measurements were taken 7 hub radii downstream of the other two. Similar trends to previous works were observed, including two-per-hub revolution, four-per-hub revolution, and 6-per-hub revolution frequency content in the velocity spectra. This study therefore aids in the uncovering of fundamental flow physics of rotor hubs, creating a baseline case to which further parametric variations may be compared.

TABLE OF CONTENTS

LIST OF TABLES

LIST OF FIGURES

Figure Page

NOMENCLATURE

Variables

Re_L	Reynolds number based on L
Ma	Mach number
μ_L	Advance ratio based on L
St	Strouhal number
L	Generic characteristic length scale
d	Hub diameter
l	Chord of profile
Re_d	Hub diameter-based Reynolds number
Re_l	Profile chord-based Reynolds number
Re_{hub}	Hub diameter-based Reynolds number
R	Rotor blade radius
b	Profile thickness
U	Generic characteristic velocity scale, or freestream velocity
U_∞	Freestream velocity (same as above)
f	Generic characteristic frequency, (Hz)
c	Speed of sound in fluid
ν	Fluid kinematic viscosity
Ω	Hub rotation rate, (rad/s)
x	Streamwise coordinate
y	Vertical coordinate, defined from the rotor blade shank location
r	Hub radius

μ_R	Rotor blade tip-based advance ratio
dt	Input lag
n	Input phase increment number
f_{hub}	Hub revolutional frequency, (Hz)
ψ	Phase increment, (°)
h	Distance between rotor shanks and scissor links
δx	Generic distance difference
δt	Generic time difference
U_c	Convection veolcity
u'	Turbulent fluctuating velocity
dx	Vector distance spacing
ω	Frequency (1/s)
k	Wavenumber (1/m)
$S_{uu}(\omega)$	Single-sided frequency domain spectra (example units: m^2/s)
$S_{uu}(k)$	Single-sided wavenumber domain spectra (example units: m^3/s^2)
$(\quad)_{FS}$	Subscript indicates full-scale parameter

Abbreviations

OSU	Oklahoma State University
EFPL	Experimental Flow Physics Laboratory
EFPL-LWT	Experimental Flow Physics Laboratory - Large Water Tunnel
PSU	The Pennsylvania State University
ARL	Applied Research Laboratory
GTWT	Garfield Thomas Water tunnel
LDV	Laser Doppler Velocimetry
PIV	Particle Image Velocimetry
sPIV	Stereo Particle Image Velocimetry

FFT	Fast Fourier Transform
SLA	Stereolithograph(y/ic)

CHAPTER 1

INTRODUCTION

1.1 Motivation

The flow around helicopter hubs has been recognized as problematic for at least 40 years. This is because a rotor hub is a complex configuration of rotating, interacting bluff-body shapes which produces an oscillating turbulent wake. The problem of the rotor hub flow may be loosely categorized into two areas: drag and stability/control. As a rotor hub is composed of bluff bodies, pressure drag due to flow separation over the bluff bodies is the dominant form of drag. For single-rotor hub aircraft, the hub geometry was identified by Keys & Wiesner (1975, [1]) to be responsible for 20% to 30% of the total drag of the aircraft through compilation of available wind tunnel tests and analytical studies of a multitude of helicopters, with a focus on Boeing aircraft. Sheehy (1977, [2]) came to the same conclusion after revising and expanding the previous compilation to more accurately reflect Sikorsky helicopters. Rabbott & Stroub (1975, [3]) estimated that if the hub drag could be reduced by 50% for a third of the civilian helicopter fleet that fuel cost could be reduced by 10% across the entire civlian fleet using a similar compilation of available drag data along with estimates of fleet composition and other aircraft parameters. In addition to the drag on the hub, the wake of the hub is composed of separated flow structures that impact the tail. This impact is known to negatively affect both the stability and structural safety of the helicopter (Roesch & Dequin, 1985, [4]). As a result, several long-age wake studies have been undertaken to attempt to characterize the wake behind various rotor hubs. A selection of some particularly relevant wake studies is discussed in detail in the

literature review in Section 1.3.1. As a note, the term 'long-age,' is used to indicate the wake near to and beyond the location of the fin and empennage assembly on helicopters. Since the drag and unsteady wake of rotor hubs are both important, it is therefore necessary that both be better predicted to create more optimized rotor hub designs.

However, quantitative physical prediction of hub drag and wake flow behind rotor hubs still falls short, and causes costly delays in the helicopter design process. While industry has been able to use a variety computational fluid dynamics (CFD) solvers to predict the magnitude of steady (average) drag of non-rotating hubs to about 10% (Bridgeman & Lancaster, 2010, [5]; Dombroski & Egolf, 2012, [6]), such solvers have yet to match the unsteady drag frequency content observed experimentally. Academic efforts have been more successful using generic hub geometry, and have been able to detect many of the important frequencies in the unsteady hub drag, but are still working towards accurate predictions for the amplitudes of said frequency content (Shenoy et al., 2013, [7]). In terms of unsteady wake velocity fluctuations, the same has proven true; while peaks in most of the important frequencies are detected, the amplitude predictions of those predictions are incorrect (Raghav et al., 2013, [8]). In order to better contribute to helicopter design, comptuational models will have to resolve both the unsteady drag and wake frequency components.

Validation of computational models relies on comparison with experimental results. Focusing on the wake, various wake studies have been conducted thus far, as previously mentioned. These studies have used a variety of flow measurement techniques (hot film anemometry, laser doppler velocimetry, etc.). However, all of these studies have been focused on geometric configurations very similar to hub and fuselage geometry of specific commercial helicopters. While this is entirely reasonable for design evaluation, it can limit the scope of conclusions drawn from such experiments. For example, a 4-per-hub-revolution ('4/rev') oscillation in velocity is always observed

in the wake of a four bladed hub (regardless of whether the blades have been attached or not). This 4/rev oscillation has been tied to the passage of the rotor blade shank, the arms of the hub to which the rotor blades are attached. For a commercial helicopter hub, it is difficult to know whether the strength of the 4/rev oscillation in the wake is due to the overall size and profile of the blade shanks, their location relative to the other hub components, or their particular mechanical design (location and size of bolts, holes, and other subcomponents on the blade shank). Additionally, a more complex hub increases the computational expense of CFD modeling, forcing devotion of more grid resolution to the hub as opposed to resolving the wake. For example, in Dombroski & Egolf (2012, [6]), a total of about 15 million cells were used to model the flow around a Sikorsky S-92 rotor hub, 8.2 million of which were devoted to surface and boundary layer modeling of the complex hub geometry. Thus, performing experiments and computational evaluation using specific commercial geometry, which is necessary for the design process, can obscure the underlying flow physics responsible for the major frequency content. Therefore, the purpose of the current work is to provide a characterization of the long-age wake behind a geometrically simple and generic hub composed of canonical bluff body shapes, in which the consistent frequency content of previous results (2-per-hub-revolution and 4-per-hub-revolution oscillations) is observed. This characterization can then be used as a baseline for future comparison of parametric variations. By using simple models, a more fundamental understanding of the underlying fluid mechanics of the rotor hub wake may be developed and some insight into previous wake studies can be offered.

1.2 Terminology and Scaling Parameters

Before proceeding to a discussion of previous wake studies and an overview of bluff body aerodynamics, it is first necessary to discuss the terminology that will be used in describing helicopter rotor hubs and their wakes, and to define some common scaling

parameters.

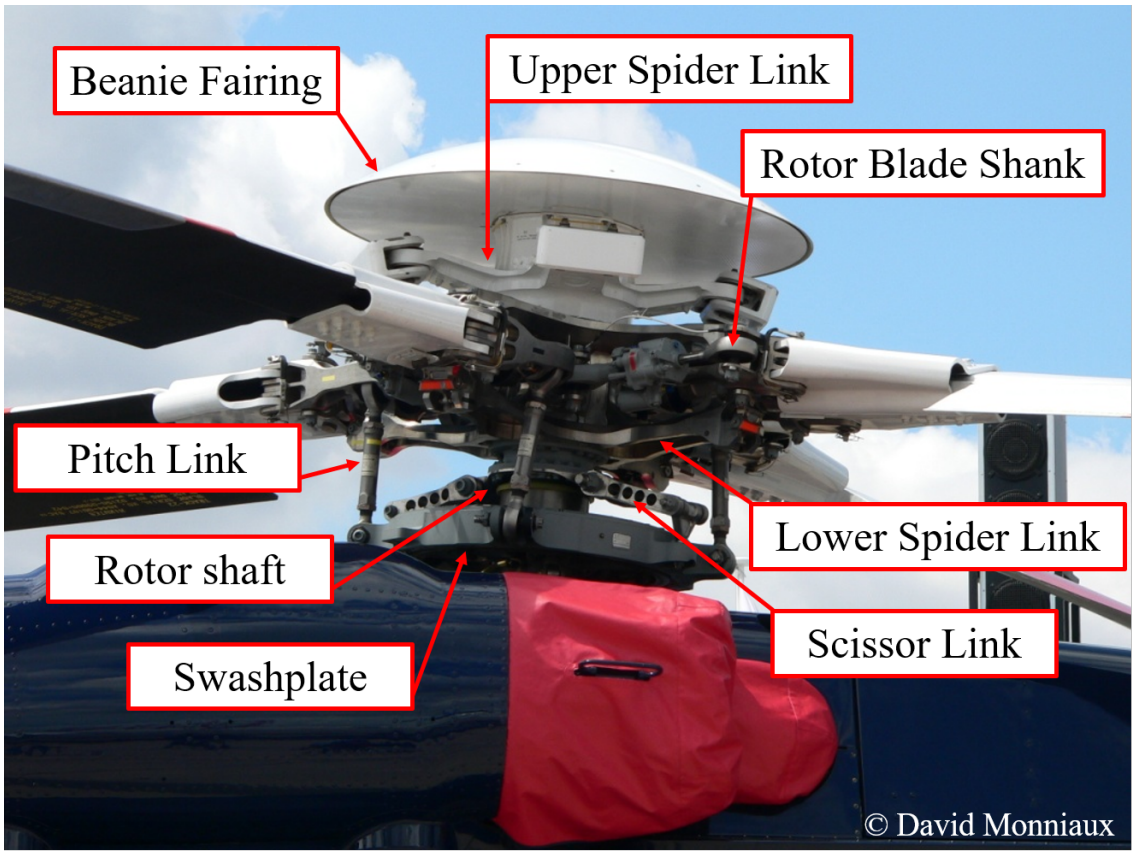

Figure 1.1: A typical four-bladed hub with important geometric features labeled. (Unlabeled image reproduced under Creative Commons ASA 4.0 license)

To assist in defining the geometry of a helicopter rotor hub, Figure 1.1 shows a four-bladed hub with important features labeled. For consistency, a four-bladed helicopter is used as the reference case in the current work; other helicopters will have similar features, but the number-per-hub may vary. This same hub was used as a test case by researchers at the Pennsylvania State University, as will be discussed in the review of wake studies. Beginning with the base hub component, the 'swashplate,' is used to control the tilt of the hub relative to the fuselage. It typically occurs once on a four-bladed hub, though there are double-swashplate designs in which a lower and upper swashplate exist. The swashplate is mounted around the 'rotor shaft,'

which may also be called the 'mast,' and connected to it using 'scissor links.' For a single hub, only one rotor shaft is used, while there are typically two scissor links on a four-bladed hub. Mounted on top of the rotor shaft are the 'rotor blade shanks'; these are the parts of the hub geometry to which the rotor blades are connected, often by bolts or screws. These may also be interchangably referred to as 'rotor blade stubs,' 'blade grips,' and the 'main hub arms.' For a four-bladed helicopter, they appear four times on the hub. On this hub, two sets of 'spider links,' are used to fix the blade shanks to the hub. Each set of the spider links (upper and lower) has four arms - one for each blade shank. To control the pitch of the rotor blades, a set of 'pitch links,' connects the blade shanks to the swashplate; for this hub there is a pitch link for each rotor blade. Finally, a single 'beanie fairing,' is mounted to the top of the rotor mast, above the upper spider links. A breakdown of the number of appearances on the hub of each hub component is shown in Table 1.1.

Component	# / hub
Swashplate	1
Rotor shaft	1
Scissor link	2
Pitch link	4
Blade shank	4
Lower spider link	4
Upper spider link	4
Beanie Fairing (not always present)	1

Table 1.1: The number of components-per-hub for a typical four-bladed helicopter rotor hub.

In the discussion of rotor hub wakes, three separate flow regimes are typically identified, based upon their respective distances downstream of the hub. These regimes are defined using the hub radius as a basis, rather than an absolute downstream distance. The 'near-wake,' is the wake closest to the rotor hub, and is the range of distances from one hub radius to three hub radii downstream. The 'far-wake,' also

called the 'long-age wake,' is the wake corresponding roughly to the location of the helicopter tail, usually six to nine hub radii downstream. Finally, the 'mid-wake,' designates the distances in between the far-wake and near-wake (three hub radii to six hub radii downstream).

Finally, rotor hub flow is often characterized by a set of three common nondimensional parameters: Reynolds number (Re), Mach number (Ma) and advance ratio (μ). An additional nondimensional parameter, the Strouhal number (St) is often used in discussion of bluff body flow. All are shown below. Note that L denotes a generic characteristic length scale. For rotor hub Reynolds numbers, this is often either the diameter of the hub (d) or the chord of local components (l). The respective Reynolds numbers are then denoted as Re_d and Re_l, though the hub diameter-based Reynolds number is also often denoted by Re_{hub}. For circular cylinders, the chord is equal to the diameter of the cylinder. However, it is still denoted by Re_l in this work to avoid confusion with the hub diameter-based Reynolds number. For the advance ratio, this length is the rotor blade radius, R, regardless of whether the rotor blades are attached. For bluff body Strouhal numbers, the length scale is almost always the thickness of the profile, b. For circular cylinders, this thickness is equal to the diameter of the cylinder. Similarly to L, U is a generic velocity scale. For rotor hub, this velocity scale is assumed to be the average freestream streamwise flow speed, U_∞, and in the current work, the two are used interchangably. However, for bluff body flow, U is equal to the relative velocity, U_{rel} at the location of the profile of interest. This resolves the rotating components with their speed relative to the freestream speed. The definition of the relative velocity is shown below; for the advancing side, the rotational speed component is added, while it is subtracted for the retreatig side (here r is the radial coordinate of the component, not the hub radius). Finally, for the Strouhal number, f is a generic characteristic frequency. For bluff body flows, the dominant frequency in the wake is often used. Other parameters here are fluid or

hub specific: c is the fluid's speed of sound, ν is the fluid's kinematic viscosity, while Ω is the rotation rate of the hub in rad/s.

$$Re_L \equiv \frac{UL}{\nu} \tag{1.1}$$

$$Ma \equiv \frac{U}{c} \tag{1.2}$$

$$\mu_L \equiv \frac{U}{\Omega L} \tag{1.3}$$

$$St \equiv \frac{fL}{U} \tag{1.4}$$

$$U_{rel} \equiv U_\infty \pm \Omega r \tag{1.5}$$

1.3 Literature Review & Bluff Body Theoretical Background

1.3.1 Helicopter Rotor Wake Studies

As the focus of the current work is on characterization of the far wake, only directly relevant wake studies (those observing velocity content of the long-age wake) are discussed here. For a comprehensive review of previous works on helicopter rotor hub drag, wake flow physics, the wake's impact on aircraft stability, and the state of computational modelling, refer to Reich et al. (2016, [9]). As the direct precursor to the current work, an emphasis is placed on research conducted at the Pennsylvania State University (PSU) Applied Research Laboratory (ARL).

Roesch & Dequin (1985, [4]) noted that when the empennage or tail rotor are caught in the wake of the fuselage or the hub of the helicopter, the pitch and yaw stability are decreased, and the stabilizers become less effective due to pressure loss in the wake. Tail shake, structural vibrations associated with the hub wake impinging

on the tail, may also be amplified if the the wake contains vortices with oscillation frequencies near that of the natural frequencies of the empennage assembly. To gain a better insight into the hub wake, Roesch & Dequin [4] conducted a wind tunnel flow visualization campaign using a 1/7th scale, four-blade helicopter hub mounted to the top of a scaled Aérospatiale SA 355 Écureuil 2 fuselage. The rotor blades were not mounted, presumably because they would complicate flow visualization, under the assumption that the blades would not greatly modify the structure of the wake. Preliminary pressure measurements showed that the blades deflected the wake downwards and in the opposite lateral direction to that of the blade's trajectory. The minimum and maximum hub diameter-based Reynolds numbers were 1×10^5 to $\sim 4 \times 10^5$ (roughly 1/10th of that of the full-scale helicopter), with free-stream speeds varying between 10 m/s and 30 m/s. Advance ratio was varied from 0.1 to 0.4. After conducting flow visualization of the wake, the root bending stresses of the stabilizer were measured, while hot film anemometry was used to measure the velocity spectra in the hub wake. Flow visualization revealed large turbulent structures propagating downstream from the hub. These structures occured due to the passage of the the bare blade shanks (the four large arms used to bolt to the rotor blades to the hub) and were noted to convect towards the tail. A sample of these structures is shown in Figure 1.2. Comparing the measured bending stresses to the velocity spectra of the wake, the fluctuating bending moments of the stabilizer were noted to be strongly correlated to the wake fluctuations. In addition to the dominant spectra identified at the blade-passage frequency (4/rev for a four-blade assembly), a slightly weaker 2/rev signal was also observed. Because the 4/rev frequency was due to a 4-per-hub geometry, the 2/rev frequency was attributed to the scissor link geometry, the most prominent 2-per-hub geometry. While providing useful qualitative observations, the quantitative measurement of frequency content in the actual wake was limited to a single hot-film location.

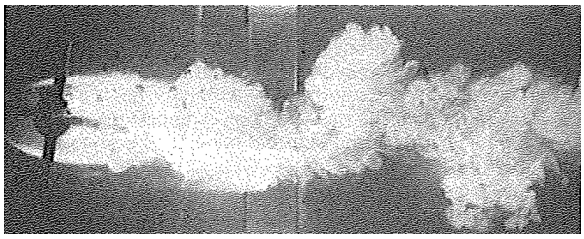

Figure 1.2: Top view of flow visualization of a 1/7th scale helicopter hub, showing a snapshot of oscillatory flow structures propagating downstream from the hub (flow is left to right, the hub is the black cross at the far left). From [4].

As mentioned, a limitation of the previous study was the lack of spatial resolution of the wake. To amend this, Berry (1997, [10]) used laser doppler velocimetry (LDV) to examine the turbulence downstream of a hub, with the intention of improving fuselage drag modeling. The US Army 2-Meter Rotor Test System (2MRTS) was used mounted on a generic helicopter fuselage in a wind tunnel. The 2MRTS is a four-bladed test hub with two rotating scissor links, described in detail in Phelps & Berry (1987, [11]). For this experiment, the rotor blades were attached. The measurements were taken using a grid of over 200 points located downstream of the hub, both above and below the rotor blade plane and on either lateral side of the center plane. The model was roughly 1/5th scale, and the advance ratio of the hub was set to 0.23, with a free-stream speed of 42.67 m/s. The hub diameter-based Reynolds number of the test was 1.1×10^6. Close to the hub (less than half of the diameter of the rotor), an unexpectedly strong 2/rev component was observed in the wake. At distances beyond half of the diameter of the rotor, the expected 4/rev component exceeded the 2/rev content. Unlike Roesch & Dequin (1985, [4]), Berry (1997, [10]) attributed the 2/rev frequency content to interactions between the hub and the fuselage, because the structures appeared near the fuselage, though acknowledged no detailed explanation. As with previous studies, the turbulent structures were persistant far downstream, but no measurements were taken as far downstream as the tail assembly.

In both wake studies discussed so far, an unexpected and strong 2/rev oscillation in the wake was found in the wakes of hubs mounted to helicopter fuselages. The cause of the 2/rev, however, was loosely attributed to different sources: Roesch & Dequin (1985, [4]) thought it to be due to the passage of the scissor links, a 2-per-hub geometry, while Berry (1997, [10]) conjectured that it was the result of fuselage-pylon-wake interactions. Because the presence and strength of the 2/rev oscillation must be able to be predicted for an optimal helicopter design process, Reich et al. (2014, [12]) conducted the highest hub diameter-based Reynolds number experiments yet, using a 1:4.25 scale model of commercial helicopter hub. These results were compared to computational results from the wake of a different hub in Reich et al. (2014, [13]). The model hub was mounted in the Garfield Thomas Water Tunnel (GTWT) at the Pennsylvania State University (PSU) Applied Research Laboratory (ARL); a water tunnel had not been used before for study of rotorcraft aerodynamics, due to compressibility effects at the tips of rotor blades. However, the rotor blades were neglected as in Roesch & Dequin (1985, [4]), leaving only the hub. The commercial hub the model was based on has a maximum Mach number of 0.18, meaning incompressibility could be assumed (incompressible flow is generally valid for $Ma < 0.3$). Thus, the GTWT, which has a 48 inch diameter test section, was used, as it is capable of providing freestream velocities necessary for full-scale hub-diameter based Reynolds numbers. The model hub had four blade shanks and two scissor links, which were set roughly 30° out of phase with the blade shanks, and a total diameter of 24 inches. The model hub was made using a rapid prototyping, 3D-printing technique called stereolithography (SLA), which had the added benefit of allowing the model to be easily defeatured. That is, the small features of the hub components (e.g. screws, bolts, holes, etc.) were ignored in the model design such that the end product mimicked the overall profiles and shapes of the hub components, thereby removing the small-scale complexity of the hub while retaining the shape of the larger components (as outlined

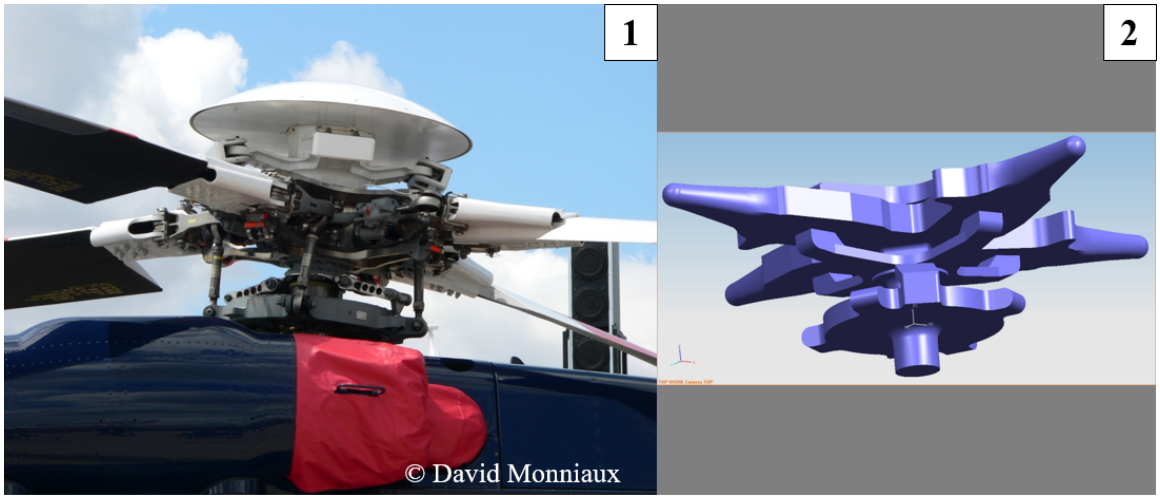

Figure 1.3: 1 (left): The commercial hub upon which PSU 24-inch model was based, shown with rotor blades attached (Image reproduced under Creative Commons ASA 4.0 license). 2 (right): A computer rendering of the 'defeatured' PSU 24-inch model, provided by authors of [12]. Defeaturing involved removing the small scale complexity of the hub while keeping the overall shape and wetted surface area nearly the same.

previously in Section 1.2). This was done to determine if the large-scale hub geometry was responsible for the 2/rev oscillation. An illustration of the initial hub and final model is shown in 1.3 Additionally, the hub was mounted to a straight, untapered NACA 0025 fairing rather than a fuselage, though this was done to protect the wake from interference of flow shedding from the rotor shaft. More detailed design of these experiments may be found in Reich (2013, [14]). As shorthand, the experiments & results discussed here may be referred to as 'PSU 24-inch experiments/results,' due to the hub diameter of the model.

The hub was operated at two hub diameter-based Reynolds numbers: $\sim 2.5 \times 10^6$ and $\sim 4.9 \times 10^6$, which correspond foughly to full-scale hub diameter-based Reynolds numbers for small (e.g. Hughes OH-6 Cayuse, Robinson R44) and medium sized helicopters (e.g. Bell 412, Aérospatiale SA 355 Écureuil 2), but only 1/3rd and 2/3rd of the scale for large helicopters (e.g. Sikorsky S-92), respectively. These

corresponded to freestream speeds of 3.25 m/s and 6.50 m/s, and an illustration of the test conditions of the PSU 24-inch model experiments compared to hub diameter-based Reynolds numbers of common helicopters is shown in Figure 1.4. While the GTWT was capable of providing flow speeds for a hub diameter-based Reynolds number of $\sim 7.4 \times 10^6$, the full-scale hub diameter-based Reynolds number of a large helicopter, the model was predicted to undergo failure at that condition due to the use of SLA material. Therefore, this condition was not tested. The advance ratio was set to 0.2 for all operating conditions, and the hub was pitched to a nominal angle of 5° to represent forward flight conditions. Two-dimensional streamwise-vertical plane wake measurements were taken using hub phase-averaged two-dimensional particle image velocimetry (PIV), and three-dimensional wake measurements were taken using LDV and stereo particle image velocimetry (sPIV), with the image plane aligned in the spanwise-vertical direction. Quantitative optical methods like traditional (2D) PIV and stereo PIV have the benefit of increased spatial resolution over the resolution of LDV; that is, optical methods can be used to measure more points to form a larger view of the wake. However, quantitative optical methods rely on cross-corellation of multi-pixel interrogation windows, and thus have a lower point-wise resolution than LDV. Therefore LDV is better able to assess fine-scale turbulent statistics. Unsteady drag measurements were taken on the hub using a button load cell mounted next to the shaft. Not all wake measurement techniques were used at all locations. The measurement locations were scaled according to hub diameter, and were situated roughly two hub radii downstream ('near-wake'), four hub radii downstream ('mid-wake'), and seven hub radii downstream ('far-wake,' also called the long-age wake), which was assumed to be the approximate location of the tail for any given helicopter. In the near-wake measurement, LDV and streamwise 2D PIV were used, while at the mid-wake, only LDV data were acquired. Finally, at the long-age wake location, seven hub radii downstream of the hub, all three techniques were used. As a point

of clarification, the 2D PIV image planes were centered along the same plane as the fairing. A schematic of the test locations and the measurements used is found in Figure 1.5.

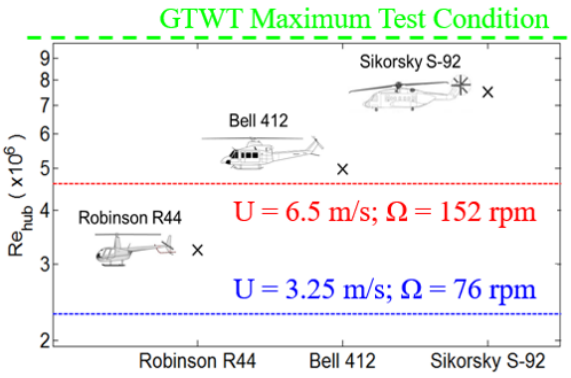

Figure 1.4: Hub diameter-based Reynolds number range of various helicopters. Sampled helicopters taken as representative for helicopters of similar size and speed. The hub diameter-based Reynolds number test conditions of PSU 24-inch model are shown by blue ($Re_{hub} = 2.5 \times 10^6$) and red ($Re_{hub} = 4.9 \times 10^6$). Figure provided by authors of [12].

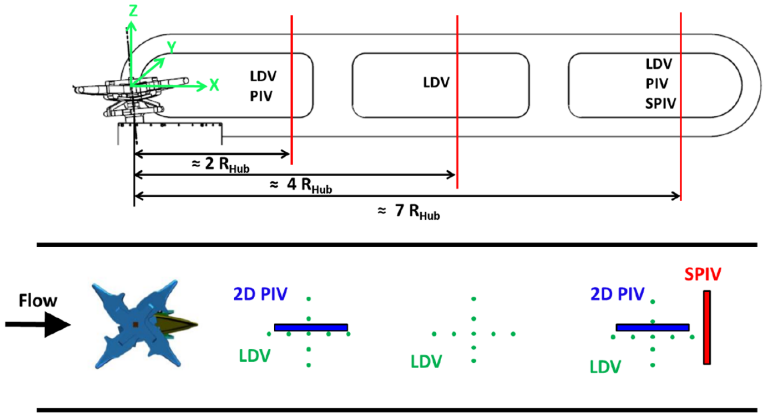

Figure 1.5: Schematic of the test locations and the wake measurements used at those locations in PSU 24-inch experiments. Flow is left to right. Figure is a compilation of two subfigures provided by author of [12].

The 2/rev and 4/rev oscillation frequencies reported by Roesch & Dequin (1985, [4]) and Berry (1997, [10]) in the wake were confirmed using the PSU 24-inch model (Reich et al., 2014, [12]). Near-wake and far-wake PIV harmonics are shown in Figure 1.6, compared to harmonics from preliminary CFD by the same authors. In the near-wake (2 hub radii downstream), the 2/rev oscillations were just as strong as the 4/rev at vertical locations around just above that of the scissor links (Position 2 in Fig. 1.6), becoming weaker above and below that height.

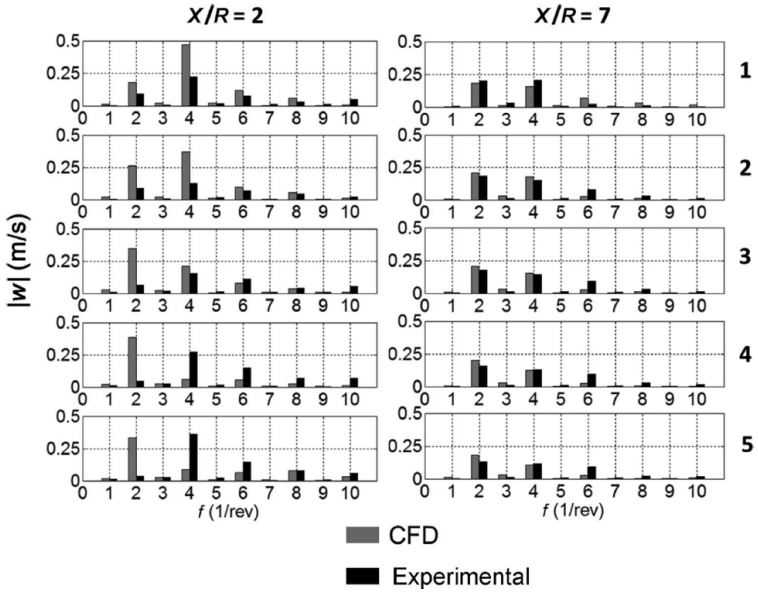

Figure 1.6: Near-wake ("$X/R = 2$", left) and far-wake ("$X/R = 7$", right) 2D-PIV vertical velocity harmonics from [12]. Grey denotes preliminary CFD results, while black denotes experimental results. The test condition for both was $Re_h ub = 4.9 \times 10^6$. The numbers on the far right (1 through 5) indicate probe position, and correspond to hub heights. Position 1 indicates a vertical location at the center of the rotor arm height, while Position 5 us the approximate height of the swashplate. The scissor link geometry is located between Position 3 and Position 4. Note that Z and w are used to describe the vertical coordinate and vertical velocity, while the current work uses y and v to describe the same.

Of note, in the far wake (∼7 hub radii downstream), the 2/rev signal was stronger than that of the 4/rev in all locations aside from the most extreme heights. This was taken as an indicator that the different structures decay at different rates. Additionally, the relative strengths of the fluctuations displayed a 'flip' through the height profiles; that is, looking at locations that were above or below the height of the hub (i.e. not directly behind the hub), the 4/rev was stronger than the 2/rev. Looking at heights directly behind the hub, the 2/rev fluctuation was the stronger component. With no fuselage model and the hub geometry simplified to concentrate on the largest scale of the geometry, it was concluded that both 2/rev and 4/rev flow structures were due to vortex shedding from 2-per-hub and 4-per hub geometry (the scissor links and rotor blade shanks, respectively), and not complex fuselage-pylon-wake interactions (Reich et al., 2014, [12]). To reiterate, these frequencies of wake oscillation were observed with all measurement techniques used (hub drag, PIV, sPIV, LDV). In addition to fluctuations in vertical velocity that were shown in PIV data, LDV data also showed these frequencies to be present in the streamwise direction. However, no vertical spatial distribution of frequency content was discussed for any measurement other than the 2D PIV. Because these two frequencies of wake oscillations have been consistently seen in rotor hub wake studies, and because the amplitude flipping between the two frequencies was observed in the highest hub diameter-based Reynolds number data yet collected, observation of trends similar to these was taken as the objective of the current work. A sample phase pseudo-spatially-resolved panorama of the vertical velocity from PIV measurements taken at the near-wake and far-wake measurement locations behind the PSU 24-inch model is shown in Figure 1.7. The creation of panoramas like this is detailed in the Results section of the current work.

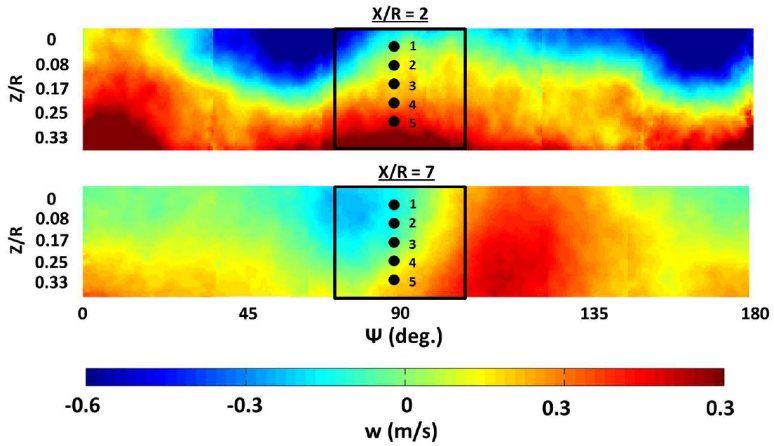

Figure 1.7: Near-wake ("$X/R = 2$", top) and far-wake ("$X/R = 7$", bottom) 2D-PIV vertical velocity phase panoramas from the PSU 24-inch tests [12]. Flow is left to right. This figure shows vertical flow structures that have been shed at various hub phases from 0∘ to 180°. The numbered dots describe the probe positions discussed in the caption of Fig. 1.6. Note that Z and w are used to describe the vertical coordinate and vertical velocity, while the current work uses y and v to describe the same. Also note that the vertical distance is scaled to the hub radius, R.

Finally, a definite 6/rev fluctuation was observed at all locations in the PIV and LDV, as well as in the hub drag measurement. Unlike the 4/rev and 2/rev fluctuations, which have a direct geometrical counterpart on the hub (the blade shanks/grips and scissor links, respectively), the 6/rev component has no geometric basis on the hub. The 6/rev was hypothesized to be due to Strouhal shedding from the spider link geometry of the hub. With an assumed Strouhal number of 0.14 for a 'square cylinder' (i.e. a square prism - see Section 1.3.2 for discussion of bluff body terminology), a 6/rev fluctuation corresponded to a characteristic length of 4.1 cm. The geometry that closest matched that length was the chord of the lower spider link (a 4-per-hub component), which was 3.8 cm (corresponding to $St = 0.13$). However, this explanation of the 6/rev fluctuation was viewed as hypothetical conjecture (Reich et

al., 2016, [9]) and is therefore still an active question.

In Reich et al. (2015, [15]), the dependence of the wake structures on Reynolds number and advance ratio were examined, along with several geometric variations for studied for drag reduction. The same geometry tested previously was scaled further down from a 1:4.25 model to a 1:17 scale model, producing a model with a diameter of about 6 inches. This was done in order to place the hub in the ARL PSU 12-inch diameter water tunnel. Additionally, the model was machined from stainless steel unlike the previous rapid-prototyped SLA model. The hub diameter-based Reynolds number was varied between three conditions from 1.06×10^6, 1.81×10^6, and 2.81×10^6 (at a maximum freestream speed of about 15 m/s). The latter Reynolds number is near that of a full-scale small helicopter (e.g. Hughes OH-6 Cayuse), and to 1/3rd that of a large helicopter (e.g. Sikorsky S-92). The advance ratio was also varied between 0.2 and 0.4. Once again, phase-averaged 2D PIV measurements were taken in a streamwise-vertical image plane aligned laterally to the center of the fairing, while drag measurements were obtained using a load cell mounted in contact with the rotor hub shaft. The measurements were taken at streamwise locations equal to 2 hub radii downstream and 4 hub radii downstream (near-wake and mid-wake conditions of the previous PSU tests). A sample phase pseudo-spatially resolved panorama of the vertical velocity from PIV measurements taken at the near-wake and far-wake measurement locations behind the PSU 6-inch model is shown in Figure 1.8. Again, the 2/rev and 4/rev fluctuations were observed the PIV harmonics at certain heights in all the hub diameter-based Reynolds number conditions, using the same geometric configuration as Reich et al. (2014, [12]). However, a strong 6/rev fluctuation was not observed in the PIV harmonics at the lowest hub diameter-based Reynolds number, with a strength instead on par with that of other weak harmonics (5/rev, 7/rev, etc.). Similarly, strong 2/rev and 4/rev fluctuations were seen in the drag harmonics of the same configuration at the two higher hub diameter-based Reynolds number conditions

(1.81×10^6 and 2.81×10^6), while the 6/rev drag harmonic was only notable at the highest hub diameter-based Reynolds number (2.81×10^6). This indicates that proper scaling of both drag and wake studies is dependent on Reynolds number. Because the hub is composed of individual bluff body components, the individual component chord-based Reynolds numbers were also reported for the pitch links, the spider links, the scissor links and the blade stubs. This information is summarized for an advance ratio of 0.2 in Table 1.2. These were not varied with respect to each other (i.e. they were the same geometric size in all configurations), so it was unclear whether proper scaling of the hub wake studies should rely on the hub diameter or individual component chords as a basis. Finally, the inclusion of pitch links and a beanie fairing modified the harmonics observed, typically increasing the strength of the 4/rev fluctuation at the expense of the 2/rev fluctuations.

Table 1.2: Reynolds numbers reported for PSU 6-inch model at an advance ratio of 0.2 for hub diameter-based Reynolds number conditions from Reich et al. (2015 [15]).

Reynolds Numbers ($\times 10^5$) of PSU 6-inch Model			
Hub Diameter-based	**26.2**	**18.1**	**10.6**
Component chord-based	↓	↓	↓
Pitch Links	0.64	0.45	0.30
Spider Links	1.8	1.2	0.75
Scissor Links	1.9	1.3	0.8
Blade Stubs	2.6	2.0	1.0

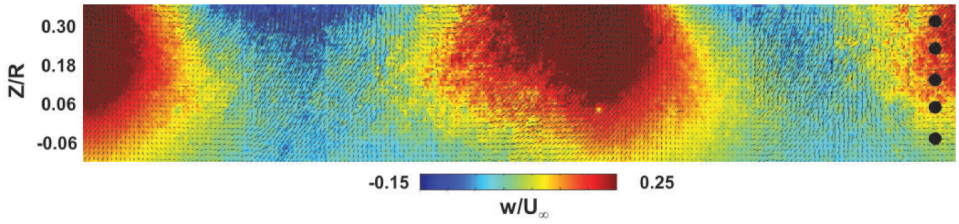

(a) **X = 2R**

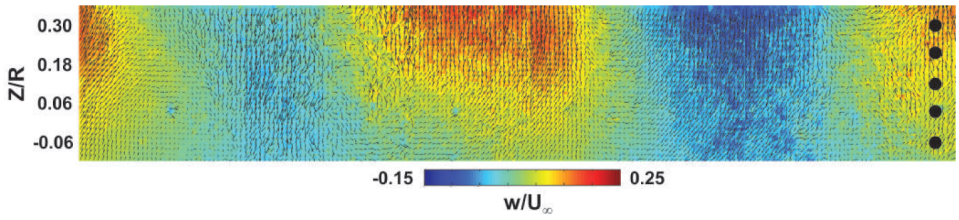

(b) **X = 4R**

Figure 1.8: Near-wake ("$X/R = 2$", top) and far-wake ("$X/R = 7$", bottom) 2D-PIV vertical velocity phase panoramas from the PSU 6-inch tests [15]. Flow is left to right. This figure shows vertical flow structures that have been shed at various hub phases from 0° to 180°, comparable to those seen in Fig. 1.7. Note that Z and w are used to describe the vertical coordinate and vertical velocity, while the current work uses y and v to describe the same. Also note that the vertical distance is scaled to the hub radius, R.

As mentioned previously, the work done at PSU was a direct motivator in the current work, and is used to compare the results of the current work to those of more traditional helicopter wake studies. As stressed by Reich et al. (2016, [9]), the rotor hub is composed of several bluff body shapes. While the hub diameter-

based Reynolds number has traditionally been used to scale the rotor hub, ignoring the local components, it appears that local bluff-body component Reynolds numbers may provide more detailed insight into the rotor hub wake. It is therefore useful to present a brief overview of bluff body aerodynamics.

1.3.2 Bluff Body Overview

Bluff bodies are those shapes for which the component of drag is due to separation of the boundary layer over the body and pressure loss in the wake. This definition is a counterpoint to streamlined bodies, for which the dominant drag component is viscous skin friction. An illustration of the differences in shape and pathlines between bluff and streamlined bodies is shown in Figure 1.9. Two comprehensive reviews of the aerodynamics of a cylinder, the quintessential bluff body, may be found in Roshko (1993, [16]) and Williamson (1997, [17]). Both reviews identify the same diameter-based Reynolds number flow regimes for a cylinder (note: a cylinder's chord is its diameter), though, due to a difference in focus, slightly different names are used for some of the regimes. To illustrate the various flow regimes discussed next, an oft-recreated plot of the cylinder drag coefficient related to the chord-based Reynolds number of the cylinder from Delany & Sorensen (1953, [18]) is included in Figure 1.10, with the flow regimes of interest labeled.

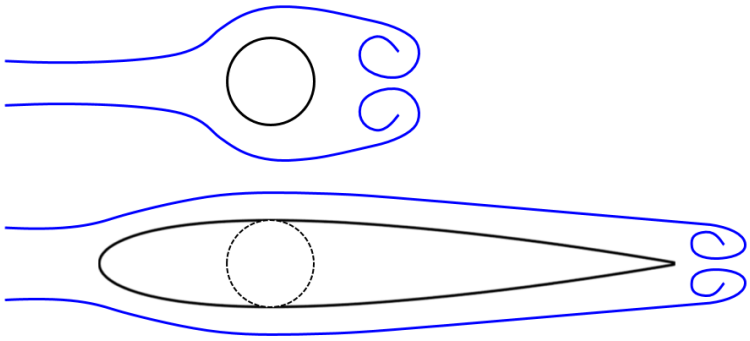

Figure 1.9: A cartoon of the pathlines over a bluff body (top) compared to a streamlined body (bottom) of equal thickness. The wake of a similarly thick bluff body is larger and forms at earlier streamwise locations, thereby causing more pressure drag.

Focusing on the regimes likely to be encountered in rotor hub flow, the first regime of interest is the 'shear layer-transition regime' which lasts from a chord-based Reynolds numbers of 1×10^3 until $\sim 2 \times 10^5$. The shear layer-transition regime is named so because it encompasses the chord-based Reynolds numbers in which the turbulence-transition point moves upstream in the separated shear layer (Roshko, 1993, [16]). In this regime, the wake pattern displays the familiar von Kármán vortex street, illustrated in Figure 1.11. As the chord-based Reynolds number increases, this vortex street becomes less coherent and more three-dimensional. At a chord-based Reynolds number around 2×10^5, the flow enters the 'drag crisis regime,' also called the 'critical regime' and the 'boundary-layer transition regime.' This flow regime acquired the first two names because it is marked by a steep drop in drag. This drop is caused by the formation of a separation-reattachment bubble on one side of the back of the cylinder. Over a comparatively short range of chord-based Reynolds numbers, this bubble grows from the side it started on towards symmetry on both the top and bottom of the cylinder, pushing the boundary layer separation back to about 140° from the upstream stagnation point. Throughout this process,

the boundary layer transitions to turbulence, hence the latter name for the regime. The 'supercritical regime' is marked by the bubble attaining symmetry on the back side of the cylinder, and begins near chord-based Reynolds numbers of 6×10^5. In this region the boundary layer continues to transition towards being fully turbulent, but the separation-reattachment bubble formed at the back of the cylinder remains unchanged; thus the drag coefficient displays a low plateau. At the end of the supercritical regime, with a chord-based Reynolds number of 1×10^6, the boundary layer becomes fully turbulent and separates earlier, thus resulting in the increase of drag. This final regime is called the 'postcritical regime.' Note that all of the benchmark chord-based Reynolds numbers mentioned here are subject to variation due to the surface roughness of the cylinder (Shih et al., 1993, [19]) and the freestream turbulence of the onset flow (Fage & Warsap, 1929, [20]; Nakamura, 1993, [21]), increasing either of which is similar to the effect of increasing the chord-based Reynolds number.

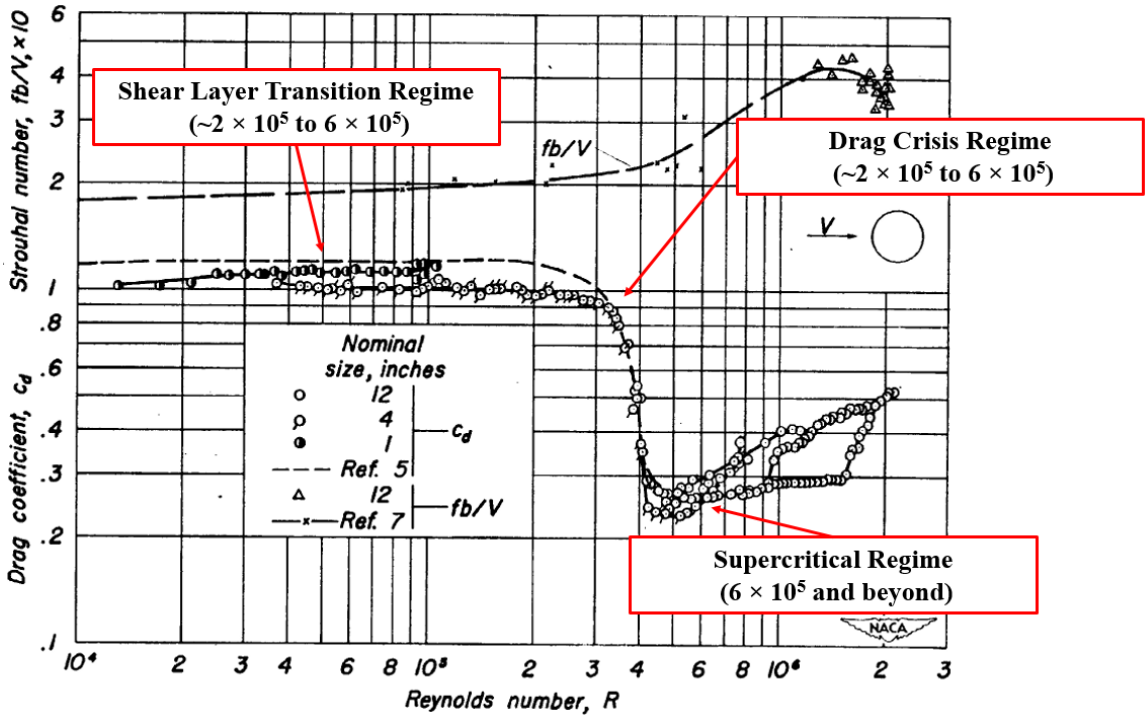

Figure 1.10: Dependency of the drag coefficient of a cylinder on the chord-based Reynolds number, from [18] (modified with labels of flow regimes)

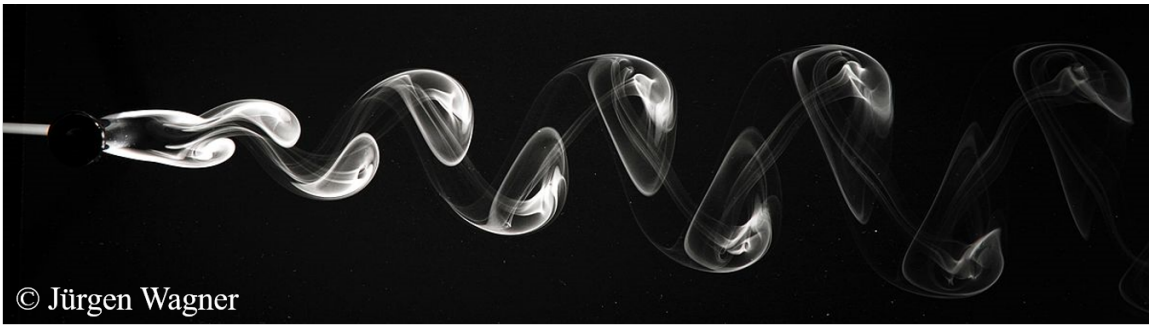

Figure 1.11: Photo of the von Kármán vortex street pattern, typical of the shear layer transition regime of cylinder flow. Photo reproduced under Creative Commons ASA 4.0 license.

Other bluff bodies show similar flow regimes. Besides cylinders, another common bluff body is the 'rectangular cylinder.' This term simply indicates a prism with

rectangular end profiles, and may also be called sharp-edged bluff bodies. Flow regime plots similar to that used for the cylinder earlier are shown for a square cylinder and a 2:1 chord-to-thickness rectangular cylinder in Figure 1.12. The Reynolds number here is still based on the chord of the body. Unlike circular cylinders, however, the range of available data is more limited. Delany & Sorensen (1953, [18]) document the highest chord-based Reynolds number data available for a few simple rectangular cylinder profiles (chord-to-thickness ratios of 1:1, 2:1, 1:2, with three levels of varying corner sharpness). The data reported for all of these profiles may be found in Appendix A. Aside from the importance of drag coefficient in scaling the hub geometry, Strouhal number may also be important, as Reich et al. (2014, [12]) attributed the appearance of the 6/rev fluctuation to Strouhal shedding from a piece with a rectangular profile.

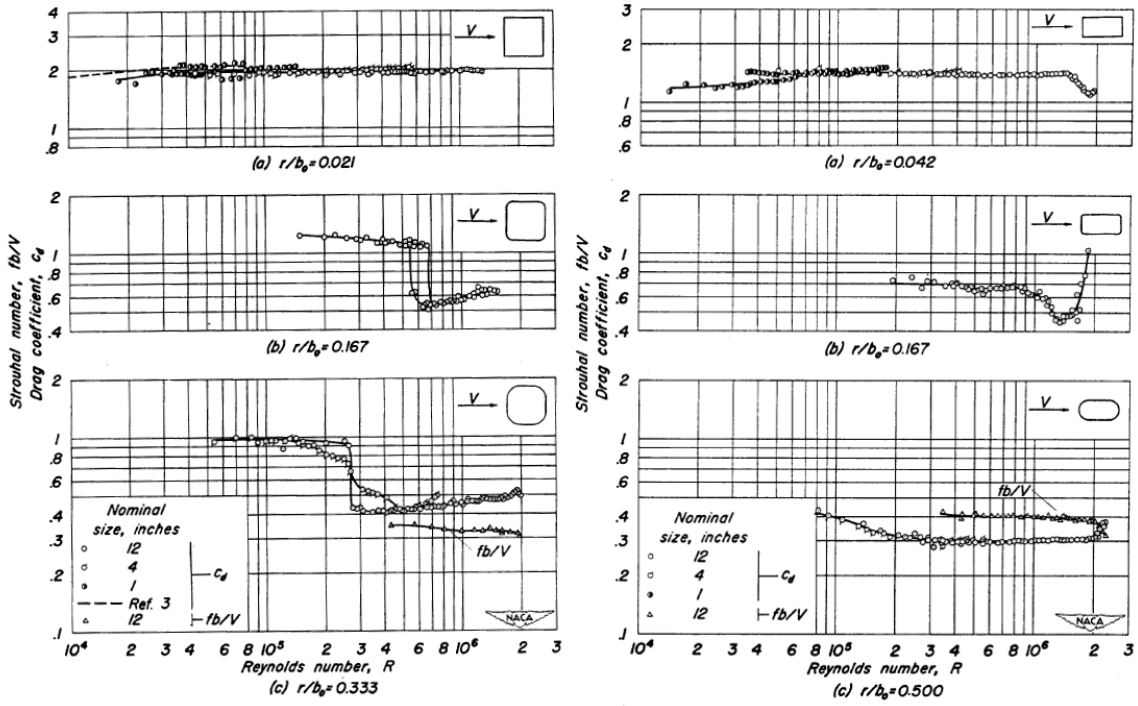

Figure 1.12: Drag coefficients of rectangular cylinders, from Delany & Sorensen [18]

As with the drag coefficients of bluff bodies, the Strouhal number, which was mentioned previously as a nondimensionalization of frequency, has been better stud-

ied for a circular cylinder. For bluff bodies, the Strouhal number is typically based on thickness, and is determined from frequency content of velocity measurements (often using hot-wire or hot-film anemometry) in the bluff body's wake. Delany & Sorensen (1953, [18]) compiled previous results for thickness-based Strouhal number data for cylinders operating in the critical and supercritical regimes, whilst contributing postcritical regime data. Thickness-based Strouhal numbers were roughly 0.2 in the pre-critical Reynolds number ranges ($< 2 \times 10^5$), while the critical Reynolds number marked the start a gradual increase in Strouhal number to 0.4 in the postcritical regime. Roshko (1961, [22]) conducted even higher chord-based Reynolds number experiments on a cylinder with a splitter plate attached downstream of the cylinder. With the splitter plate, the thickness-based Strouhal number was found to be roughly 0.25 in the postcritical chord-based Reynolds number range. Because there was no clear peak in the hot-wire anemometer data used to determine the thickness-based Strouhal number, it was assumed the splitter plate dampened shedding. Therefore, the trend observed by Delany & Sorensen (1953, [18]) of thickness-based Strouhal numbers for circular cylinders switching from roughly 0.2 before the critical thickness-based Reynolds number regime to 0.4 in the post-critical regime is taken to be the better representation of simple cylindrical bluff body thickness-based Strouhal numbers.

As for rectangular bluff bodies, Delany & Sorensen (1953, [18]) report the only data at chord-based Reynolds numbers above 1×10^5. Similar to the regular cylinder, the thickness-based Strouhal numbers for sharp-edged bluff bodies operating in the critical, supercritical and postcritical chord-based Reynolds number flow regimes were observed to rise from around 0.15 to maximum values near 0.4. On the lower end of the chord-based Reynolds number ranges, Okajima (1982, [23]) observed an initial rise thickness-based Strouhal numbers of roughly 0.16 for sharp-edged rectangular profiles with chord-to-thickness ratios of 2:1 and 3:1 at Reynolds numbers above $4 \times$

10^2, which were followed steep drop in thickness-based Strouhal numbers of roughly 0.8 and 0.11, respectively. For the 3:1 aspect ratio profile, the Strouhal number was shown to recover back to 0.16 at a chord-based Reynolds number of about 6×10^3. These trends were replicated in Norberg (1993, [24]), though the 2:1 aspect ratio profile displayed significant scatter based upon the particular model used. This drop in thickness-based Strouhal numbers was attributed to the formation of an unsteady separation-reattachment bubble at the leading edge of the rectangular profile. Schewe (2013, [25]) found the thickness-based Strouhal number of a 5:1 chord-to-thickness aspect ratio body to be comparatively constant (small variations between 0.110 and 0.115) with thickness-based Reynolds numbers of 1.2×10^3 to 6×10^4. Putting together the previous results as a whole, the thickness-based Strouhal numbers of rectangular profiles are between 0.11 and 0.15 (depending on the chord-to-thickness aspect ratio of the profile) for chord-based Reynolds numbers up to the onset of drag crisis, at which point they increase steadily to 0.4 in the supercritical and postcritical regimes, as observed by Delany & Sorensen (1953, [18]).

From the preceding discussion of drag and Strouhal numbers of bluff bodies, it appears that the local rotor hub components may operate in vastly different flow regimes depending on their profile. However, this factor has long been ignored in favor of simply reporting the hub diameter-based Reynolds number, with Reich et al. (2015, [15]) standing as an exception. Thus, the hub diameter-based Reynolds number stands as the only easily accessible basis of comparison of the wake studies. While the hub diameter-based Reynolds number is certainly useful for comparison of rotorcraft size and speed, it does not aid as much in the discussion of frequency content in the wake. Therefore, rotor hub wake studies should, at very least, estimate the component chord-based Reynolds numbers alongside the hub diameter-based Reynolds number for their test models, in order to better discern the appropriate scaling for helicopter rotor flow.

1.4 Objectives

As mentioned previously, the primary objective of the current work was to characterize the long-age wake behind a geometrically simple and generic hub composed of canonical bluff body shapes. Here, canonical refers to the two categories of bluff body profiles discussed in the previous section: circular and rectangular cylinders. Observation of consistent frequency content of previous works will be used as the criterion for evaluation of results. The specific frequency content sought after are the 2-per-hub-revolution and 4-per-hub-revolution frequencies, which are tied to the passage of large scale 2-per-hub (scissor links) and 4-per-hub (blade shanks) geometry. By creating a hub with similar large-scale symmetry to previous hubs (i.e. prominent 2-per-hub and 4-per-hub features), this will serve as a preliminary exploration of the possibility of simplifying the helicopter rotor hub to uncover the underlying physical flow phenomena. With a simple and easily defined hub, future experimental studies may more easily target geometric variations of interest while using a common basis of comparison, and computational studies may devote more resources to accurately modeling the wake of the hub.

To accomplish this objective, a simple hub configuration was designed, and three separate models were generated by varying two geometric parameters (the sharpness of the blade shank geometry's corner and the phase angle of the scissor link geometry). The models were then mounted in the Experimental Flow Physics Laboratory Large Water Tunnel (EFPL-LWT) at Oklahoma State University (OSU), and 2D PIV measurements of the wake were taken seven hub radii downstream. While the component-specific Reynolds numbers are discussed later, the models were tested at an advance ratio of 0.2 with a hub diameter-based Reynolds number of 7.6×10^5, the maximum acheivable in the EFPL-LWT.

CHAPTER 2

EXPERIMENTAL METHODS

2.1 Test Facility

The experiment took place in the Experimental Flow Physics Laboratory (EFPL) Large Water Tunnel (LWT) at Oklahoma State University (OSU), shown in Figure 2.1. The LWT is a recirculating water tunnel, designed primarily for the study of turbulent boundary layers at high Reynolds numbers. The design and characterization of the tunnel is detailed in Daniel et al. (2015, [26]) and Farsiani & Elbing (2016, [27]), respectively. In brief, the test section is 1.1 m long and has a 152 mm $\times$ 152 mm (6 in $\times$ 6 in) square cross-section, with acrylic walls that provide optical access. The tunnel can be pressurized up to a maximum gauge pressure of 276 kPa (40 psi), and it is powered by a 150 hp variable-speed centrifugal pump, which can provide a maximum empty-test section freestream speed of 10.1 m/s. The free-stream turbulence intensity at the inlet is reduced to below 0.3% by a tandem honeycomb and settling chamber section upstream of an 8.5:1 contraction. As shown in Farsiani & Elbing (2016, [27]), the test section inlet velocity profile is uniform, and the boundary layer is approximately 10 mm tall at a flow speed of 10 m/s. To facilitate mounting the model, a small hatch on the top of the tunnel was repurposed. A schematic of the tunnel is shown in Figure 2.2.

Figure 2.1: EFPL Large Water Tunnel at OSU

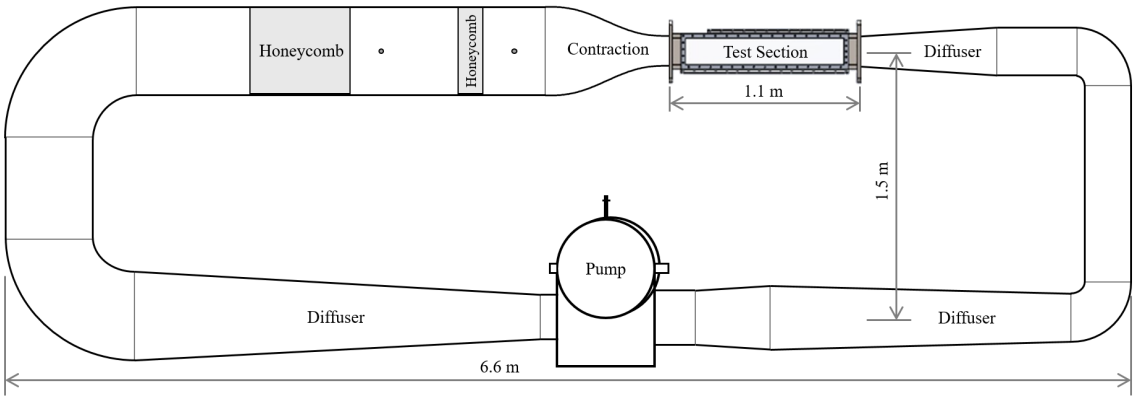

Figure 2.2: Schematic of the LWT

2.2 Experimental Design

The experiment was conducted in two different peices, due to changing hardware availability. In preliminary tests, replication of the trends observed at the Pennsylvania State University Applied Research Laboratory was pursued using time-resolved PIV of the wake behind the hub. In the final tests, a comparison between two model configurations was conducted with phase-averaged PIV. The model geometry was changed very slightly between the two experiments.

2.2.1 Model Design and Scaling

The same reference case used at the Pennsylvania State University (PSU) Applied Research Laboratory (ARL) was used (as discussed previously in Chapter 1 - Section 1.3.1), to determine the target Reynolds number, advance ratio and geometric ratios for the hub. This reference was a large commercial helicopter, estimated to fly at a forward flight speed of 42 m/s with a rotor blade tip-based advance ratio of 0.2. Using the same assumed hub radius of approximately 14% of the rotor blade radius used at PSU, the corresponding rotational frequency of the full-scale hub is approximately 26.5 rad/s (250 rpm). At these conditions, the maximum Mach number on the hub is 0.18 and the hub-diameter-based Reynolds number is 7.3×10^6. A summary of this scaling information is provided in Table 2.1. Note that the maximum Mach number of 0.18 indicates that the flow may be assumed to be incompressible; therefore experimentation may be conducted in a water tunnel. For reference, formal definitions of the hub diameter-based Reynolds number and the rotor blade tip-based advance ratio may be found in Chapter 1 (Section 1.2). While chord-based Reynolds numbers of individual components are important, matching them to previous hubs was not considered here in order to allow flexibility in the design of the model geometry. They are instead reported later.

Table 2.1: Full-scale helicopter scaling parameters

Forward Flight Speed, U_{FS}	42 m/s
Rotor-tip Advance Ratio, μ_R	0.2
Hub Radius-to-Rotor Radius Ratio, d/R	0.14
Hub Frequency, Ω	26.5 rad/s (250 rpm)
Maximum Mach Number, Ma_{FS}	0.18
Hub Diameter-based Reynolds Number, $Re_{d_{FS}}$	7.3×10^6

The test models were designed with two objectives in mind: 1) to simplify the helicopter hub geometry as much as possible whilst keeping hub features thought to be responsible for the 2/rev and 4/rev vortex shedding based on PSU results and 2) to obtain the highest possible hub diameter-based Reynolds number for the model. To do this, the hub model tested at the PSU was used as a starting point, and is shown in Figure 2.3. A list of the major components and their geometric frequency (the number of times they appear on the hub) is given in Table 2.2. Note that this list matches with the previous one given for a typical hub in Chapter 1 (Section 1.2), though the pitch links and beanie fairing were not present. As previously mentioned, the scissor links are thought to be responsible for the 2/rev signal in the wake, as they are the components that appear only twice on the hub; similarly, the blade shanks are likely to be the strongest contributor to the 4/rev signal because they comprise the largest geometry that occurs four times on the hub. Therefore, to simplify the model, all other components (both spider links and the swashplate) were disregarded, as they would more likely only strengthen the signal corresponding to their respective geometric frequencies (Reich et al., 2015, [15]). The last major geometric change to the hub was the removal of vertical deflection of the scissor link arms, parallel with the shank arms. This decision was made because it would increase fabrication difficulty and increase stress concentrations, necessitating a stronger material. With only the

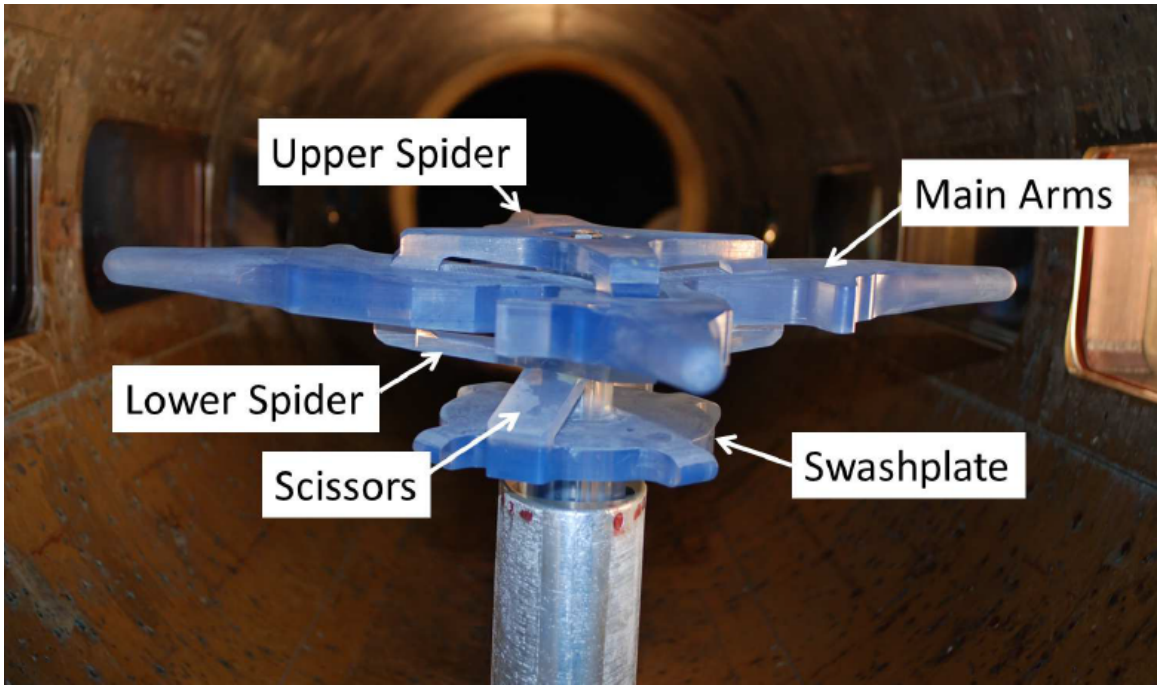

Figure 2.3: Model rotor hub used at PSU [14]

blade shanks, the rotor mast and the scissors left to consider, the constraints imposed by the tunnel were taken into consideration.

To avoid shank tip-to-test section wall interference, a maximum hub diameter was selected to be 76 mm (3 in), half that of the test section width. The PSU model was used to determine geometric ratios of the thickness of the shank arms and the scissor arms, the diameter of the scissor arms and the vertical gap between the scissors and

Table 2.2: Major geometric components of PSU model

Model Component	**Geometric Frequency (#/hub)**
Rotor Blade Shank Arm ("Main Arm")	4
Upper Spider Link Arm	4
Lower Spider Link Arm	4
Scissor Link Arm	2
Swashplate	1

the shank arms, all scaled with the hub diameter. Thus, the hub diameter was used to set many of the dimensions of the rest of hub model. A canonical study (Delany & Sorensen, 1953, [18]) was consulted to set the shank arm profile; of the many profiles available, a rectangular profile with a chord-to-thickness aspect ratio of 2:1 (twice as long as it is tall) was selected. To minimize torque on the model, a profile with a rounded corner (corner radius-to-thickness ratio of 0.167) was initially selected for preliminary experiments, but changes in model material and fabrication necessitated a final profile with a sharp corner for the final tests. The initial and final blade shank profiles, with their respective Reynolds number dependency, are illustrated in Figure 2.4. A fuller set of canonical data is found in Appendix A. The scissor profile was first chosen to be the same as the shank profile. However, during prototyping, the chord was doubled due to fracturing in the prototype model. This resulted in a rectangular profile with a chord-to-thickness ratio of 4:1. For the preliminary tests, the models were rapid-prototyped with an SLA 3D printer (Formlabs 1+). In the initial experiments, though, the shank arms of the prototype suffered fatigue failure and broke. The models were therefore re-fabricated for the final tests from aluminum (Al-6061) as two pieces: a top piece that formed the four shanks (larger arms), and a bottom piece that formed the mast and scissors. These two pieces were then press-fit and welded together for each model configuration. The final model design is shown in 2.5, with a breakdown of the various components, while a side-by-side comparison of the prototype and final models of one configuration may be found in Figure 2.6, and a side-by-side comparison of the two final model configurations may be found in Figure 2.7.

The final hub design had a diameter-based Reynolds number of 7.6×10^5, for a freestream test section speed of 10 m/s with a nominal viscosity of 1×10^{-6} m^2/s. This Reynolds number is basically 1/10th that of a large full-scale helicopter. A rotor-tip advance ratio of 0.2 was used along with the assumption that the hub model radius

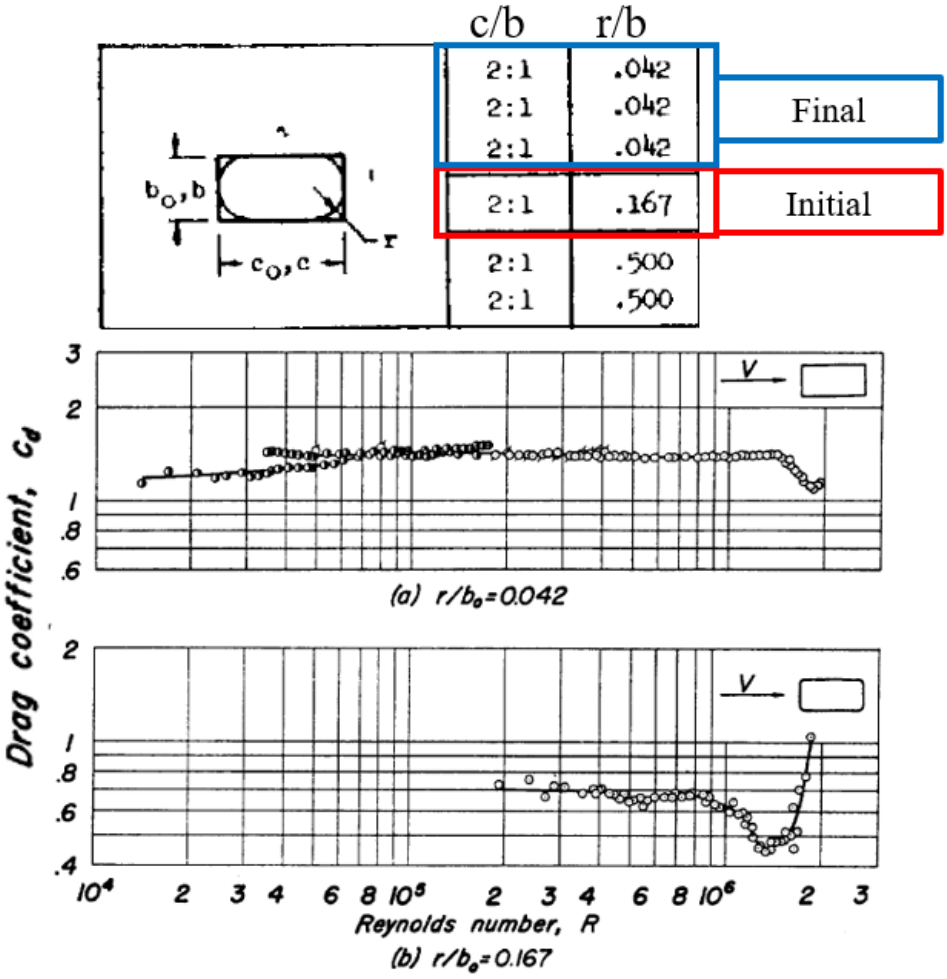

Figure 2.4: Profiles considered for the shank arms [18]. Highlighted in red is the preliminary test profile, while the final test profile is highlighted in blue.

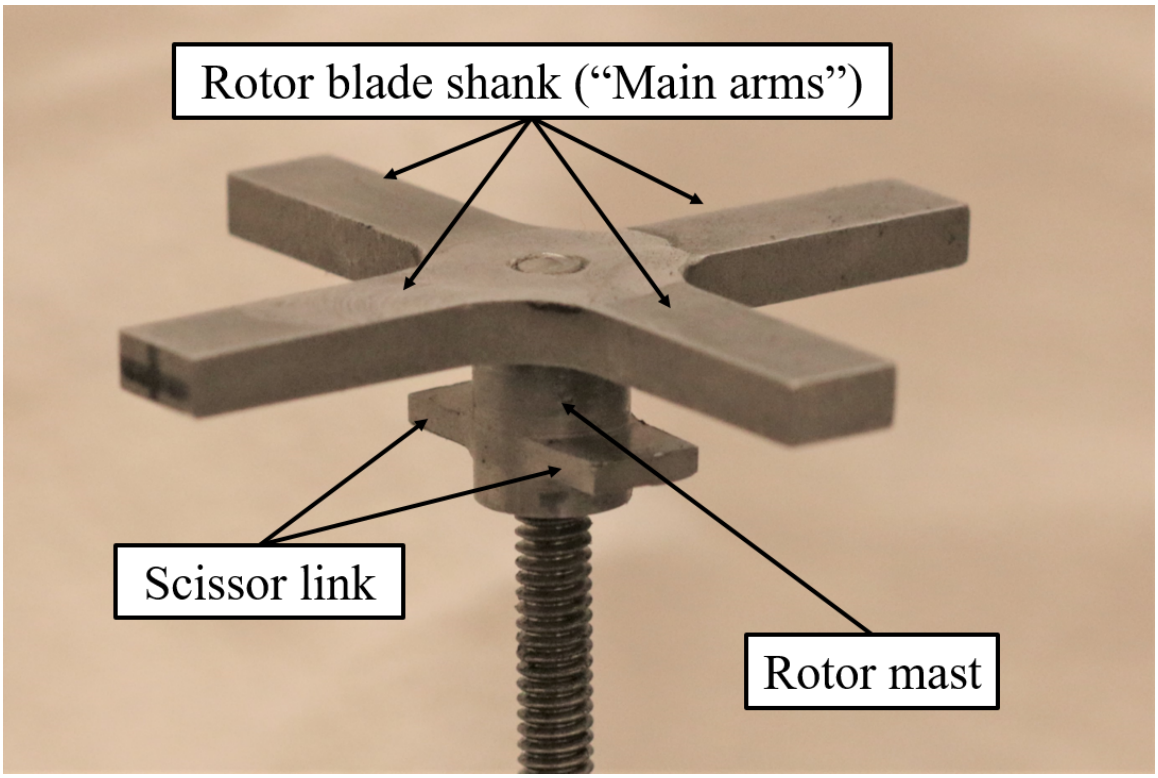

Figure 2.5: One configuration of the final model design

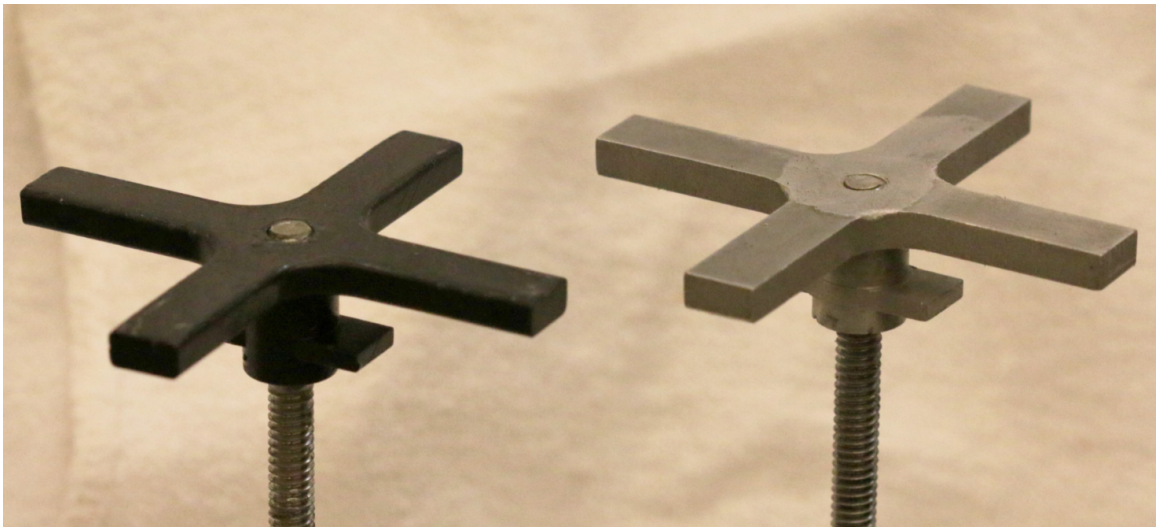

Figure 2.6: An untested model from preliminary tests (left) and a model from the final test (right). The scissor links are in-phase for both of these models.

Figure 2.7: Final test model configurations: out-of-phase scissor links (left) and in-phase scissor links (right).

would be 14% of the rotor blade radius to calculate the necessary hub frequency. However, it is important to note that the model did not actually incorporate rotor blades, so this rotor blade radius was imaginary, and used only to back-solve the for the necessary hub frequency. To keep a rotor blade tip-based advance ratio of 0.2, the hub was rotated at a nominal speed of ∼190 rad/s (1800 rpm, 30 Hz). For the final geometry of the hub, Figure 2.8 should be consulted. Mechanical drawings of all the hubs tested in the current work are found in Appendix B. Additionally, a summary of this scaling information is found in Table 2.4 at the end of this chapter, next to the that of the full-scale hub. Also included at the end of the chapter in Table 2.5 are the component chord-based Reynolds numbers, thickness-based Strouhal numbers and the expected frequency contribution to the wake based on the Strouhal numbers. Note: the thickness-based Strouhal numbers are estimated from literature discussed previously in Chapter 1 (Section 1.3.2). Of all of the components, the only one with a Strouhal frequency harmonic close to those of interest to this study is the rotor mast (with a 5/rev Strouhal frequency). However, it is operating at a chord-based Reynolds number of 1.3 × 105, which is in late shear-transition regime of a cylinder

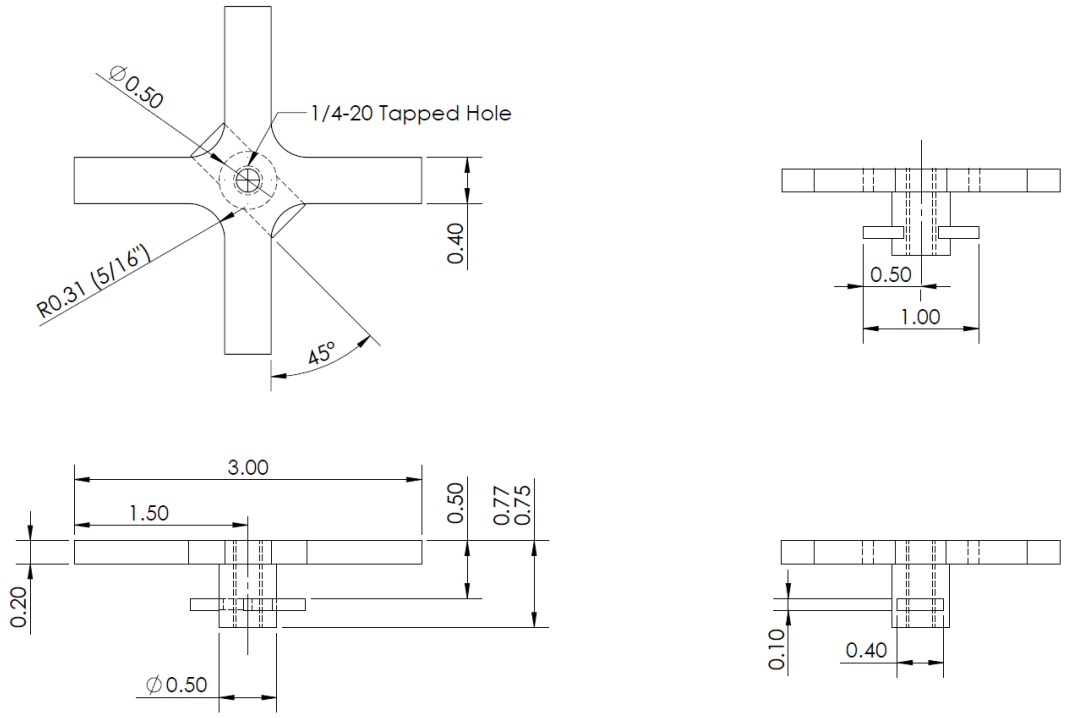

Figure 2.8: Mechanical drawing of one configuration of the final design

and near to the canonical onset of the drag crisis at a chord-based Reynolds number of 2×10^5. With the added effect of interference from the other components, the rotor mast may have entered a critical regime, and therefore its Strouhal number may be anywhere between 0.2 and 0.4, with resulting frequencies of 5/rev through 10/rev. Note that if the Strouhal number of the rotor mast is increased slightly to between 0.21 and 0.24, the rotor mast will produce a 6/rev shedding harmonic. Also, because the mast is operating near the drag crisis regime, it is reasonable to expect the rotor mast's wake to be three dimensional; 5/rev or higher frequency content is a potential in the wake.

A fairing was attached to the hub model assembly to reduce drag and turbulent wake noise from the rotor mast. The fairing was 3D-printed and was comprised of two parts: a vertical mast fairing and a bottom wall fairing. For the preliminary tests, this fairing mimicked that of the PSU tests, while the airfoil profile was lengthened

in the final tests. In both tests, the vertical mast fairing was a rectangular planform wing section with that protruded from the tunnel wall into the free-stream; for the initial tests, this airfoil used for the was a NACA 0025 airfoil as with the PSU fairing. Concerns over the higher level of noise behind the fairing led to speculation that separation was occuring, so the airfoil was changed to a NACA 0015 for the final tests. Note, however, that no separation was actually observed during testing, as no measurement or flow visualization was attempted at the rotor hub location. The tip of the fairing was left flat, parallel with streamwise flow as in the PSU tests, to minimize the impact of the fairing's interference on hub flow. Because the fairing was to be attached to the inside of the tunnel with machine screws, the bottom tunnel wall fairing was necessary to avoid boundary layer modification and separation caused by exposed screw heads. This bottom fairing was composed of a 1.5:1 elliptical leading edge followed by a flat section for the screws to be attached through and a linearly decreasing trailing edge with a height-length ratio of 13 (height-length ratios of 10 or above are recommended to prevent separation on blister-type fairings [28]). A CAD illustration of the fairing is provided in Figure 2.9.

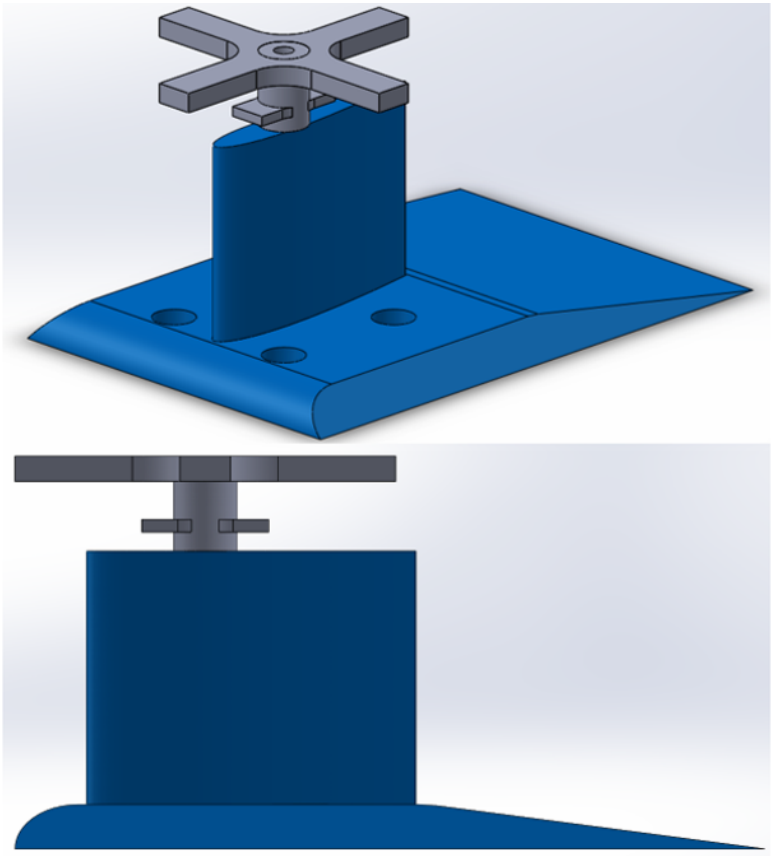

Figure 2.9: CAD model of the fairing

2.2.2 Mechanical Design

As mentioned previously, a small hatch at the top of the test section was repurposed to affix the model and motor to the tunnel. The mounting hatch, made from aluminum (Al-6061) and anodized, was designed to fit flush with the test section walls and had a large clearance hole to allow a rod to pass through the test section wall. This hole was intended to be large enough to allow for testing different angles of attack for the hub. In addition, the mounting hatch had a set of four 1/4"-20 threaded holes on the inside and outside plate surfaces to allow additional attachments (e.g. sealing gaskets, fairings, etc.). Sealing this hatch was problematic and is discussed subsequently. A series of blind holes along the rim of the hatch were intended for

attaching the hatch to the test section; however, fabrication error resulted in through-holes instead, necessitating further sealing. In order to attach the hubs to the motor (Cobalt 40S, Astro), a threaded hole was drilled through the center of each model. The models were then fixed to threaded drive rods using threadlocker (Blue 242, Loctite). During testing, the drive rod was screwed into an adapter to attach it to the motor, which was rigidly suspended over the test section using a support structure bolted to the mounting hatch and test section. Every component of the mechanical design was ultimate fixed to the test section using the mounting hatch, so that the predominant modes of vibrational oscillation would be at the tunnel motor's frequency. However, no vibrational frequency analysis or experimentation was conducted for the mechanical setup. An illustration and picture of the mounting structure is provided in Figure 2.10.

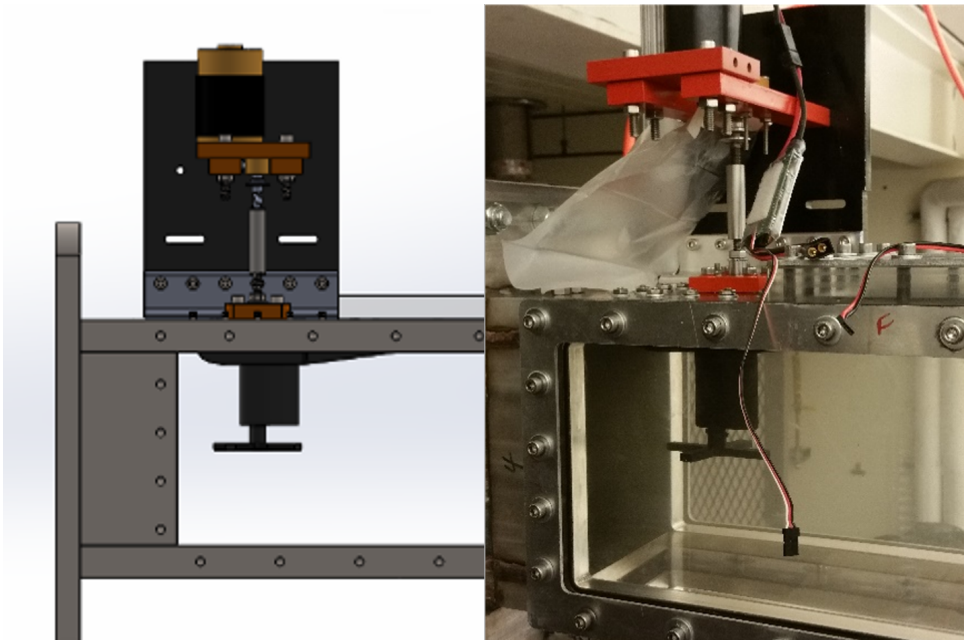

Figure 2.10: CAD of the mechanical mounting structure (left) and a photo of prototype hub mounted in the tunnel (right)

Sealing the tunnel proved to be difficult. Many iterations were attempted, the

final design is shown in Figure 2.11. All of the major components are labeled, and the seals are highlighted with green fill, while the rotary shaft to which the model was fixed has an orange highlighted border. To begin with, the mounting hatch mentioned previously (colored black in the figure) was fixed to the test section (marked in light blue/gray). The test section has its own seal, so the hatch needed only to be fixed to the tunnel to seal the potential outlet between it and the test section. Next, a gasket plate was attached to the top of the mounting hatch. This gasket hatch had a Buna-N rubber O-ring sealing the potential flow outlet between it and the top of the mounting hatch, as well as a groove to which a rotary shaft seal was press-fit. The rotary shaft seal was composed of a stainless steel outer backing for support, and a clipper-type seal on the inside. This clipper seal had a U-shaped profile, and a spring was wrapped around the inside sealing lip. Because the rotary shaft was too small in diameter to be sealed by the shaft seal, a sealing adapter was fabricated with the necessary outer diameter matched to the inner diameter of the shaft seal. This sealing adapter had a threaded center hole, allowing it to be screwed on to the rotary shaft. Finally, to seal the potential flow outlets of the threaded rotary shaft, a thread-sealing washer was added to each side of the sealing adapter and clamped down using hex nuts screwed onto the shaft. Overall, this sealing set up was successful. However, it was very prone to fatigue failure and installation damage; after a single model was tested, the shaft seal typically had to be removed and a new one installed as the rubber lip was worn away and damaged by the rotation of the sealing adapter in spite of the addition of lubricating oil (SAW 80W-90). Additionally, if the shaft seal was not evenly press-fit into the gasket plate, the stainless steel backing of the plate tended to bend, destroying the parts ability to properly seal. While utilized for the current work, a better method of sealing the tunnel should be developed.

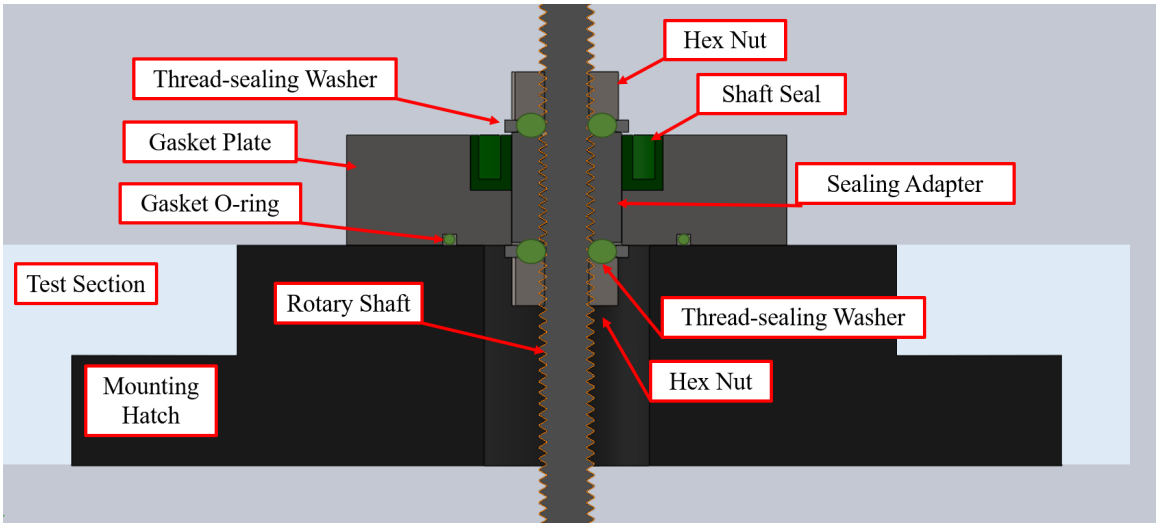

Figure 2.11: CAD of the setup used to seal the tunnel. Sealing material is highlighted in green, and the rotary shaft to which the hub was fixed has an orange highlighted border.

2.3 Instrumentation

In the preliminary tests of the experiment, time-resolved velocity data were acquired seven hub diameters downstream of the hub with two-dimensional particle image velocimetry (PIV). This distance was twice as far as what previous wake studies have examined, but can still provide information about the long-term development of the wake. However, it is more difficult to compare to previous results. The measurements were acquired at 1 kHz with a high-speed camera (Phantom M110) with a resolution of 1280 px $\times$ 800 px, using a commercial PIV image acquisition and processing package (Davis 8, LaVision). To calibrate the images, a three-dimensional calibration target was used (Type 058-5, LaVision). A 60mm diameter, f/2.8D lens (AF Micro-NIKKOR, Nikon) was fixed to the camera, and the final field of view was roughly 110 mm $\times$ 80 mm. The image plane was aligned parallel to the flow, centered behind the fairing, and illuminated using a laser sheet produced by a high-speed Nd:YLF laser (DM30-527, Photonics). The beam was directed to a 45° mirror, focused and spread

into a sheet using a cylinder lens. A diagram of the optics path is shown in Figure 2.12. Glass spheres with an average diameter of 18 microns (im30K, 3M) were used for flow seeding. The high-speed camera, which was controlled by the PIV image acquisition program, stores each image in its own RAM during recording before saving them to a hard drive. Limitation in the on-board memory of the camera limited each recording to a length of 350 sequential, single-frame images. A total of 9 useful recordings were taken. A 10th recording was also taken, but the hub failure mentioned previously was observed in it, thereby discounting it. The raw data sets were processed using the same commercial PIV package using a standard multi-pass cross-correlation method, with decreasing interrogation window size of 50% overlap from 512 px × 512 px to 16 px × 16 px. The final vector spacing was about 0.8 vectors/mm in both x and y dimensions. In the preliminary tests, an additional high-speed camera of the same model was mounted upstream to record footage of the hub. No PIV processing was done on these images, though; it was used simply to monitor the phase and status of the hub.

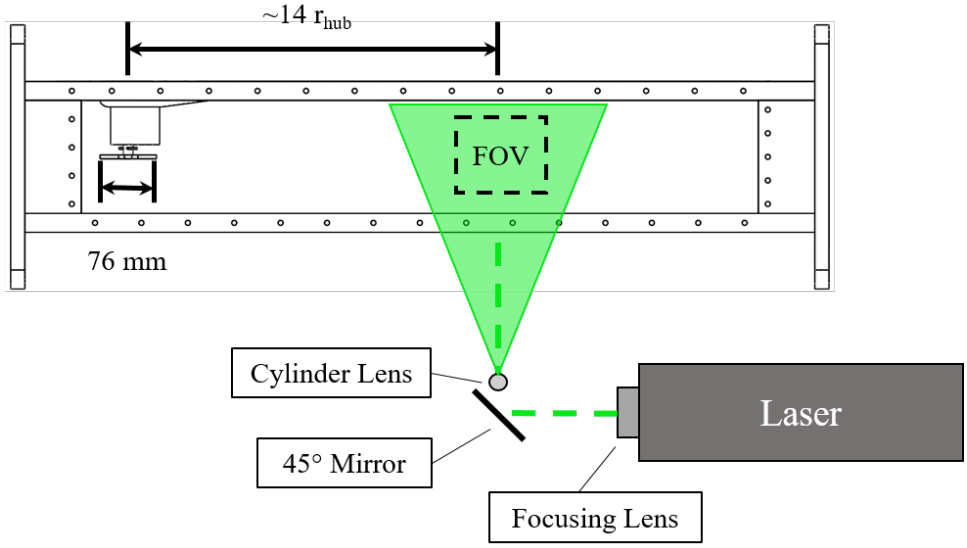

Figure 2.12: Diagram of the optics path for the laser sheet used for PIV. For the preliminary, time-resolved tests, the FOV was 110 mm × 80 mm.

In the final tests, phase-averaged velocity data were acquired seven hub radii downstream of the hub using two-dimensional particle image velocimetry (PIV). The image plane was aligned parallel to the flow, centered behind the fairing, and illuminated with a 532-nm wavelength laser sheet, produced from a beam of a pulsed Nd-YAG laser (Gemini 200, New Wave Research). Each pulsed beam of the laser was focused using a focusing lens mounted at the exit to the laser, directed into a 45° mirror and spread into a sheet using a cylinder lens. A diagram of the optics path is shown in Figure 2.13. The water tunnel was flooded with glass bubbles with an average diameter of 18 microns (im30K, 3M) to be used as tracer particles. A high-resolution (2560 pixels $\times$ 2160 pixels) sCMOS camera (Imager sCMOS, LaVision) was used to image the laser plane, and was mounted normal to the tunnel on a platform, itself rigidly mounted to the water tunnel. A 60 mm diameter, f/2.8D lens (AF Micro-NIKKOR, Nikon) was attached to the camera to yield a final field-of-view of 120 mm by 100 mm. The camera was spatially calibrated using a 58 mm $\times$ 58 mm stereo calibration plate (Type 058-5, LaVision) with circles of 1.2 mm spaced 5 $\pm$ 0.02 mm apart. The timing for both the camera and the laser were controlled using a commercial PIV acquisition and processing package (DaVis 8, LaVision) and a custom-built Hall effect sensor (described subsequently) to synchronize recording with the phase of the hub. For each phase tested, 100 image pairs were collected and velocity vector fields were computed using a multi-pass cross-correlation method, which were then averaged to produce a phase average. The final interrogation window was 32 $\times$ 32 pixels with a 50% overlap. The final vector spacing was about 0.8 vectors/mm in both x- or y-dimensions.

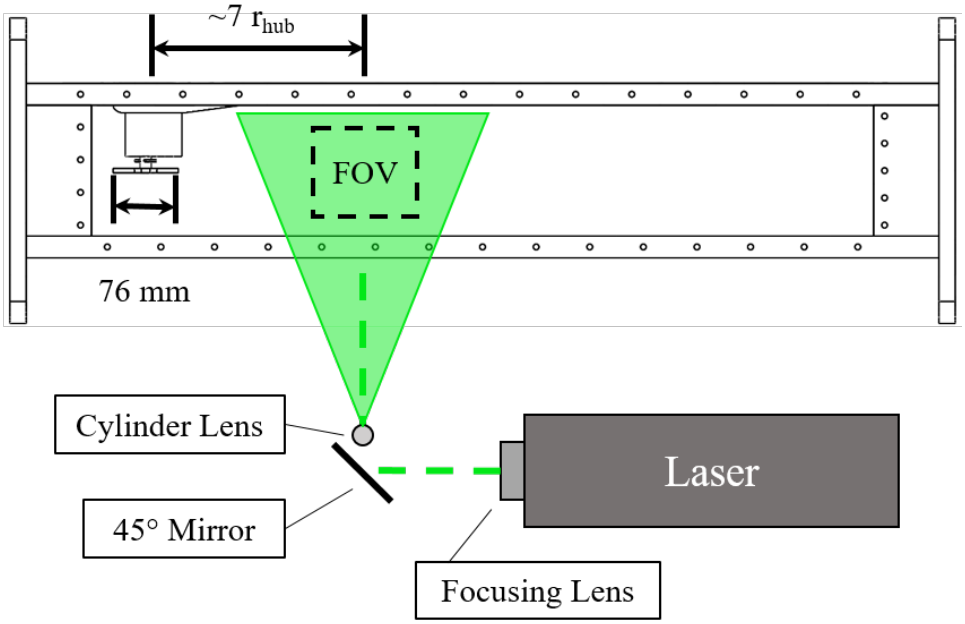

Figure 2.13: Diagram of the optics path for the laser sheet used for PIV. For the final, phase-averaged tests, the FOV was 120 mm × 100 mm, though only a 60 mm × 100 mm box in the center was processed.

In order to monitor the status of the flow in the tunnel, static pressure, temperature and pump motor frequency were recorded using a data acquisition card (USB-6218 BNC, National Instruments) with a commercial data acquisition program (LabView 15.0.1, National Instruments). Note that this was not the same acquisition system used for PIV measurements; the two systems were independent of each other. The static pressure of the tunnel was recorded using a pressure transducer (PX2300-50DI, Omega) mounted upstream of the contraction inlet, and aligned vertically the centerline of the test section. Using a step-up resistor to convert the 4-20 mA output of the pressure transducer to a more useful recording voltage, and the signal was recorded with the data acquisition system. The static pressure of the test section is determined from the measured pressure upstream by use of a Bernoulli-type equation, subtracting the difference in dynamic pressures from the measured pressure. As a side

note, the tunnel pressure was also observed using a traditional pressure gauge. The temperature of the water in the tunnel was measured between the two sections of honeycomb using a T-type thermocouple (TC-T-1/4NPT-U-72, Omega) that extended roughly 6 mm into the flow to avoid boundary-layer temperature effects. Because the thermocouple was inserted into the flow between the two honeycomb sections, the effect of the protrusion of the thermocouple was minimal. The tunnel's pump motor frequency was manually set on a variable-frequency-drive (EQ7-4150C, Teco), which had a digital display. The variable-frequency-drive also had an analog output that was used by the data acquisition system to record the pump frequency.

For the phase-averaged tests, a device was required to synchronize the PIV recording to the phase of the hub. This was accomplished using a custom instrument created from a programmable microcontroller (Uno R3, Elegoo) and an off-the-shelf Hall effect switch (A3144, Allegro Microsystems). The Hall effect switch is a sensor that switches between a high voltage wihin a weak magnetic field to a low voltage within a magnetic field past a certain threshold. A magnet was mounted above the sealing adapter on the hub models' rotary shafts. By placing the Hall effect switch within an appropriate distance of this magnet, the switch would activate once per hub revolution, thereby allowing a measurement of the revolutional frequency fo the hub. The microcontroller was used to supply voltage and monitor the output of the Hall effect switch, and to output two signals. The first signal was a digital output to the data acquisition system, allowing the frequency of the hub to be recorded. Using a phase lag calculated using the desired phase increment in measurements (nominally 15°) as shown in Equation 2.1; the second output was given this phase lag with respect to input from the Hall-effect sensor and connected as a trigger to the PIV acquisition system. With the magnet stationary, the phase lag could be incremented to set any desired phase angle of the hub. The Hall effect sensor/switch is shown in Figure 2.14.

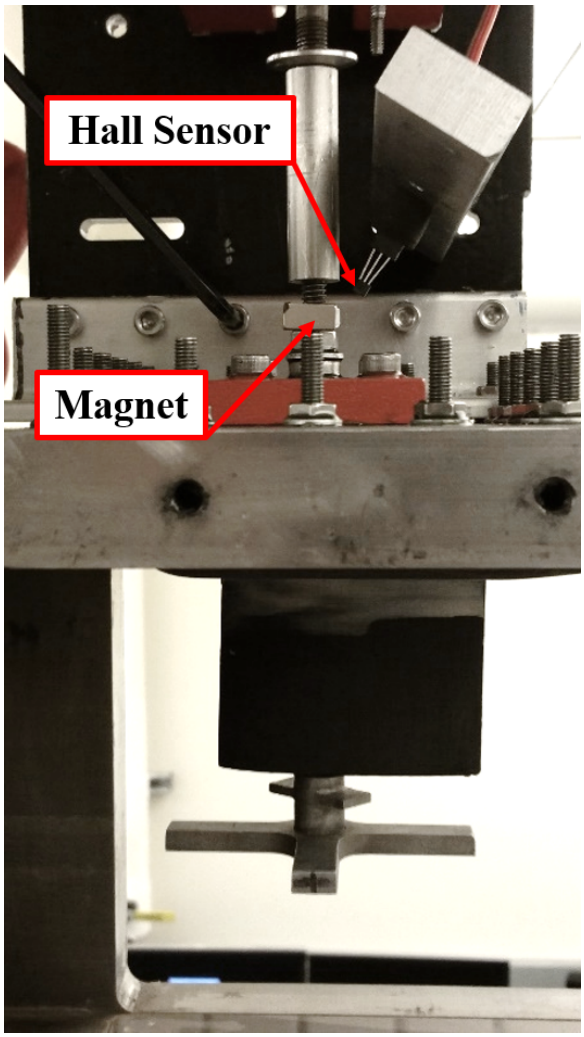

Figure 2.14: Picture of the Hall sensor mounted in the tunnel.

$$dt = \frac{n}{f_{hub}} \frac{\psi}{360^\circ} \tag{2.1}$$

2.4 Test Conditions

To reiterate, experimentation was conducted in two phases. The model examined in each test had a slightly different geometric variation. In the preliminary tests, only one model configuration was tested, while in the final tests, two model configurations were examined. The variations between the configurations can be broken into two

categories: rotor shank profile and scissor link phase. As mentioned in in this chapter, the model used in preliminary testing had rounded corners, while both models used in the final, phase-averaged tests had sharp ones. The difference between the model configurations in the final phase-averaged tests was the phase offset between the scissor links and the rotor shanks. A summary of the geometric configurations that were tested between both preliminary and final tests are listed in Table 2.3.

Model	# of Rotor Shanks	Corner Profile	# of Scissor Links	Scissor Phase
Preliminary	4	Rounded	2	45°
Final: Out-of-phase	4	Sharp	2	45°
Final: In-phase	4	Sharp	2	0°

Table 2.3: Geometric configurations of each model tested.

The locations of the preliminary and final tests are shown in Figure 2.15. The maximum freestream speed of the tunnel, 10 m/s, was used for all tests, and the advance ratio was set to 0.2. In the initial tests, the tunnel was only pressurized to 20 psi to avoid leaking. However, cavitation was observed on the advancing blade shank of the model, so the tunnel static pressure was increased to 40 psi, maximum allowable in the tunnel for the final tests, in which no cavitation was observed. The test conditions and scaling parameters for the hub are summarized in Table 2.4. It was noted earlier that the component chord-based Reynolds numbers should be reported for future rotor hub wake studies. Therefore, the span-averaged chord-based Reynolds numbers for each of components for the current model are shown in Table 2.5. Also shown are the approximate Strouhal numbers for each component, estimated from the trends mentioned previously in Chapter 1 (Section 1.3.2).

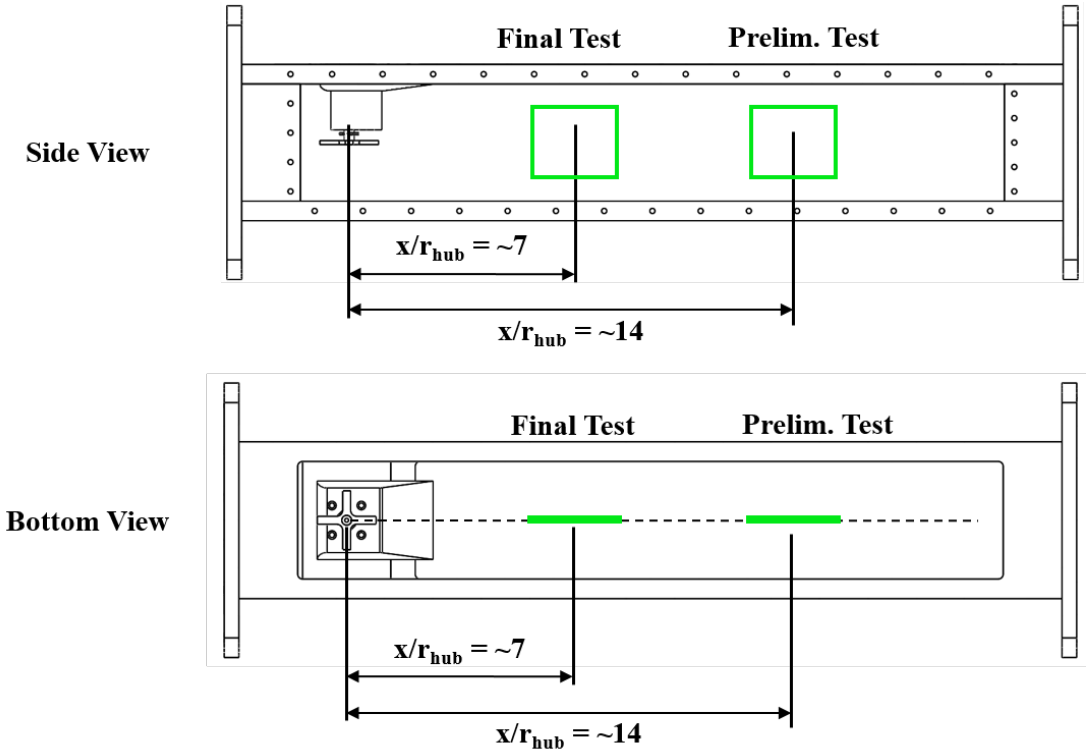

Figure 2.15: Locations of the PIV planes for both experiments.

Parameter	Full-Scale	Prelim. Test	Final Tests
Freestream speed, U	42 m/s	10 m/s	10 m/s
Rotor blade radius, R	~9 m	*~0.3 m* [1]	*~0.3 m* [1]
Hub-to-rotor ratio, r/R	0.14	0.14	0.14
Hub radius, r	~1.25 m	~0.038 m (1.5 in)	~0.038 m (1.5 in)
Advance ratio, μR	0.2	0.2	0.2
Hub rotational rate, Ω	26.5 rad/s	~188 rad/s	~188 rad/s
Hub diameter Reynolds Number, Rehub	7.3×10^6	7.6×10^5	7.6×10^5
Tunnel static pressure	n/a	20 psi	40 psi

Table 2.4: Test conditions and scaling parameters, as well as full-scale parameters.

Component	Reynolds Number ($\times 10^5$)	Strouhal Numbers
Hub Diameter-based	7.6	n/a
Blade Shanks (advancing)	1.6	~0.4
Blade Shanks (retreating)	0.4	~0.15
Scissor Links (advancing)	1.2	~0.4
Scissor Links (retreating)	0.8	~0.13
Rotor Mast	1.3	0.2

Table 2.5: Chord-based Reynolds numbers ($\times$ 10^5) of each component the models tested

Finally, the coordinate system used in the current work is shown in Figure 2.16. The x-axis is defined as the streamwise direction, while the y-axis is defined as the vertical direction. The origin is centered along the axis of rotation of the hub, with the zero-elevation height at the center height of the rotor blade shanks, coincident with the middle height of the test section. This coordinate system varies slightly from those of previous works, where Z was used to denote vertical direction.

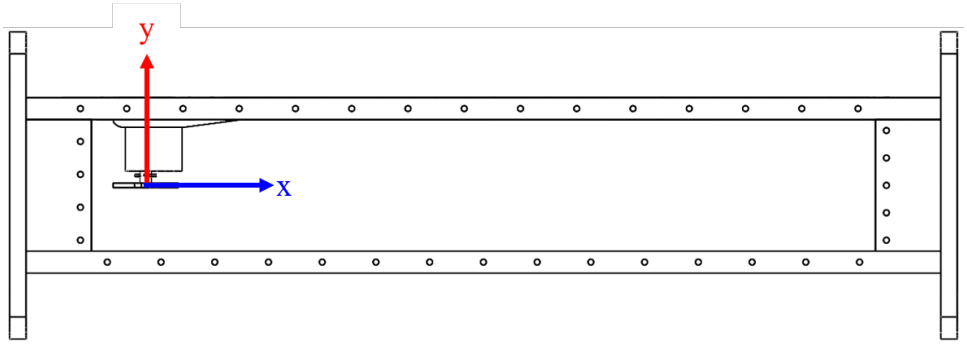

Figure 2.16: Coordinate system used in the current work.

CHAPTER 3

RESULTS

3.1 Preliminary Test (Time-Resolved PIV) Results

3.1.1 Flow Field & Spectral Analysis

A representative contour plot of the time-resolved wake is shown in Figure 3.1. Because the vectors are not shown, the spatial resolution of the field used to make this contour was 0.8 vectors/mm. From the velocity magnitude shown, coherent turbulent structures appear to be present in the very-far wake. To detemine the frequency content of the wake, a frequency spectral analysis was performed on a group of time traces of the wake.

For the series of vector fields, a grid of vertical locations at one streamwise location was examined. The y-locations on this grid were space 5 mm apart and ranged from the freestream to behind the fairing. The grid of points is shown in Figure 3.2. At each of the grid points, an FFT of the velocity magnitude time trace was taken. Frequency spectra from four sample locations are shown in Figures 3.3 through 3.6. The sample locations are spaced through the range of data regimes, the first being located in the freestream (y = -20 mm) to the last, located behind the hub fairing (y = +30 mm). Remember: the hub was mounted upside down in the tunnel, so more positive y-coordinates indicate locations behind the hub and fairing, closer to the test section wall. The full collection of frequency spectra is included in Appendix B. As another reminder of terminology, rotor shank, rotor arm, main arm and blade shank are all interchangable terms.

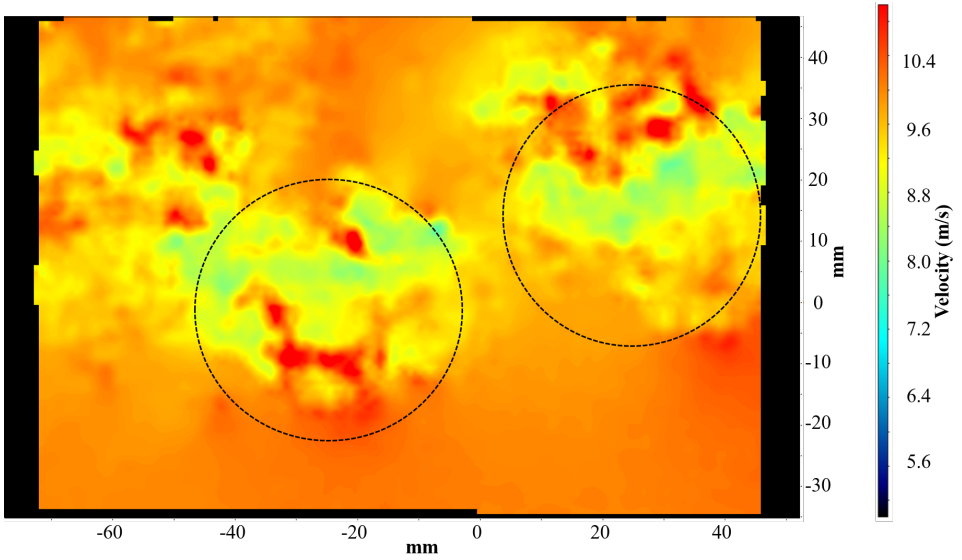

Figure 3.1: Example vector field contour map of the wake 14 hub radii downstream of the hub. Flowfield is a time-averaged snapshot, flow is left to right, and magnitude of velocity is shown. The dotted circles and arrows indicate coherent structures.

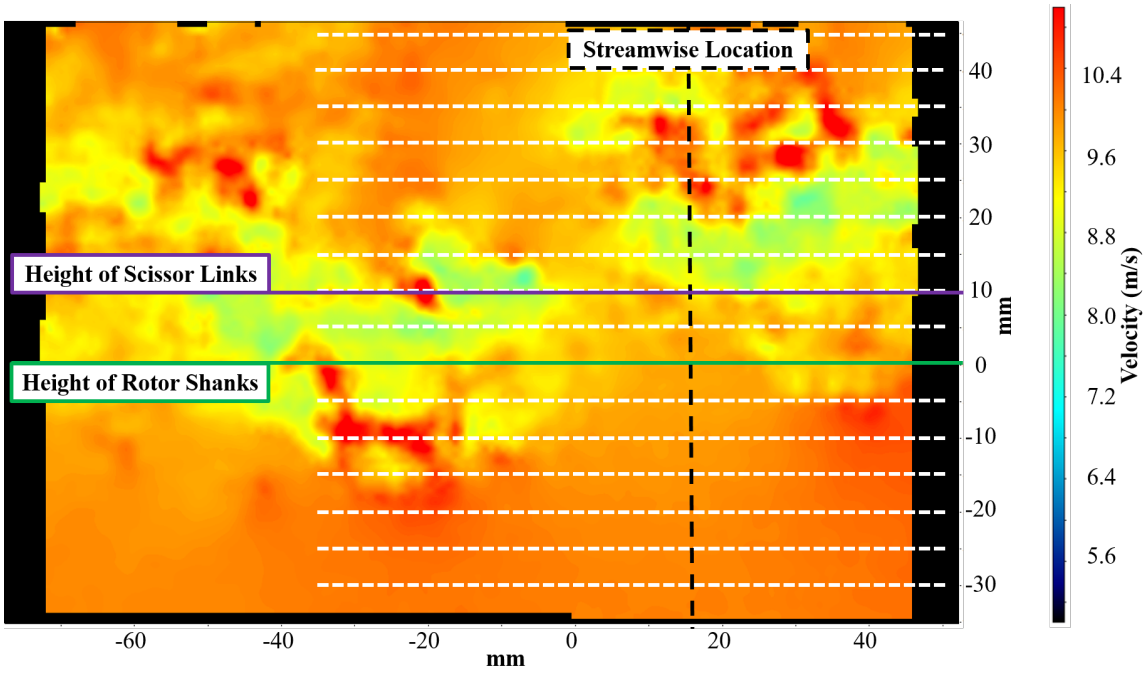

Figure 3.2: Grid of FFT locations, overlaid on contour field from Figure 3.1

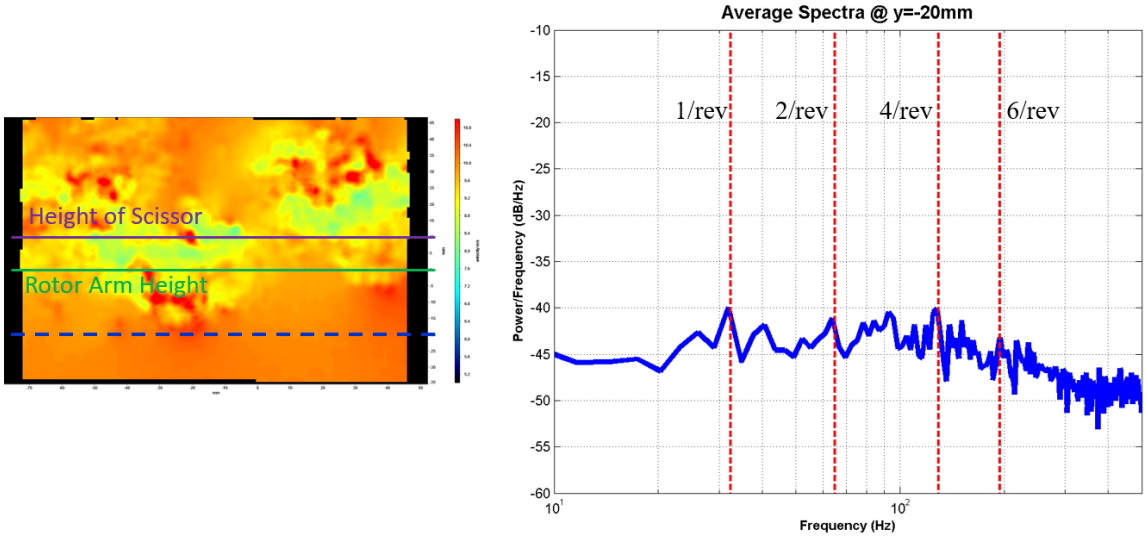

Figure 3.3: FFT at y = -20 mm (Freestream)

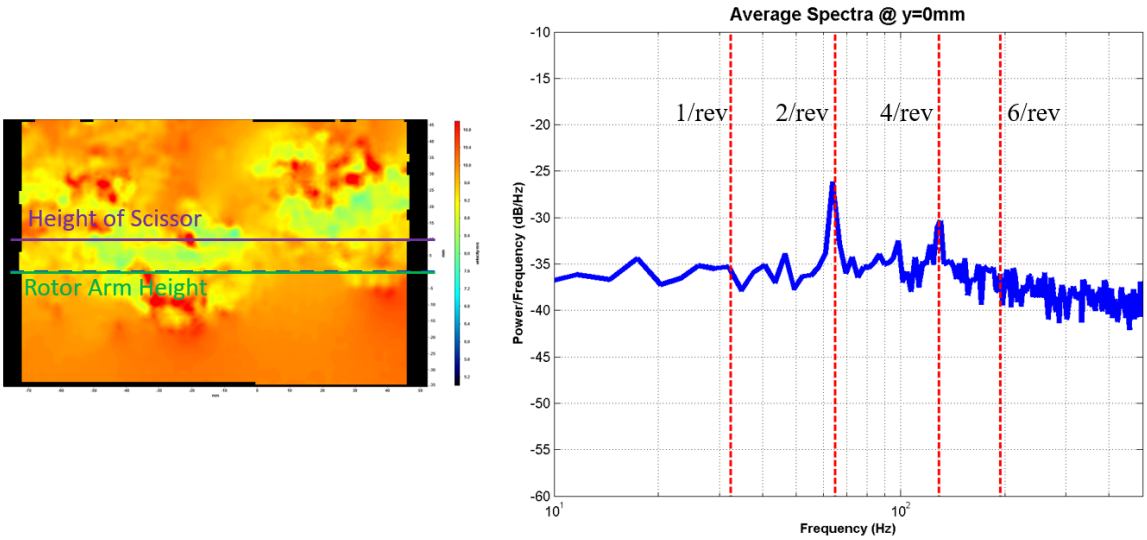

Figure 3.4: FFT at y = 0 mm (Rotor Arm Height)

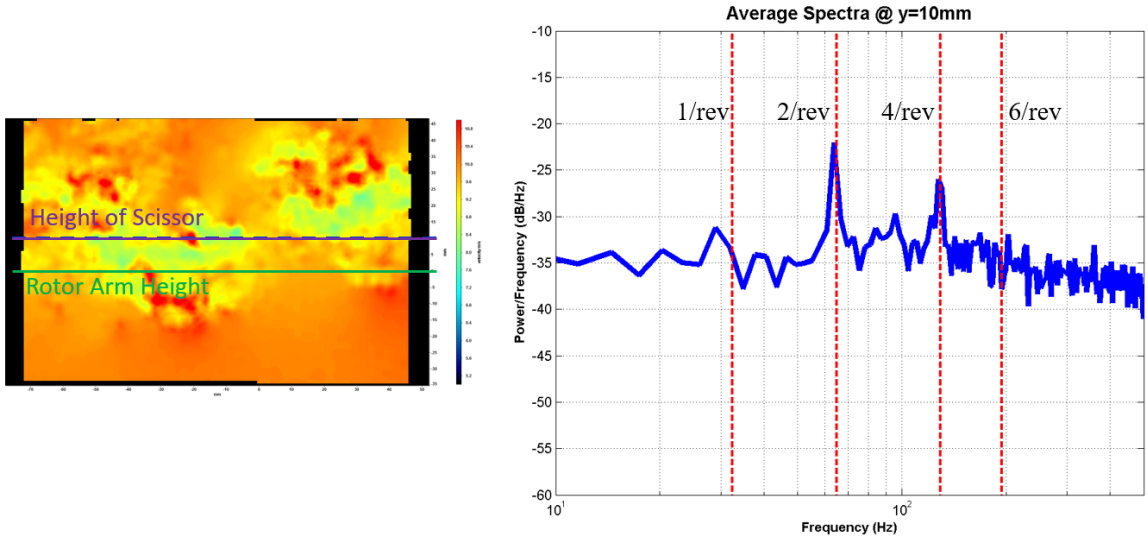

Figure 3.5: FFT at y = +10 mm (Scissor Link Height)

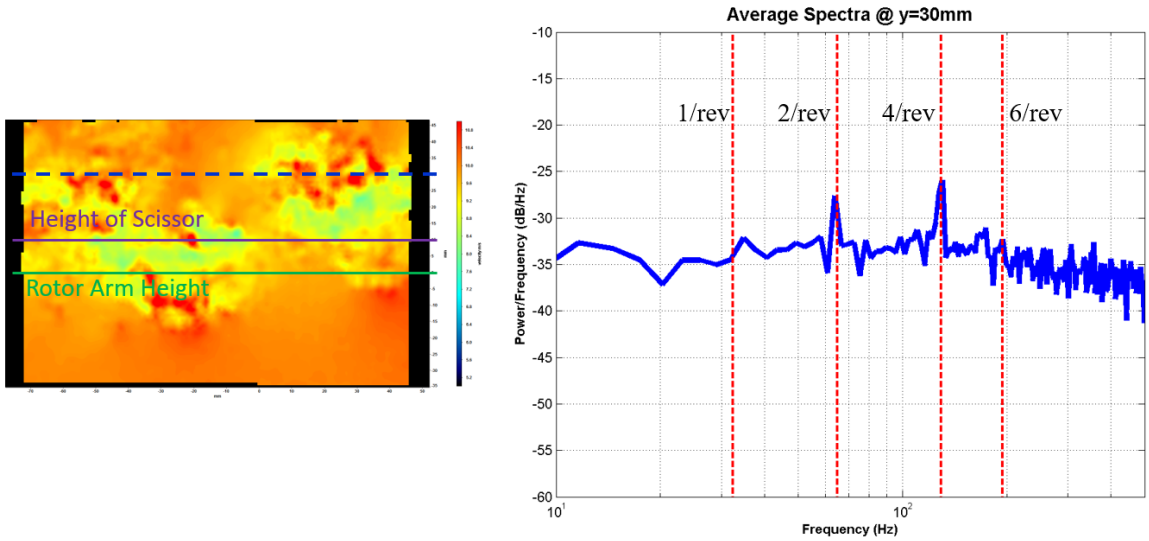

Figure 3.6: FFT at y = +30 mm (Behind Fairing)

As can be seen in Figure 3.3, the signal sampled below the hub (nearer to the freestream) does not display any fluctuations that are significantly stronger at any frequency. Instead, small-scale fluctuations, most likely due to turbulence and measurement noise, occur over the entire frequency spectrum, as is expected in the freestream far downstream of the hub. Behind the hub and fairing, however, clear 4/rev and 2/rev fluctuations exist in the wake. Interestingly, the 2/rev signal is dominant over the 4/rev immediately in the wake, and remains so for the entire wake centered behind the hub, only diminishing in the wake behind the fairing. This might hint that the 2/rev decays slowly compared to the 4/rev, as was observed in Reich et al. (2014, [12]). However, it is important to note that cavitation on the advancing blade shank was observed visually and recorded using the upstream monitoring camera (shown in Figure 3.7). This could have diminished the strength of the 4/rev to begin with by distributing 4/rev energy to higher frequencies. Additionally, the geometry linked to the 2/rev fluctuations, the scissor links, possessed sharp corners while the rotor shanks, the 4/rev's geometric counterpart, had rounded corners. This, too, could have led to a weaker 4/rev. This means it is difficult postulate as to whether the 2/rev and 4/rev structures decay at different rates.

3.1.2 Summary: Time-Resolved Results

Overall, the presence of 4/rev and 2/rev fluctuations twice as far downstream than previous wake studies have examined implies their presence further upstream. Because both the 4/rev and the 2/rev were observed, this serves as initial evidence that simple geometry may be useful approximating hub flow. Note, though, that no significant 6/rev signal was observed. From the preliminary measurements, it is impossible to determine whether there was a more significant 6/rev signal further upstream which simply decayed or there was no strong 6/rev signal that existed in the first place. Moving forward, changing hardware and model failure allowed for

the changes described earlier to be made between the preliminary time-resolved and phase-averaged tests. In particular, the corners of the rotor shank profile were sharpened like the scissor links to better compare the 2/rev and 4/rev frequency strengths, while the material the models were made of was switched to aluminum.

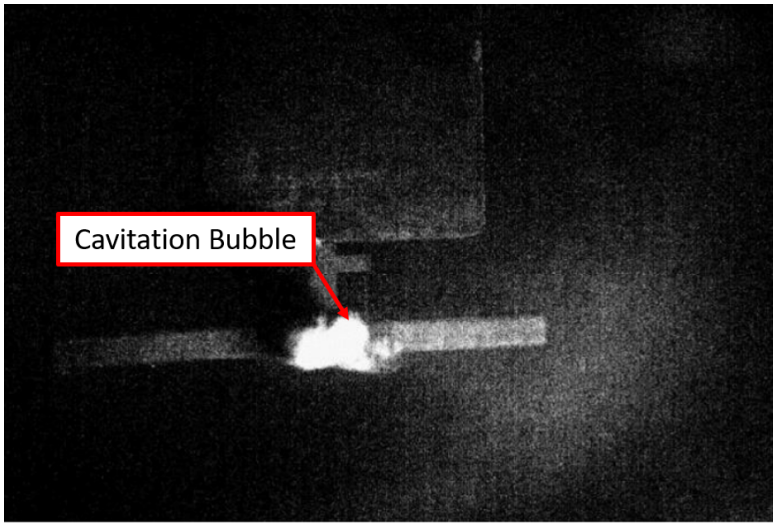

Figure 3.7: Cavitation bubbles forming over the advancing blade shank of the preliminary test model.

3.2 Results: Phase-Averaged Particle Image Velocimetry

3.2.1 Flow Field

An example contour field of the velocity magnitude from one phase of the phase-averaged data is shown in Figure 3.8, as an illustration of the vector spacing of data. This example is smaller than the full field of view, having been magnified to make the vector spacing more discernable. Additionally, in Figure 3.9, vertical profiles of the streamwise velocity of the averaged wake (all of the phases averaged together) are shown for comparison to previous work. Shown again in Figure 3.10, with the vertical axis is rescaled to the hub radius and the axis flipped to match data from Reich et al. (2014, [12]), which is shown as well in Figure 3.11. As can be seen, the deficit both

wakes, while not identical, are comparable to the previous wake studies. These three figures serve to show the better spatial resolution acheived in the current work. They also show that only a portion of the wake had been observed previously, meaning important frequency content may have been missed, especially in areas downstream of the hub-fairing interface.

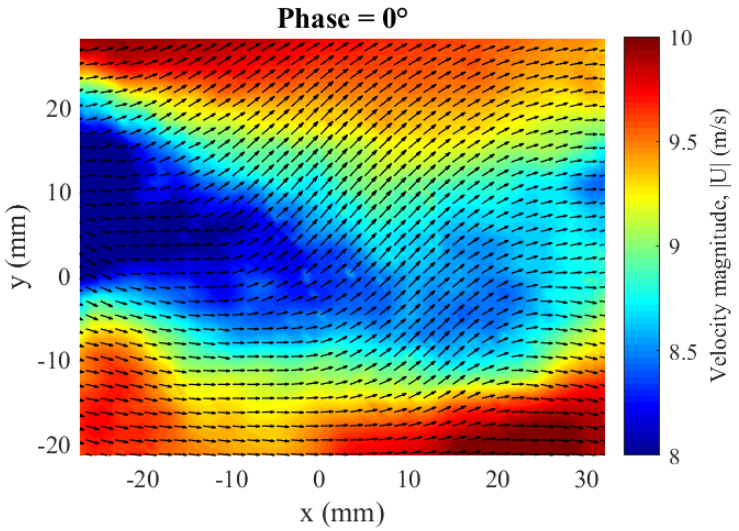

Figure 3.8: Example phase-averaged contour field.

A panorama of both components of velocity in the wake each of the models tested in the second experiment are shown in Figures 3.12 and 3.13. Remember that the y-axis, the vertical coordinate axis, is defined from the vertical location of the center of the rotor blade shanks, with more negative values indicating positions further into the freestream and more positive values indicating positions behind the hub and fairing. Also note that the y-axis has been scaled to h, the spacing between the rotor blade shanks and the scissor links, taken to be 10 mm (0.4 in). In both sets of contours, 4/rev flow structures may be observed in both components of velocity. Due to the higher contrast, the vertical contours of both sets are displayed next to each other in Figure 3.14. From these panoramas, looking left to right, the second and fourth vertical velocity structures appear to vary based upon the phase of the scissor

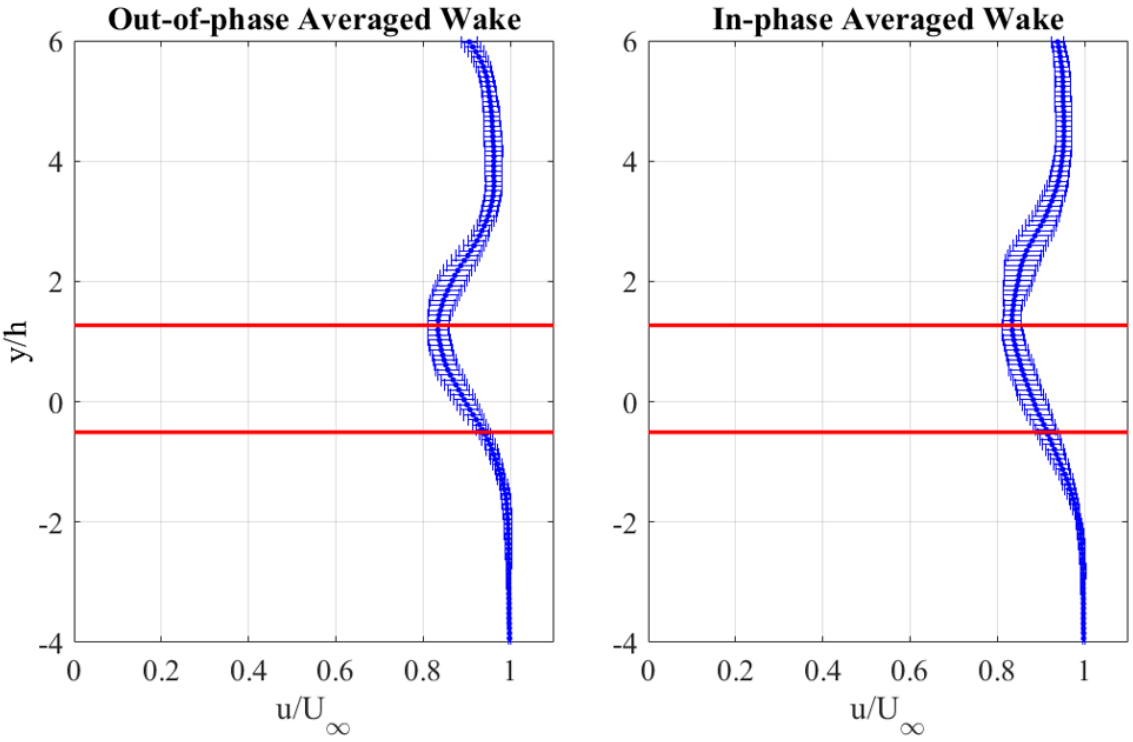

Figure 3.9: Streamwise velocity profiles in the vertical direction. Data scaled to the height difference between the rotor shanks and the scissor links. Red lines indicate data range presented in Figure 3.10.

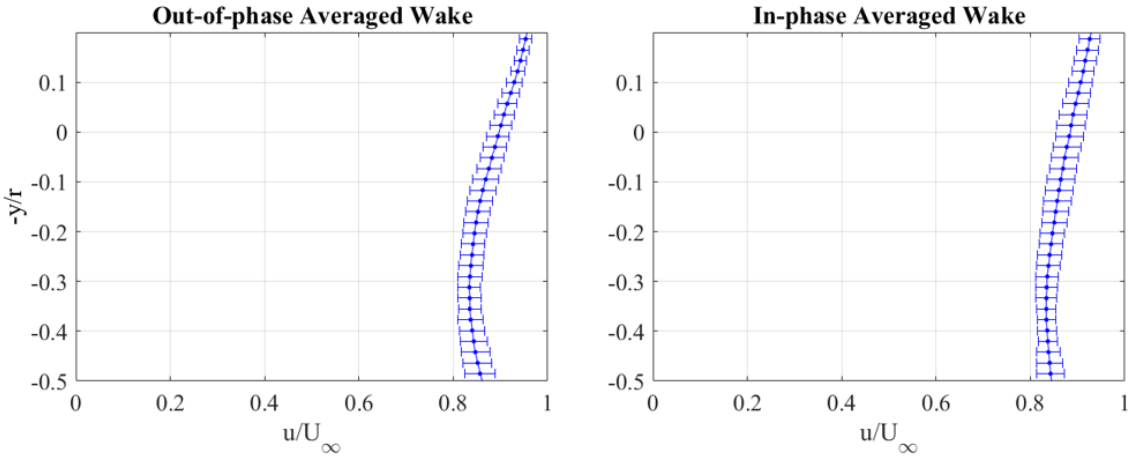

Figure 3.10: Streamwise velocity profiles in the vertical direction. Data scaled to the hub radius, and y-axis direction flipped for easier comparison to the data from Reich et al. [12], as shown in Figure 3.11.

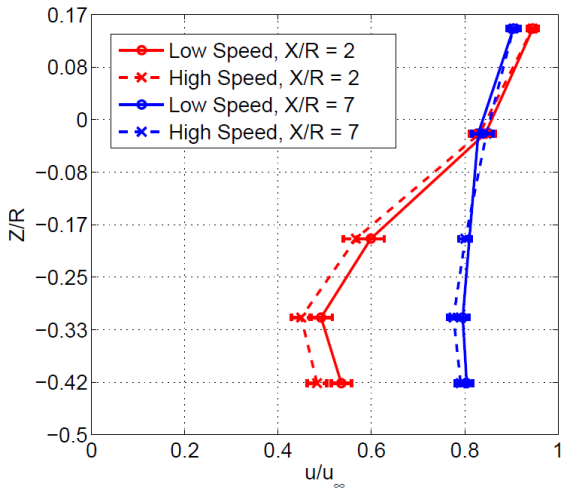

Figure 3.11: Streamwise velocity profiles from Reich et al. (Figure 3.11 in source [12]). Of interest here are the two 'X/R = 7' trendlines marked in blue. Data shown in Figure 3.10 match a similar deficit profile.

links in the model, with those structures in the wake behind the out-of-phase model displaying less coherence than those of the in-phase model. Note that the beginning phase of the panorama is arbitrary. Thus, the differences in phase location of each of the vertical structures is not indicative of a change made to the wake by the phase of the scissor links. Finally, to give a better sense of the vertical spacing involved, a spliced schematic of the wake within the context of the size of the hub is shown in Figure 3.15

As a potentially useful aside, these panoramas were constructed using Taylor's hypothesis (the "frozen turbulence approximation") (1938, [29]), as shown in Eq. 3.1, which assumes that advection is due mainly to mean flow. This assumption is valid if the turbulence intensity is sufficiently low, but can fail for free-shear flows, as mentioned by Pope (2000, [30]). As shown in the figures for the averaged wake (Figures 3.9 and 3.10), the standard deviation of the streamwise velocity in the wake is 5% or less, indicating that Taylor's hypothesis may be applied to the helicopter

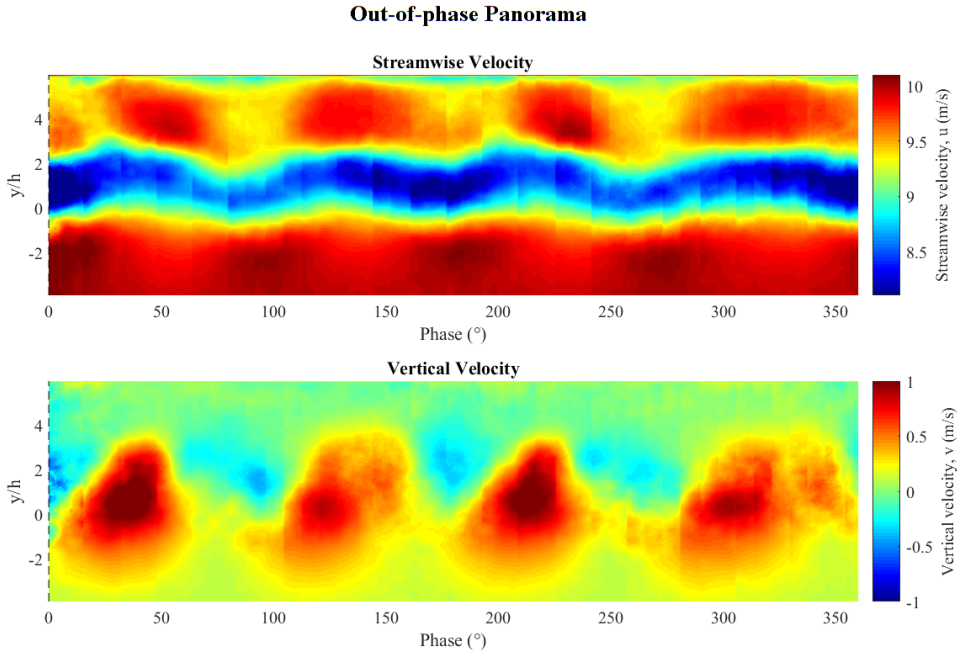

Figure 3.12: Phase panorama of the out-of-phase scissor link model wake

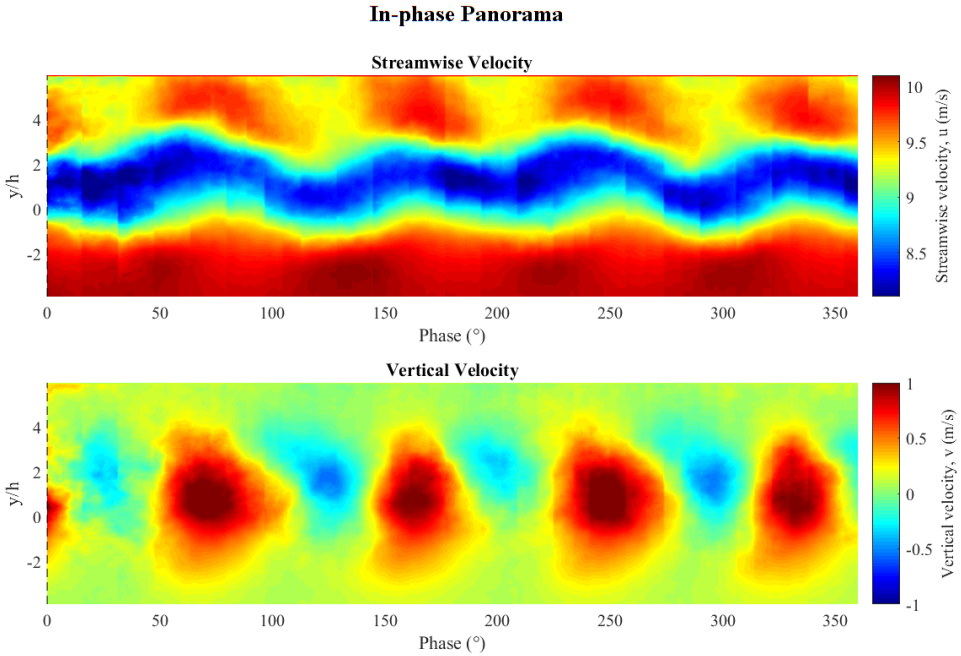

Figure 3.13: Phase panorama of in-phase scissor link model

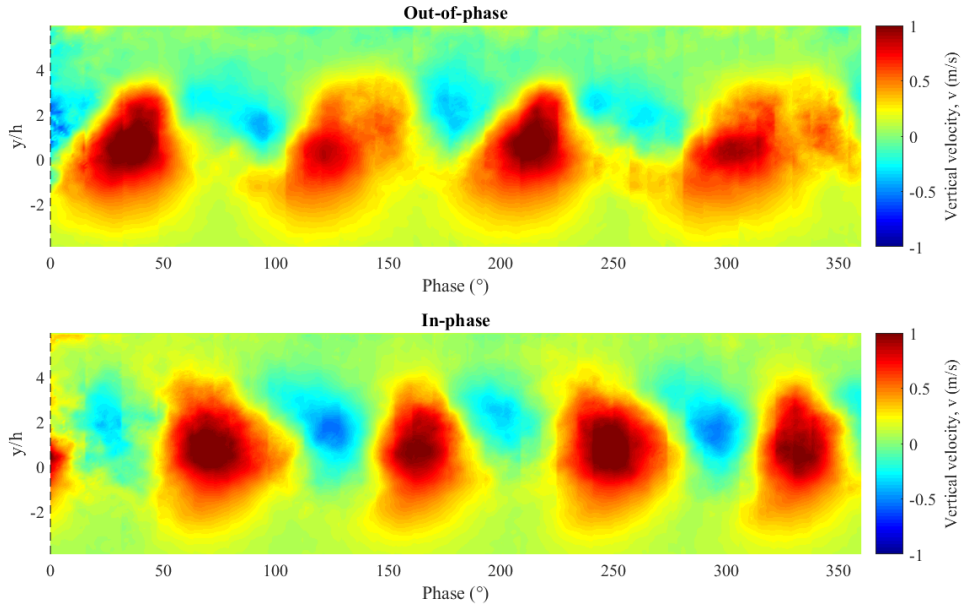

Figure 3.14: Vertical velocity phase panorama of both models

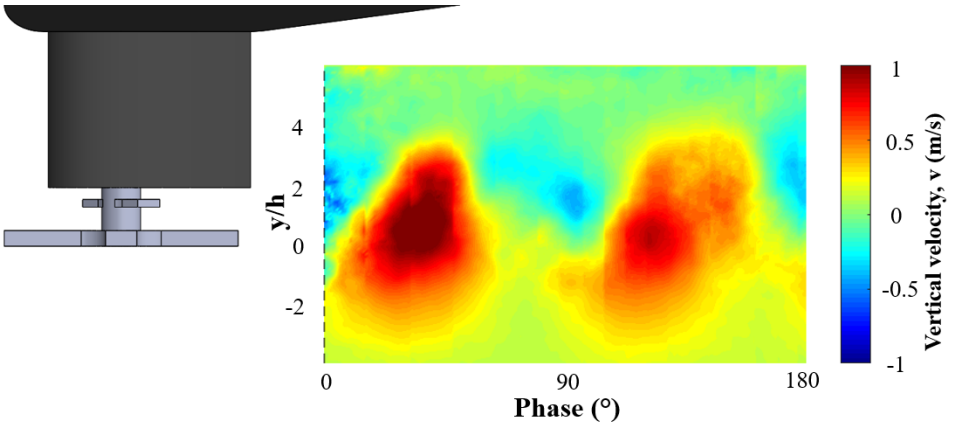

Figure 3.15: Cartoon to give a sense of the vertical scale of the panoramas shown.

Table 3.1: Binning process to create the phase panoramas

Vectors	**1**	**2**	**3**	**...**
Phase #1 Bins	0	$\frac{dx}{U_c}$	$\frac{2dx}{U_c}$	...
Phase #2 Bins	dt	$dt + \frac{dx}{U_c}$	$dt + \frac{2dx}{U_c}$	...
Phase #3 Bins	$2dt$	$2dt + \frac{dx}{U_c}$	$2dt + \frac{2dx}{U_c}$	...
...	...	...	...	...

rotor hub wake flow field. To create the panoramas, a constant convection velocity, U_c, was found by averaging the streamwise velocity at all streamwise locations for one vertical location ($y/h = 0$). By using the vector spacing, dx, and the time lag set in the Hall sensor/phase synchronizer, dt, the vectors for each phase-averaged vector field were binned into a time spacing, as illustrated in Table 3.1. The contour panoramas were created by averaging these bins, and using the measured frequency of the hub to convert each time bin into a phase.

$$\delta t = \frac{\delta x}{U_c} \iff \frac{u'}{U} << 1 \tag{3.1}$$

3.2.2 Spectral Analysis

To determine the spectral content of the wake, the points of the panorama were used as a trace input to an FFT. By applying the inverse frozen turbulence approximation, the wavenumber-domain spectra, $S_{uu}(k)$, were found. A sample of these traces for each model is shown in Figure 3.16, and sample wavenumber spectra of the same traces (and their vertical velocity counterparts) are shown in Figure 3.17. Before direct comparison to the spectra observed at PSU at "high-speed" test condition for the 24-inch model ($Re_{hub} = 4.9 \times 10^6$), a brief survey of the wake spectra is presented in Figures 3.18 (streamwise) and 3.19 (vertical). As a reminder, previous studies observed a 'flip' in amplitude dominance from the 4/rev signal to 2/rev signal

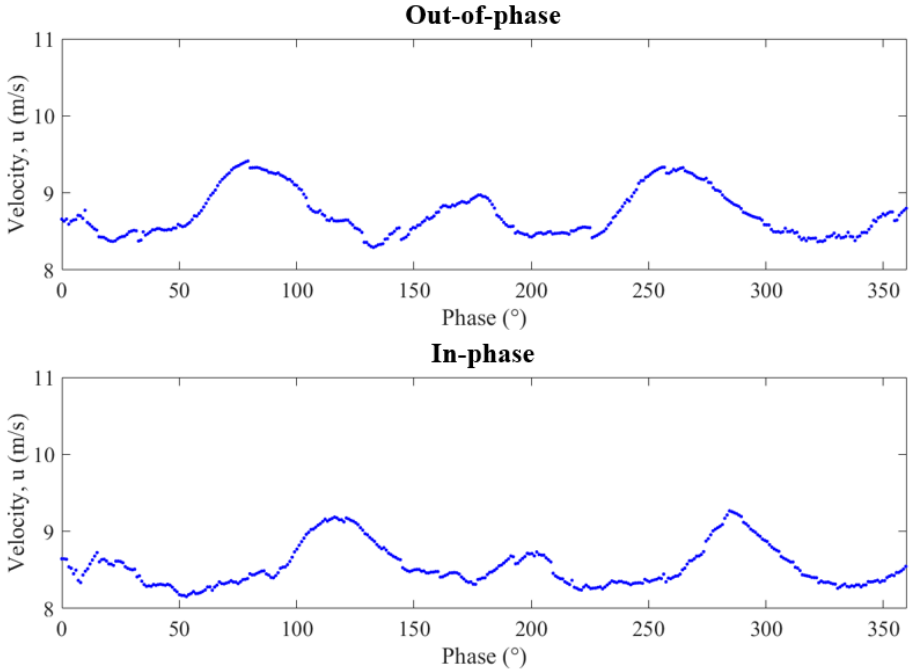

Figure 3.16: Example streamwise velocity trace for both models

in the wake directly downstream of the hub. In particular, this flip was observed when traversing from the rotor shank height towards the scissors and bottom of the hub. A similar flip can be observed twice in the streamwise spectra presented in Figure 3.18. First, between the rotor shank height ($y/h = 0$) and the scissor link height ($y/h = +1$), the same flip in dominance from 4/rev to 2/rev is seen. Next, the reverse flip (from 2/rev back to 4/rev) is seen between the scissor link ($y/h = +1$) and the hub-fairing interface ($y/h = +2$). The wake at this location was not previously measured by PSU. No similar trends are found in the vertical velocity spectra (Figure 3.19), with the 4/rev remaining dominant through the wake, though the other frequency harmonics do exhibit a growth in amplitude behind the hub. Of important note, at $y/h = +2$, the 6/rev harmonic is of the second greatest amplitude in the spectrum, overtaking both 2/rev and 8/rev.

To aid in direct comparison between the current work and previous results, the vertical velocity spectra reported by Reich et al. (2014, [12]) is shown in Figure

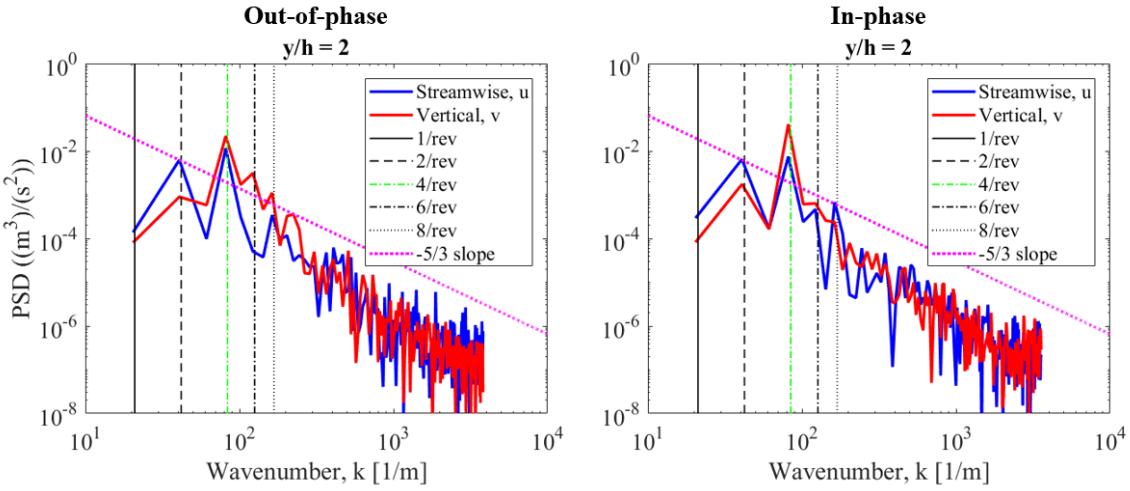

Figure 3.17: Example wavenumber spectra for both models

3.20, rescaled in the current coordinate system. The black bars are the experimental data in question. As can be seen, the vertical span examined in previous works is under half of the size of the spectra just presented in Figures 3.18 and 3.19, which were representative of about 40% of the vertical span measured in the current work. Figures 3.21 and 3.22 show streamwise and vertical velocity spectra (respectively) of the current work, side-by-side with those from Reich et al. (2014, [12]). In the streamwise spectra, the dominance flip between from the 4/rev dominance to the 2/rev structure is observed, albeit at a slightly greater height ($y/h = +0.9$ for the out-of-phase model and $y/h = +1.2$ for the in-phase model, compared to $y/h = +0.3$ for PSU model). The location of the flip for both the in-phase and out-of-phase models corresponds to roughly the scissor height ($y/h = +1$). Similarly, $y/h = 0$ corresponds to the height of the rotor shanks, and shows a 4/rev dominance. Unlike previous results, however, the 2/rev is very weak in the 4/rev dominance zone, while the 4/rev is very weak in the 2/rev dominance zone (the extremes of the heights shown in Figure 3.21. Also unlike previous results, the 6/rev does not appear to be strong in this vertical range. In the vertical velocity spectra shown by Figure 3.22, there is no flip in signal strength, with the 4/rev remaining the strongest frequency

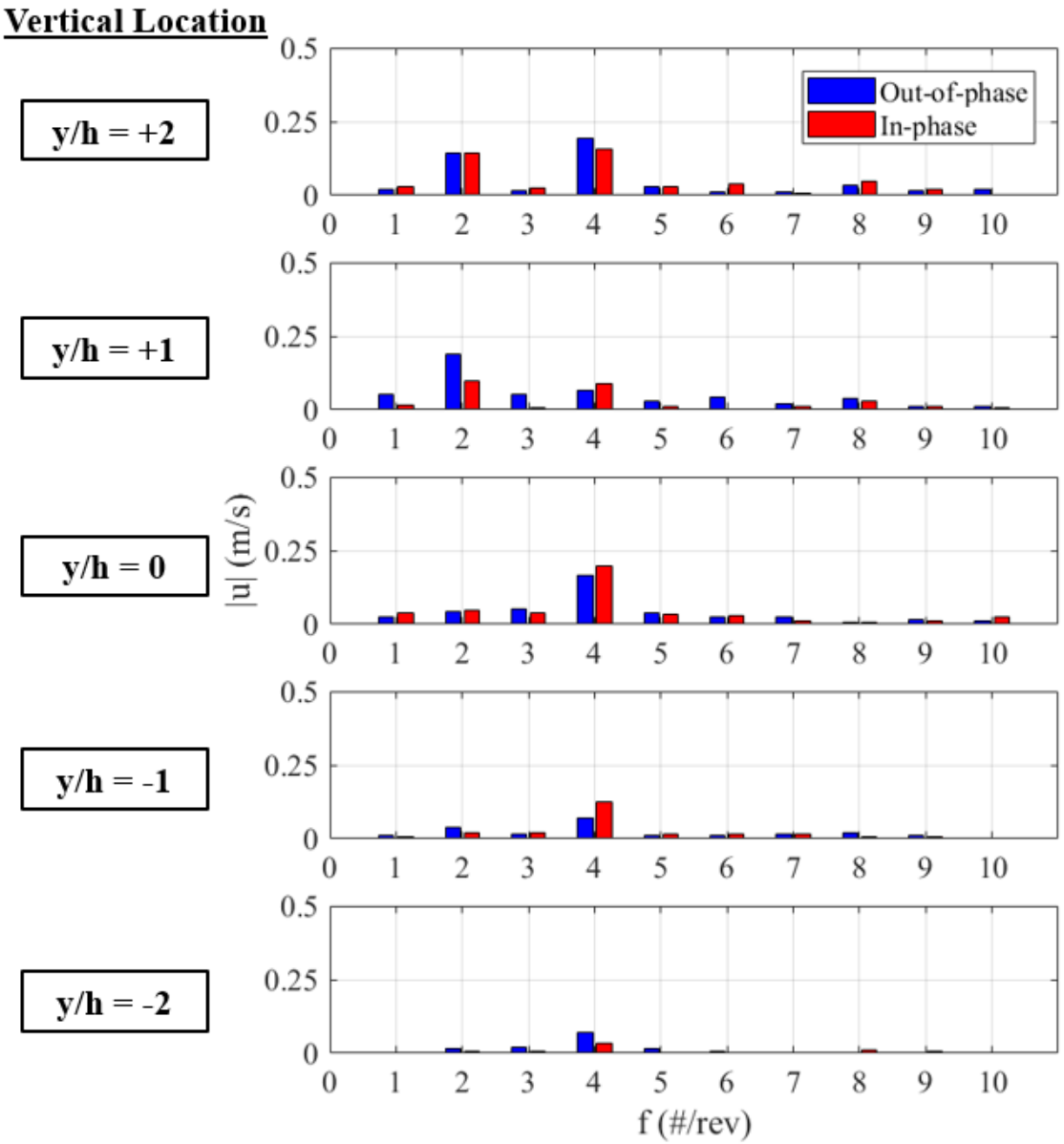

Figure 3.18: Streamwise velocity spectra for both models at a variety of vertical distances.

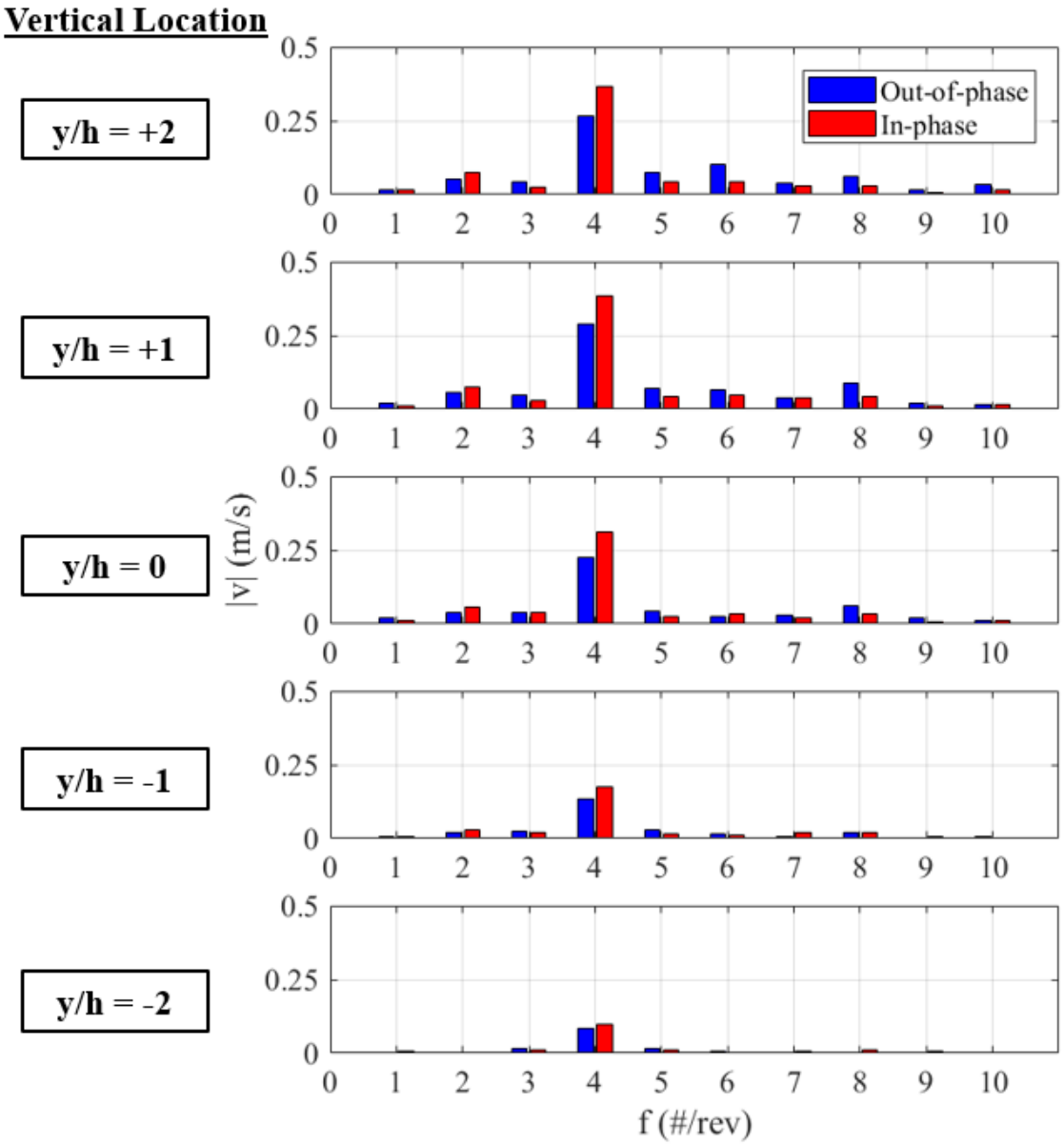

Figure 3.19: Vertical velocity spectra for both models at a variety of vertical distances.

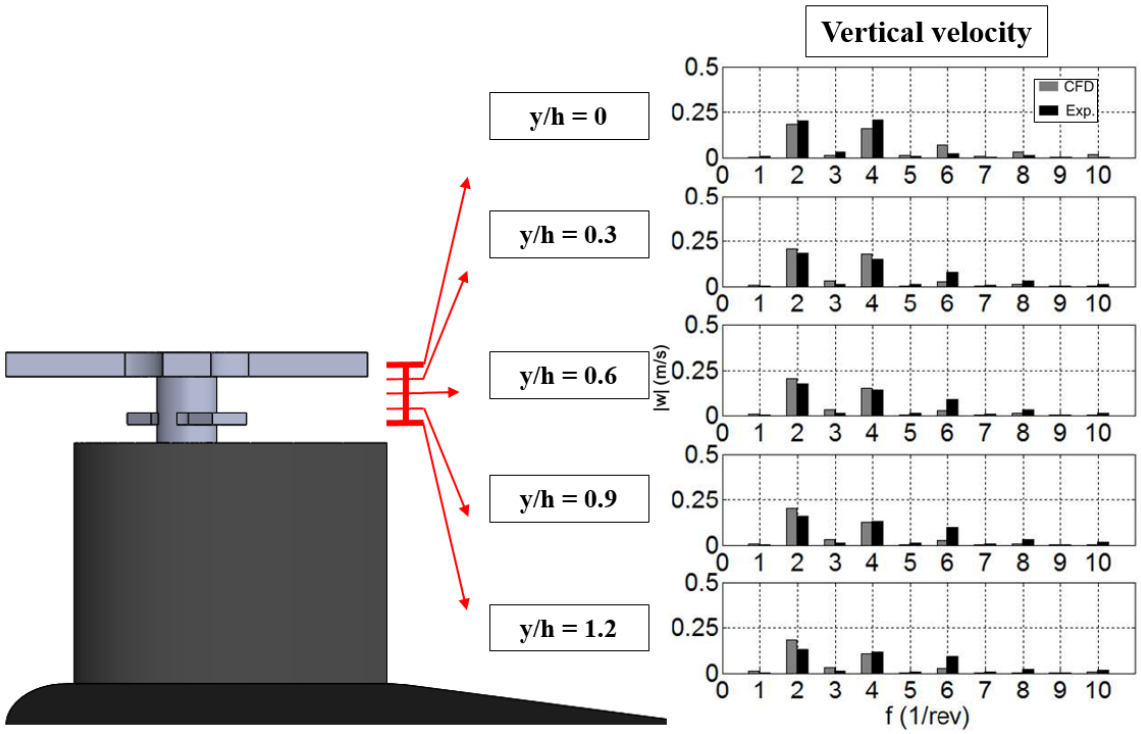

Figure 3.20: Vertical velocity spectra reported in Reich et al. (2014, [12]), rescaled in the current coordinate system. A diagram of the hub model of the current work is included to aid in determining the vertical distances involved.

component across the height of the hub. For the out-of-phase model, a slight 8/rev harmonic is seen.

The full vertical distribution of relevant spectral content (2/rev, 4/rev, 6/rev, with 8/rev for reference) in the measured wake of the out-of-phase model is shown in Figure 3.23 (streamwise velocity) and Figure 3.24 (vertical velocity). Similarly, the spatial distribution of the spectral content of the wake of the in-phase model is shown in Figure 3.25 (streamwise) and Figure 3.26 (vertical). Focusing first on the out-of-phase model, the streamwise spectra show a complex interchange in the streamwise component. For most of the wake, the 4/rev frequency component remains the largest amplitude. However, it experiences a sharp deficit centered around $y/h = +1$, the height of the scissor geometry, where the 2/rev component experiences its highest

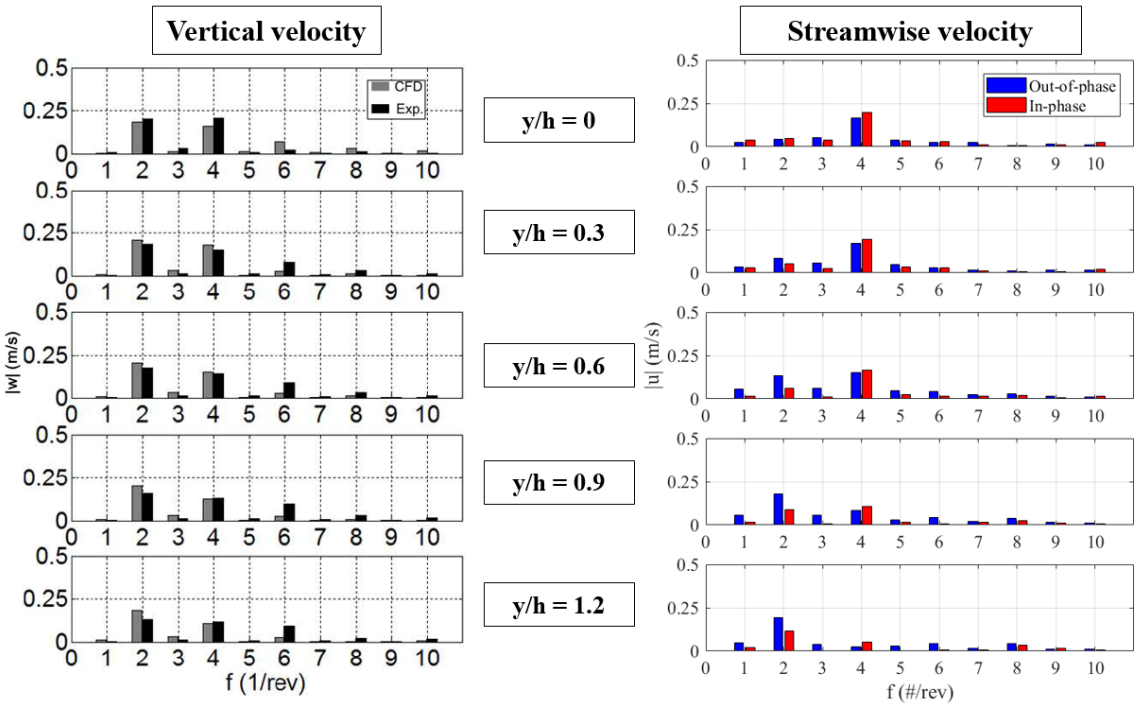

Figure 3.21: Vertical velocity spectra reported in Reich et al. (2014, [12]) compared to streamwise velocity spectra of the current work at the same height.

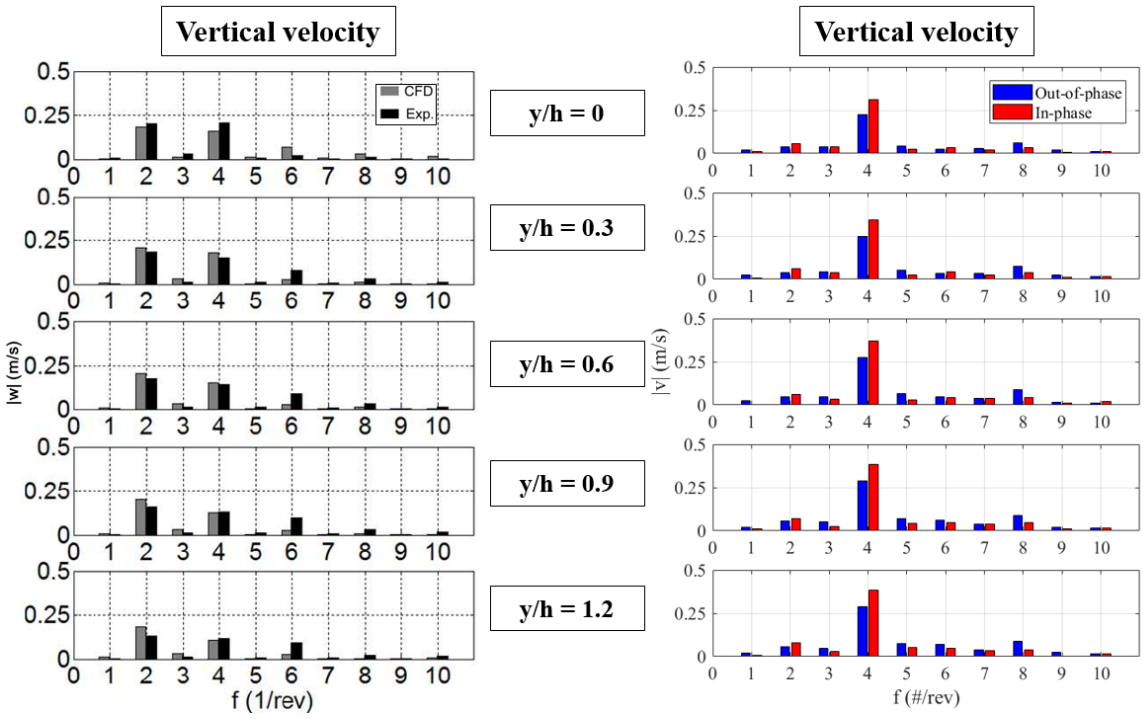

Figure 3.22: Vertical velocity spectra reported in Reich et al. (2014, [12]) compared to vertical velocity spectra of the current work at the same height.

amplitude. A peak in the 4/rev is observed both one scissor height above and one scissor height below the 2/rev peak (i.e. 4/rev peaks at $y/h = 0$ and $y/h = +2$), better displaying the double flip observed from the spectra earlier in this chapter. Aside from the amplitude flipping behavior, Figure 3.23 shows that the 6/rev component is the strongest frequency at $y/h = +3$. This vertical location corresponds to a spot behind the fairing, just above the interface between the fairing and the hub model. A secondary, though not dominant peak of 6/rev can be seen near the scissor link height as well $y/h = +1$. The vertical velocity spectra of the out-of-phase model shown in Figure 3.24 also show intriguing trends; here, the 4/rev remains the largest component by far, with a peak near $y/h = +1$, wile 2/rev component is never dominant, and only briefly larger than both the 6/rev and 8/rev content at heights closer to the wall ($y/h > +3.5$). However, a coherent 6/rev peak may be noted near $y/h = +2$, larger than all other harmonics besides the 4/rev. A similar 8/rev peak is found at $y/h \approx +1$, which is unsurprising if it is a harmonic of the 4/rev.

Looking next at the streamwise spectra in the wake of the in-phase model, shown by Figure 3.25, the 4/rev content shows a very similar trend to that of the out-of-phase model, with two peaks centered at $y/h = 0$ and $y/h \approx +2$, respectively, and a very sharp deficit near the scissor link height at $y/h = +1$. The 2/rev also shows a similar trend, in that it has a peak. The peak is far less coherent in the wake of the in-phase model, and it is shifted away from the scissor link height, closer to the hub-fairing interface at $y/h = +2$. For the 6/rev distribution, the in-phase model's wake is markedly different than that of the out-of-phase. Rather than a peak at $y/h = +3$, it displays a valley, and is never the dominant frequency component in the wake. The vertical velocity spectra of the in-phase model also vary from the out-of-phase. As seen in Figure 3.26, all of the relevant frequency content, except possibly the 8/rev, of the vertical spectra experiences a peak near $y/h = +1.5$, and for the most part, remains ordered in amplitude with the 4/rev being the vastly dominant frequency,

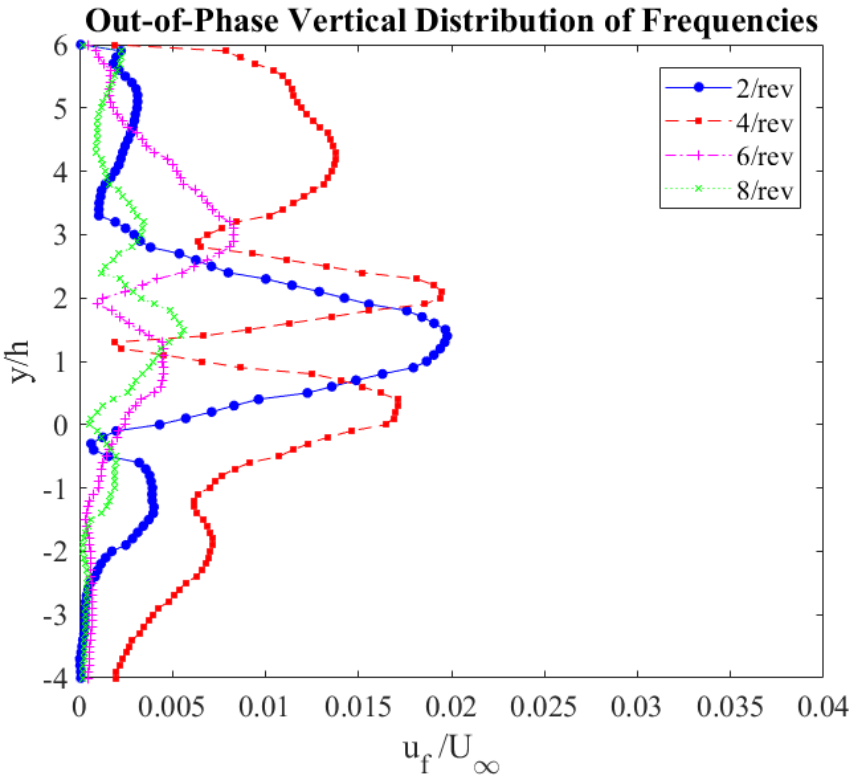

Figure 3.23: Vertical distribution of streamwise velocity spectra in the wake of the out-of-phase model.

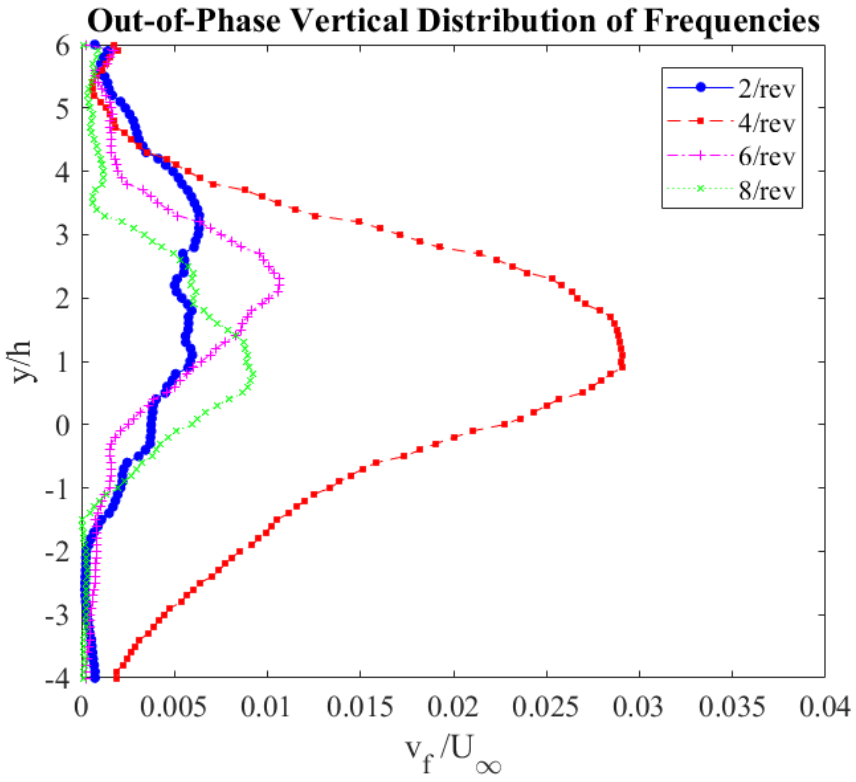

Figure 3.24: Vertical distribution of vertical velocity spectra in the wake of the out-of-phase model.

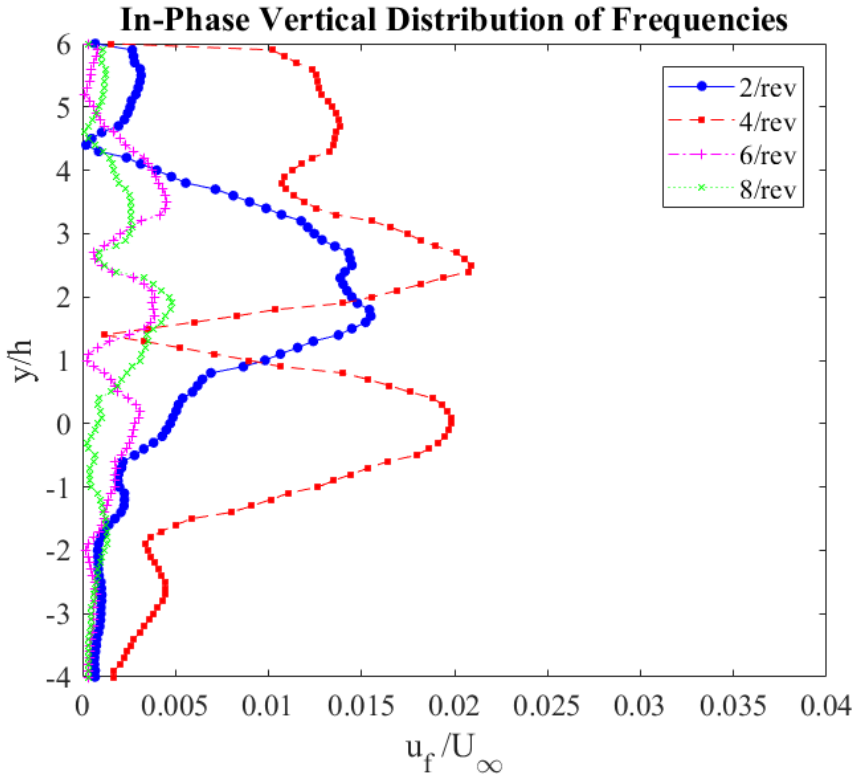

Figure 3.25: Vertical distribution of streamwise velocity spectra in the wake of the in-phase model.

followed far behind by the 2/rev, and then the higher order frequencies.

To better draw out the differences in frequency distribution between each model, Figures 3.27 through 3.32 display the spatial distribution of streamwise and vertical velocity components for the 2/rev, 4/rev and 6/rev fluctuations. In Figure 3.27, the difference in peak coherence between the out-of-phase and in-phase models is much more prominent, with the model with out-of-phase scissors displaying a larger and more coherent streamwise 2/rev peak. Conversely, the in-phase model wake seems to display the slightly more coherent peak in 2/rev vertical fluctuations, as shown in Figure 3.28, though both of the peaks are very weak. As observed previously, the 4/rev components display very similar trends in both velocity components (Figures 3.29 and 3.30). In both components, the 4/rev distribution trends of the in-phase

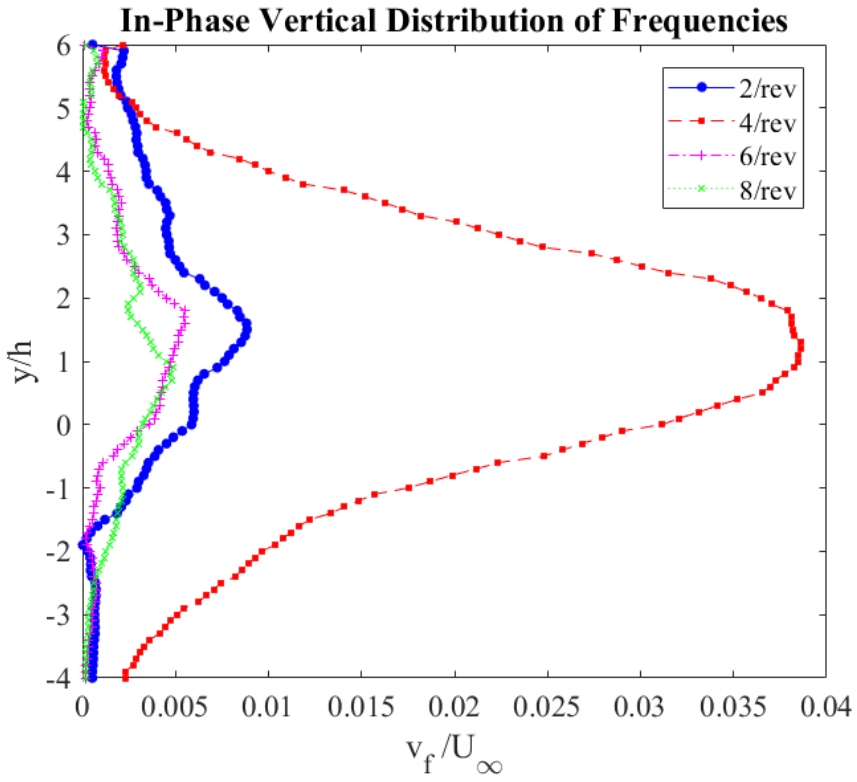

Figure 3.26: Vertical distribution of vertical velocity spectra in the wake of the in-phase model.

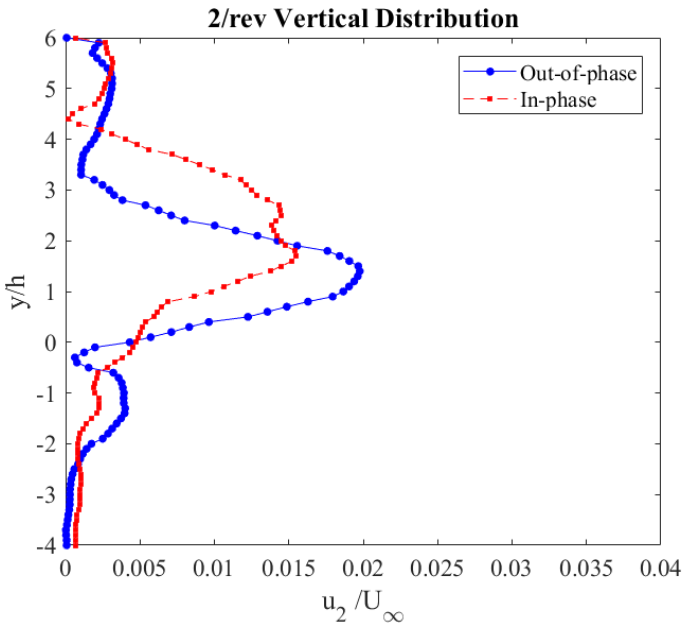

Figure 3.27: Comparison between models of spatial distribution of streamwise 2/rev fluctuations.

occurs over a larger vertical range, but display greater amplitudes than those of the out-of-phase model. Of note, the location of the sharp streamwise deficit is nearly identical for both, occuring at $y/h \approx +1$, the approximate location of the scissor geometry, while the peak of the vertical velocity occurs at the same location. Finally, Figures 3.31 and 3.32 confirm that the 6/rev content of the wake behind the out-of-phase model is noticeably stronger than that of the in-phase model in both velocity components. Strangely, the streamwise components display an almost inverse trend: at $y/h = +1$ (the height of the scissor link geometry), a small peak occurs in the wake of the out-of-phase model, while a valley occurs in the in-phase model. The opposite is true at $y/h = +2$.

3.2.3 Summary: Phase-Averaged Results

From the phase-averaged data, some similar trends in 2/rev and 4/rev velocity have been identified between the streamwise velocity of both models tested and the vertical

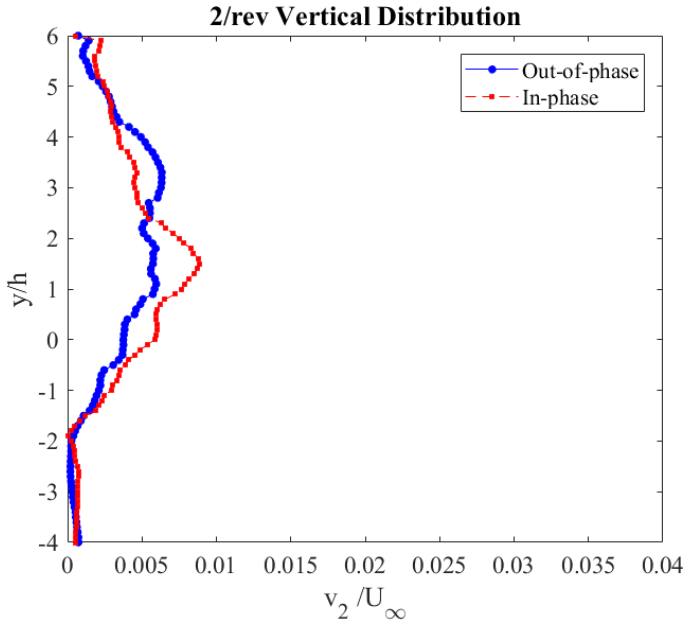

Figure 3.28: Comparison between models of spatial distribution of vertical 2/rev fluctuations.

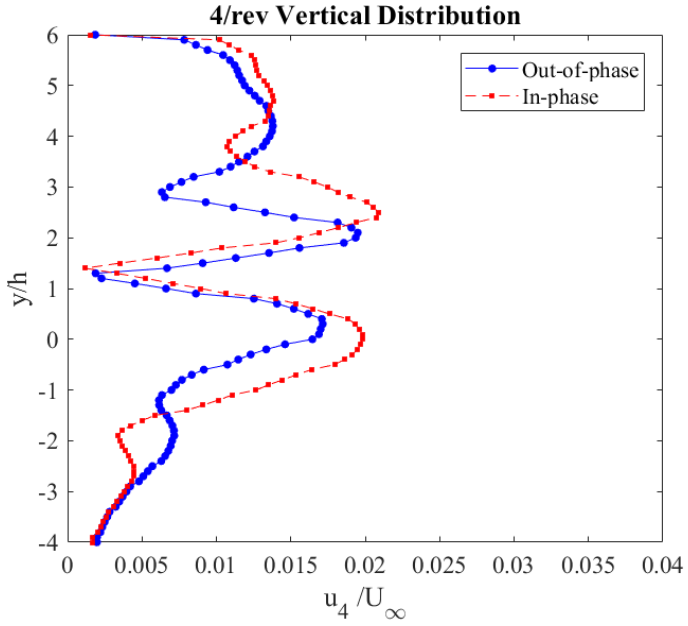

Figure 3.29: Comparison between models of spatial distribution of streamwise 4/rev fluctuations.

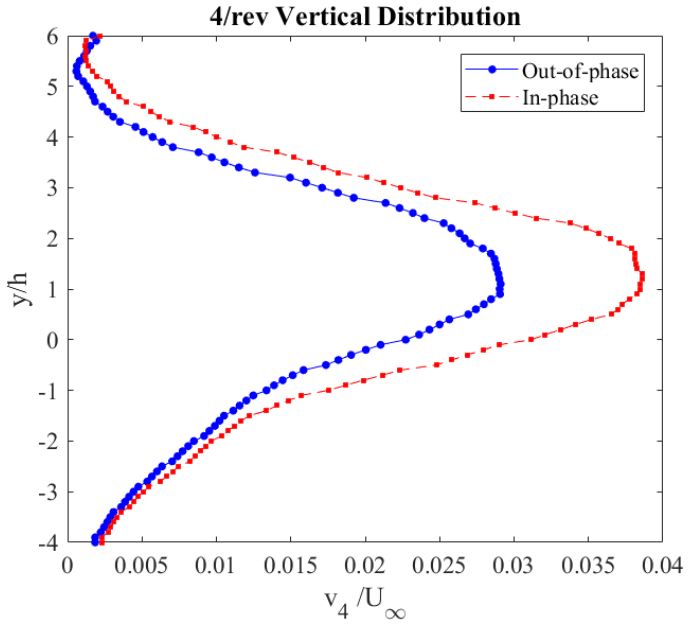

Figure 3.30: Comparison between models of spatial distribution of vertical 4/rev fluctuations.

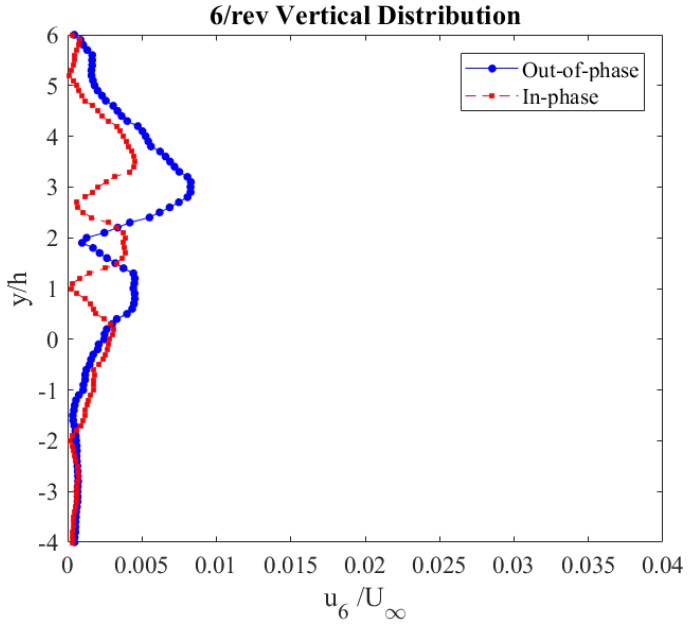

Figure 3.31: Comparison between models of spatial distribution of streamwise 6/rev fluctuations.

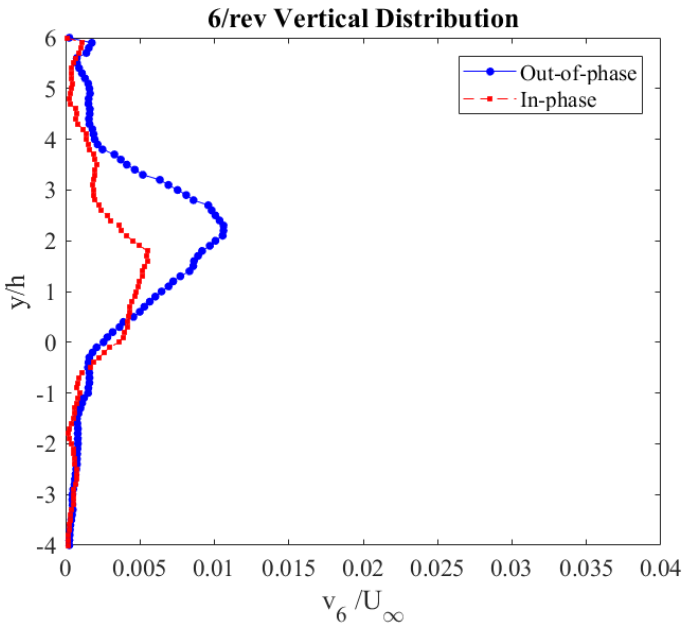

Figure 3.32: Comparison between models of spatial distribution of vertical 6/rev fluctuations.

velocity results reported in Reich et al. (2014, [12]). The location and magnitude of the streamwise wake deficit for both models is close to that of the PSU model, and both 2/rev and 4/rev fluctuations were observed over similar heights. In the current work, however, the same trends were not seen in the vertical velocity components. In addition, the contrast in streamwise amplitude between the 2/rev and 4/rev is greater for the current work than it was in Reich et al. (2014, [12]). As a final comparison to previous studies, a 6/rev velocity fluctuation was observed for one of the models, though it was not observed at the same vertical location as previous studies.

In addition, very clear differences were observed between the wake behind the two models, whose only significant geometric difference was the phase angle of the scissor links. Generally speaking, the 2/rev fluctuations for the out-of-phase scissor model showed a more coherent streamwise-velocity wake and a less coherent vertical-velocity wake than those of the in-phase model. The 4/rev fluctuations displayed very similar trends in both models, though the streamwise wake of the out-of-phase

model was concentrated across a smaller vertical span, and displayed slightly weaker overall amplitudes. Finally, clear 6/rev peaks were observed only for the model with out-of-phase scissor geometry.

CHAPTER 4

CONCLUSIONS & FUTURE WORK

4.1 Conclusions

As discussed, prediction of frequency content in the wake of helicopter rotor hubs, particularly the experimentally observed 2/rev velocity component, is of immense importance to industry. Thus far, the closest to full-scale hub diameter-based Reynolds number hub wake data was collected using a defeatured and generalized model of a the rotor hub of a commercial helicopter hub (Reich, 2013, [14]; Reich et al., 2014, [12]; Reich et al., 2014, [13]), in which the expected 4/rev fluctuation, as well as a strong 2/rev fluctuation and a previously unpredicted 6/rev fluctuation were all observed. In the current work, both 2/rev and 4/rev fluctuations were observed at the same scaled-streamwise location (7 hub radii downstream) with similar amplitudes using a simpler geometry based on more canonical shapes, and operating at roughly 15% of the hub diameter-based Reynolds number. Furthermore, a 6/rev fluctuation was also observed, though at a different vertical location than that of previous studies. The 2/rev and 4/rev fluctuations were also observed to occur in the wake very far downstream (14 hub radii downstream), while the 6/rev was not seen. The appearance of similar spectral trends to previous experimental studies conducted at the Pennsylvania State University [12–15] has implications for both future experimentation and computational modeling. Because the hubs in the current work were operating at roughly 1/10th of the full-scale hub diameter-based Reynolds number, and at roughly 15% of that of the previous work, the frequency content observed in the current work indicates that the hub diameter may not be the ideal scaling parameter.

Additional Reynolds numbers based on the chords of local hub components have been reported, to aid in future scaling of results. In addition, these hubs may provide a much better validation case for CFD than previous studies. Due to their vastly simplified geometry, more computational power that was previously applied to complex hub geometries can be shifted to the wake, therefore increasing the computational resolution of the wake flow physics.

Beyond replication of previous results, the wakes of the two models showed key differences. As the only notable geometric change between the two models was the phase of the scissor tested show that the phase of the scissor link geometry plays a major role in the amplitude and vertical location of all frequency content in the wake. In the vertical velocity spectra, the out-of-phase scissor link geometry resulted in a significant 6/rev peak, while the in-phase geometry did not. However, this is not to say that the scissor link phase is the sole determinant in the appearance of the 6/rev fluctuation or the strength of the 2/rev and 4/rev fluctuations. As the 6/rev spectral component was observed downstream of the final fairing (as opposed to the fairing used in the preliminary, time-resolved test), the interface between the hub model and the fairing and the shape of the fairing itself may play a significant part in the creation of 6/rev flow structures. Also, as pointed out, it is also possible that 6/rev Strouhal shedding is a potential for the rotor mast of the model (note: not the rotary power shaft, which was faired, but the cylindrical portion of the model above the fairing). Because of geometric interference, it is not clear whether the rotor mast is operating before or in the critical regime of circular cylinder flow (nominally, a chord-based Reynolds number of 2×10^5), thus making it difficult to determine its Strouhal number.

Finally, the current work provides the largest vertical span of wake data behind a model rotor hub yet. While some parts of the observed wake may not have direct implications in helicopter design, experimental components previously considered some-

what extraneous like the fairing and the tunnel wall boundary layer may actually play a role in the strength and vertical location of frequency content observed in the wake of the model. It is therefore necessary to have an estimation of their effect to properly compare to previous results. As the most extensive vertical wake survey at the streamwise location of interest (7 hub radii downstream) so far, future studies may use the current work to compare the influence of the tunnel boundary layer and fairing design on the creation and strength of spectral content in the wake of the model hub.

The observation of frequency content similar to that of previous work, as well as the measurement of significant differences between these models signifies substantial progress towards the stated objective of this work: to create a model with simple and easily defined geometry based on canonical bluff body profiles that is capable of approximating hub flow, thus streamlining the process of parametric variation to uncover significant wake physics. However, for full completion of this objective, further work must be done.

4.2 Limitations & Future Work

A major shortcoming in the current work is the lack of a drag measurement. Because hub diameter-based Reynolds number similarity is currently thought to be of importance for properly replicating the hub drag (Reich et al., 2015, [15]), the potential direct advantage to hub modelling is limited. However, a drag measurement of the current hubs would provide further criteria for validation of computational methods, thus allowing the prediction methods to be tested on a simpler case before moving to more complicated geometries at higher Reynolds numbers.

Aside from incorporation of a drag measurement to the setup, a componenet build-up should be conducted. That is, each component of the hub should be tested in its simplest possible form. For example, it is currently unknown if the fairing

or rotor mast geometry is contributing to 6/rev fluctuations. Therefore, the fairing should be tested alone, followed by the combination of the fairing and the rotor mast, without the scissor links or blade shanks. By conducting a component build-up, a better estimation of the contribution of each component may be developed, as well as a better understanding of interference effects between the components. In a similar vein, the effect of local component chord-based Reynolds numbers should also be explored. The simplicity of the model geometry lends itself towards this end. If, for example, the scissor profiles were shortened in chord to match the same ratio as that of the blade shank, the resulting wake could be contrasted to the wakes presented here to estimate the sensitivity to chord-based Reynolds number. This approach may uncover a better scaling parameter than the hub diameter-based Reynolds number.

Finally, the current hubs should be re-tested at an angle of attack representative of forward flight. Previous works observed strong 2/rev, 4/rev and 6/rev frequency content in both streamwise and vertical velocity components, while the 4/rev essentially dominated the vertical velocity across the entire span of the wake in the current work. The difference may be due to the fact that previous studies have implemented a moderate angle of attack ($\sim 5^\circ$) on the hub models to better model forward flight, while the current models were not placed at an angle of attack. Therefore, to better model hub wake flow physics, the effect of the hub angle of attack should be explored.

APPENDIX A

Canonical Data for Common Bluff Bodies

All figures presented here are from Delany & Sorensen (1953, [18]). Note that b denotes the thickness of the profile, while r denotes the radius of the corner.

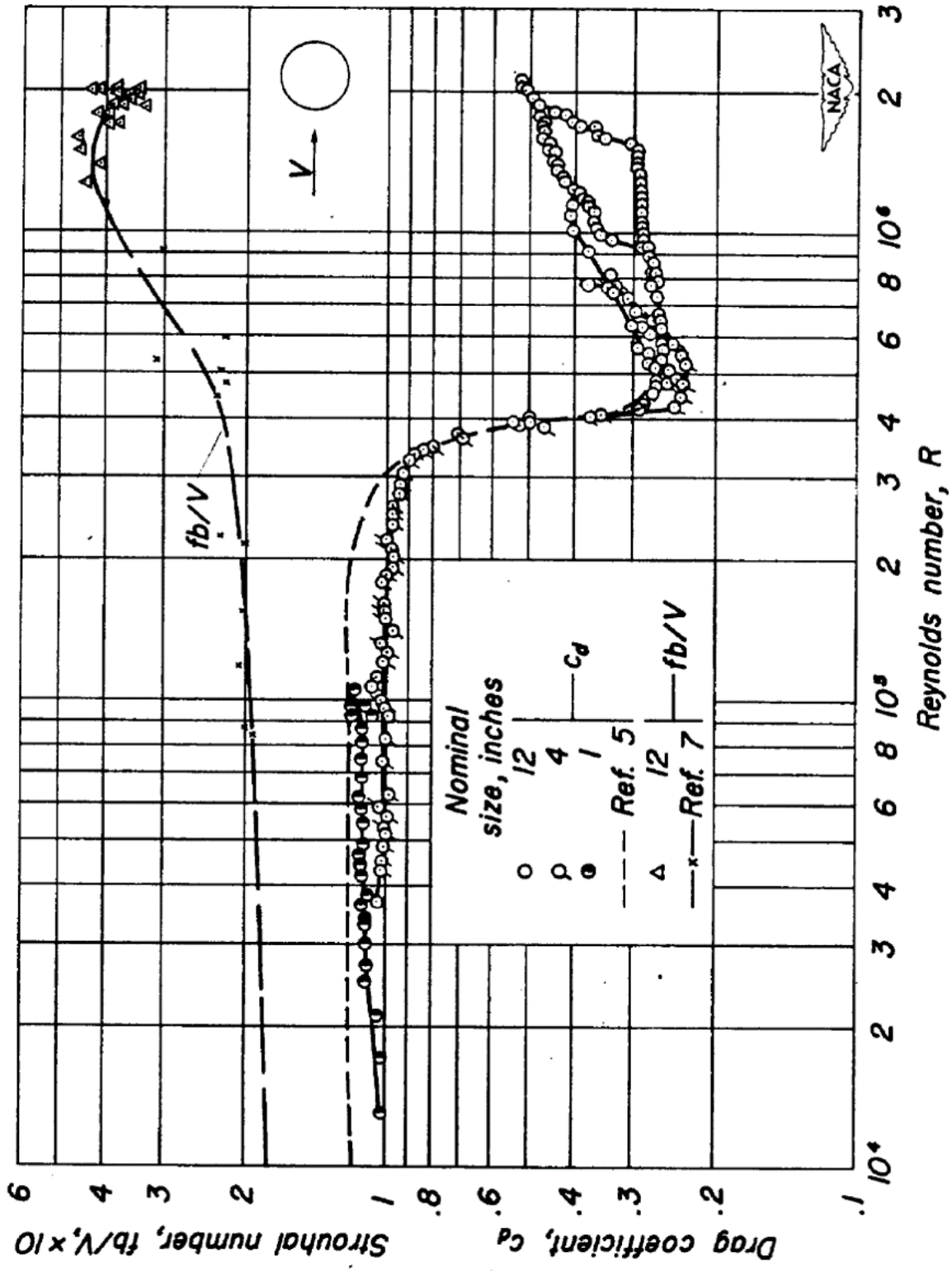

Figure A.1: Drag coefficient and Strouhal number variance with chord-based Reynolds number for a circular cylinder

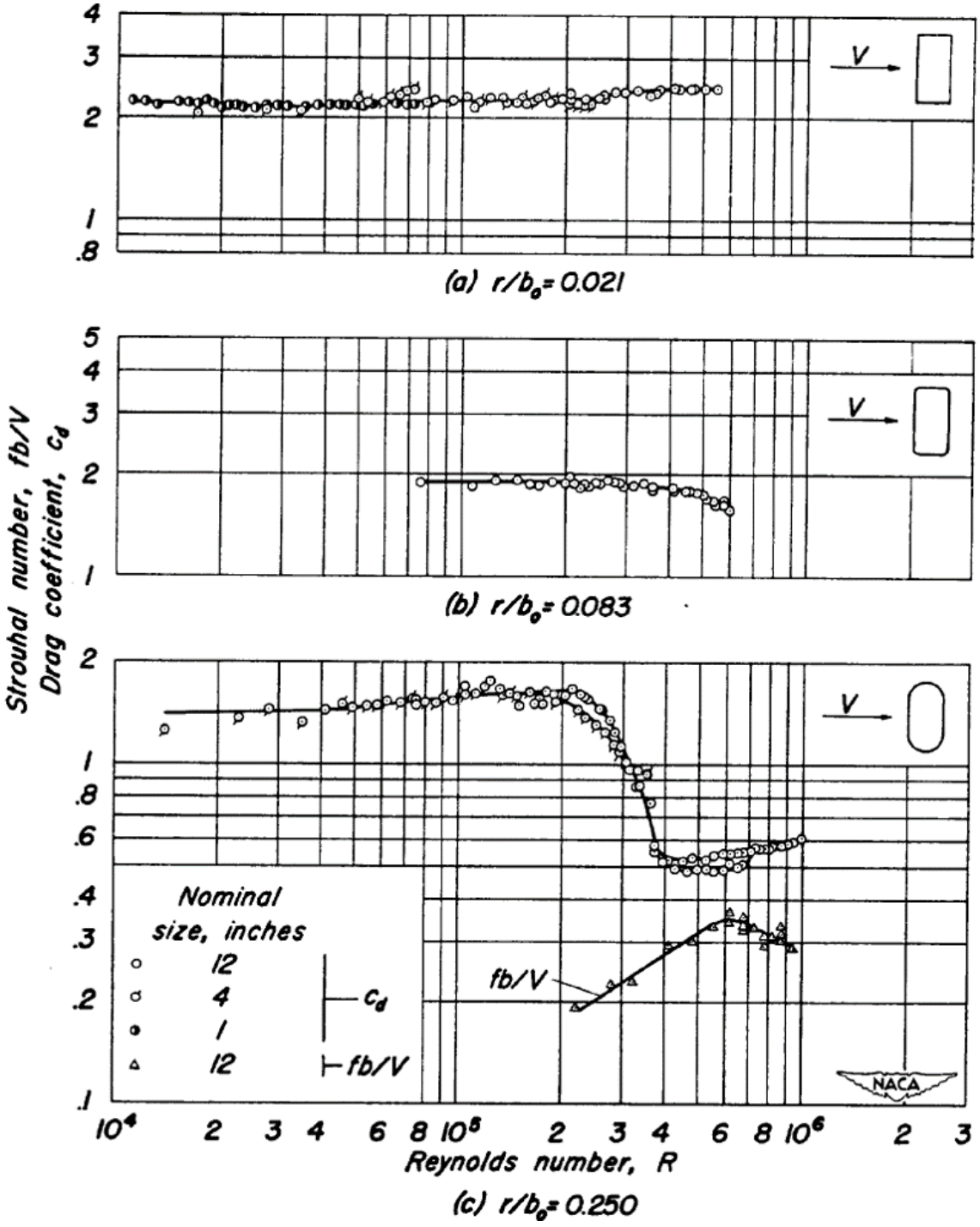

Figure A.2: Drag coefficient and Strouhal number variance with chord-based Reynolds number for a 1:2 rectangular cylinder

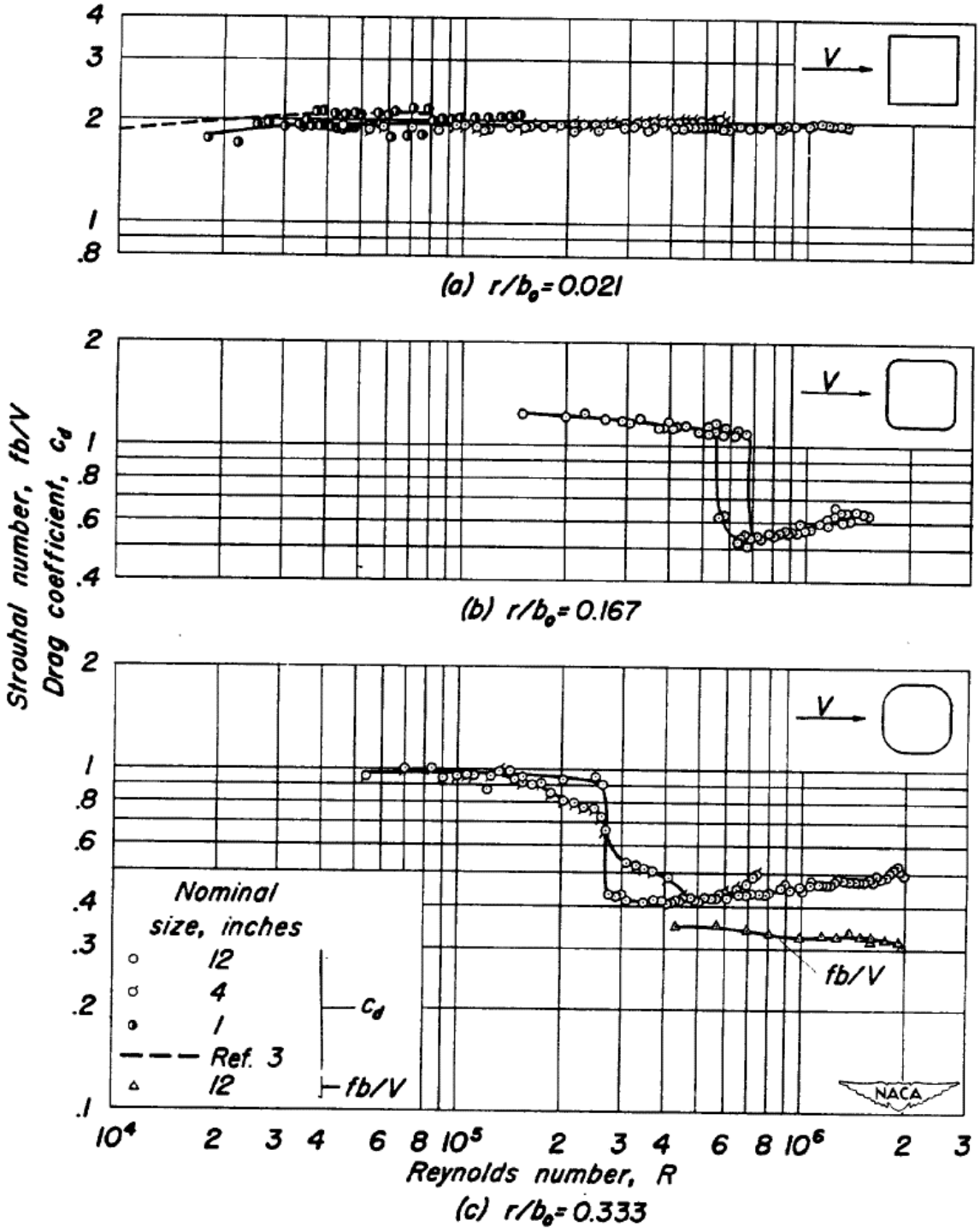

Figure A.3: Drag coefficient and Strouhal number variance with chord-based Reynolds number for a 1:1 rectangular (square) cylinder

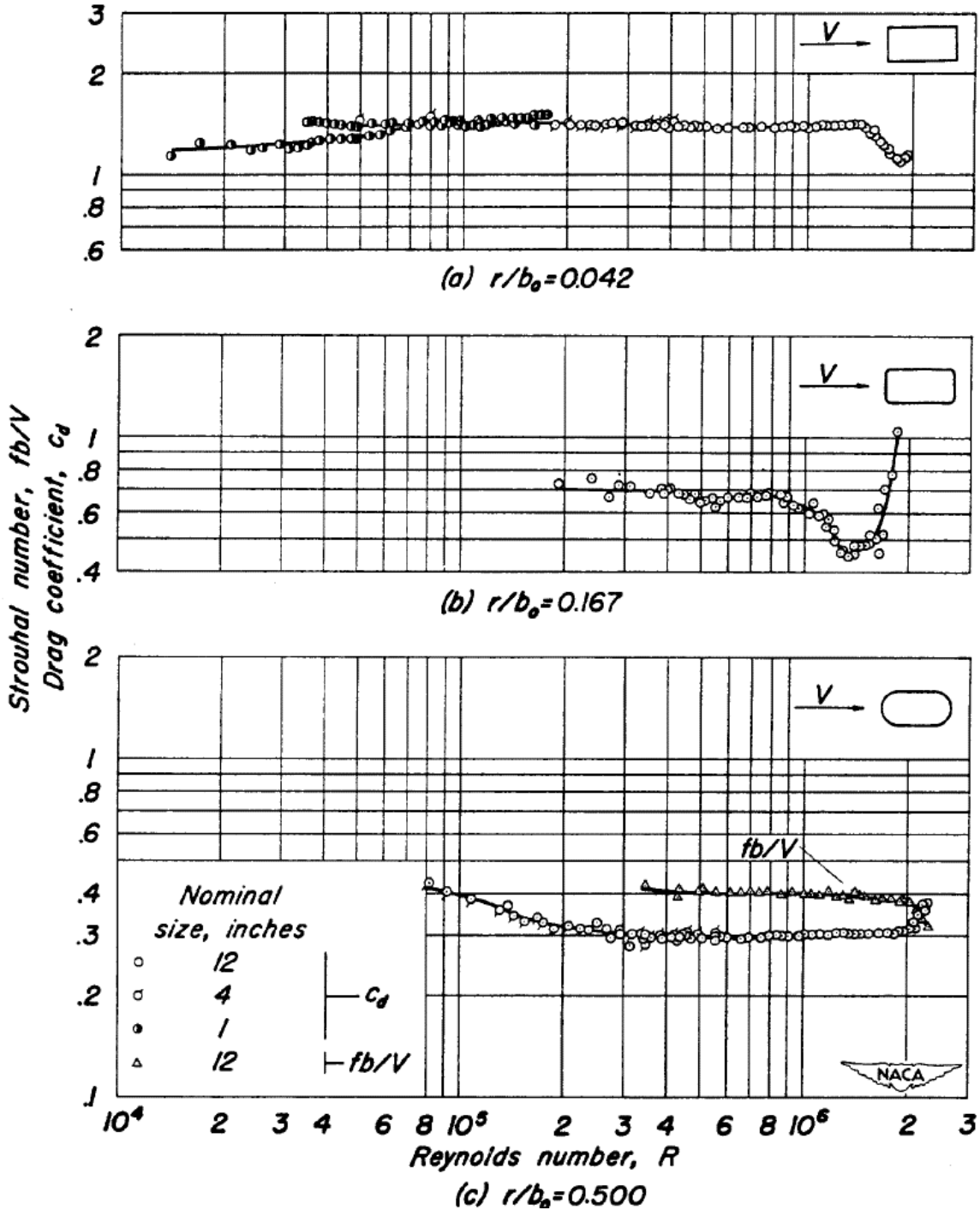

Figure A.4: Drag coefficient and Strouhal number variance with chord-based Reynolds number for a 2:1 rectangular cylinder

APPENDIX B

Mechanical Drawings of Hubs

Mechanical drawings of each of the hub models tested in the current work.

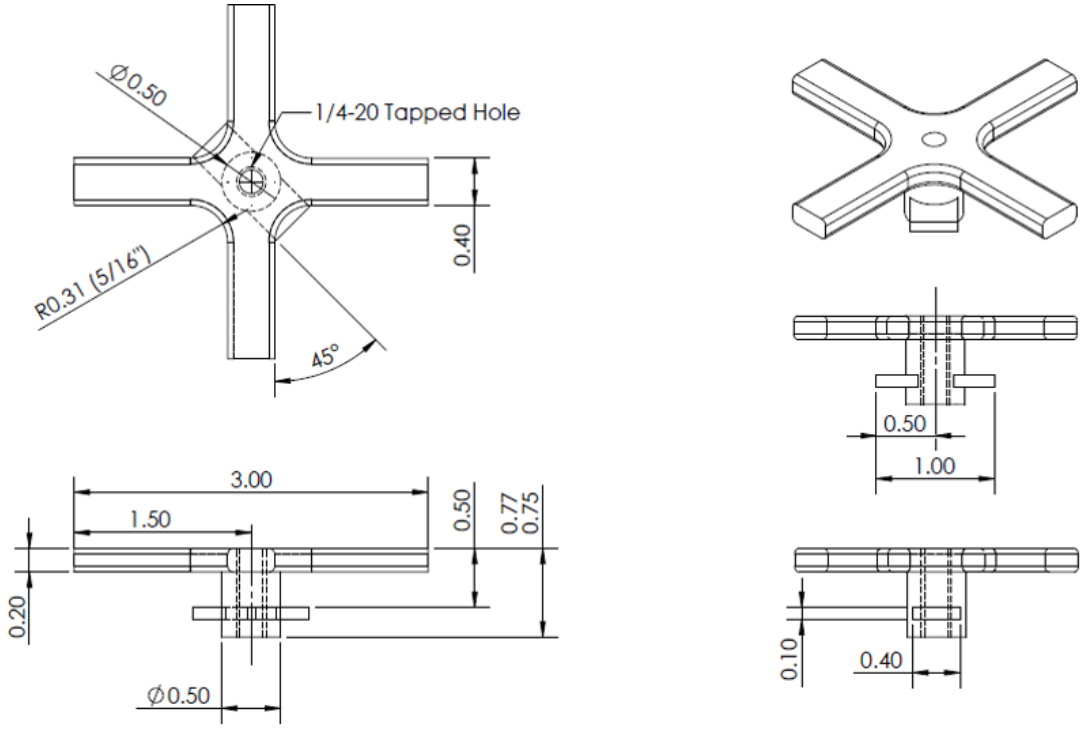

Figure B.1: Model used in preliminary tests. Scissor links are out-of-phase, and corner profile is rounded (corner radius-to-profile thickness ratio of 0.167)

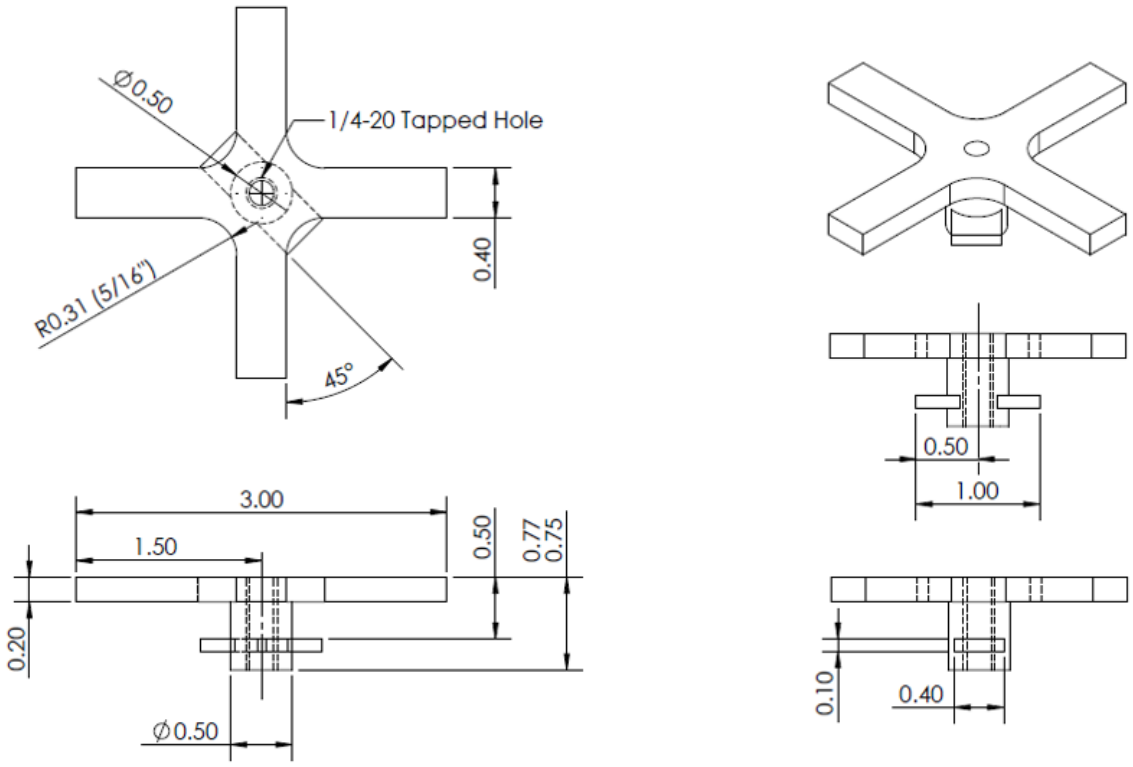

Figure B.2: Model used in final tests. Scissor links are out-of-phase, and corner profile is sharp

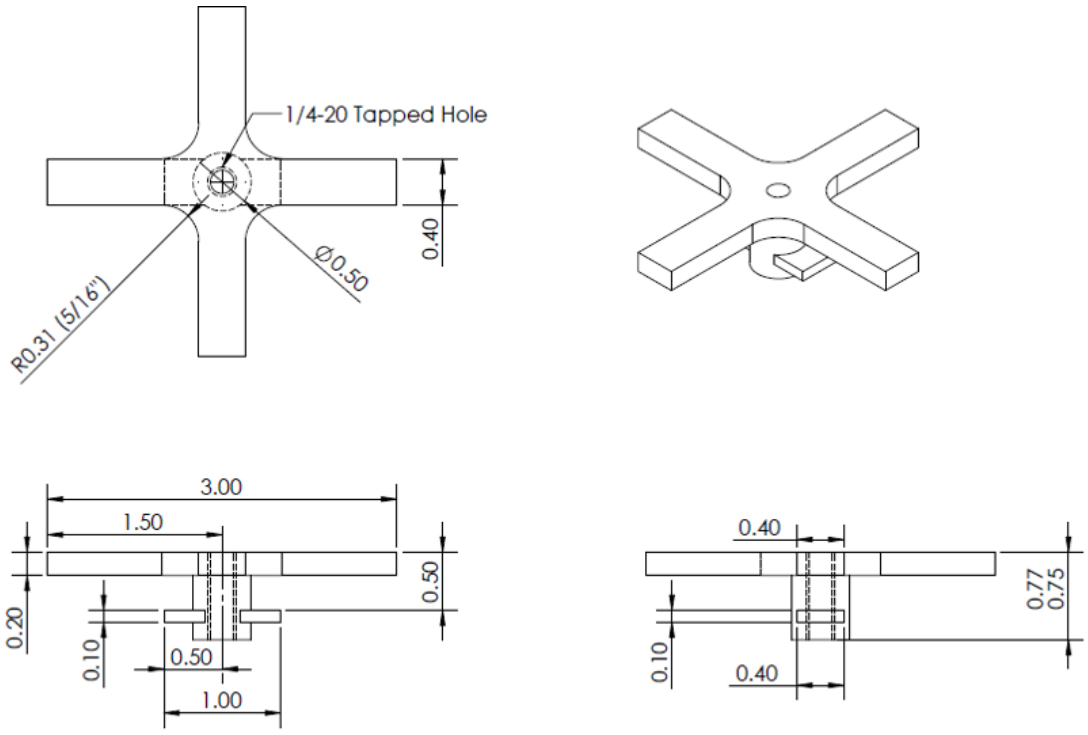

Figure B.3: Model used in final tests. Scissor links are in-phase, and corner profile is sharp

APPENDIX C

Preliminary Testing Velocity Spectra

A collection of velocity spectra at each grid location from the preliminary, time-resolved testing.

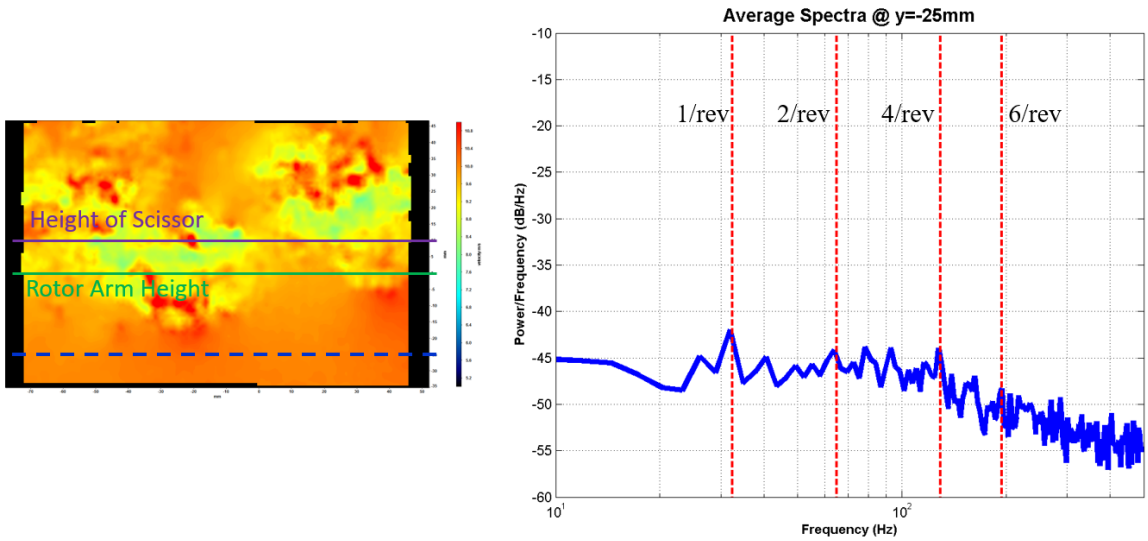

Figure C.1: Velocity Magnitude Spectra at y = -25 mm

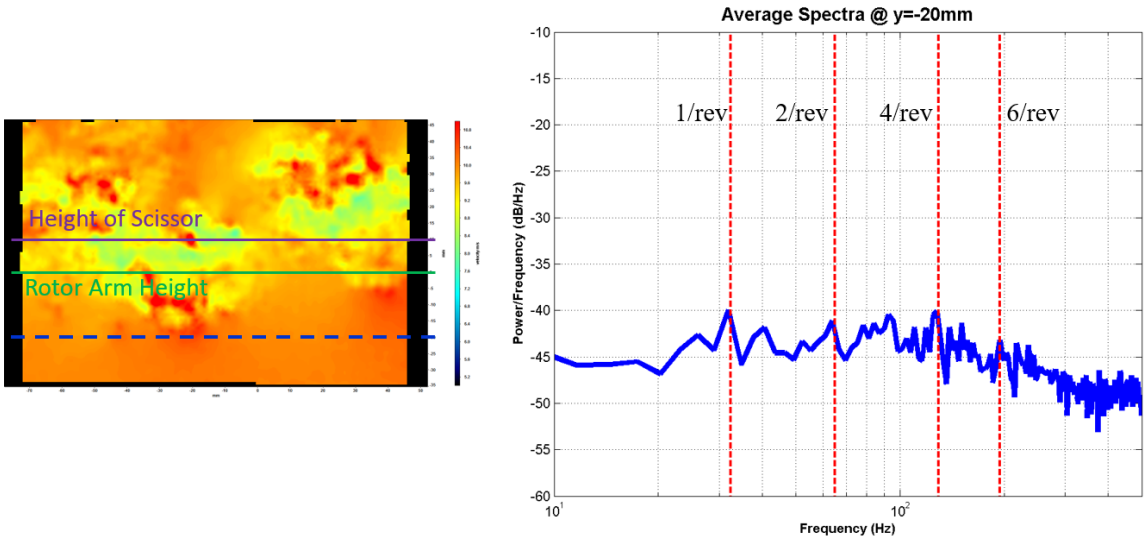

Figure C.2: Velocity Magnitude Spectra at y = -20 mm

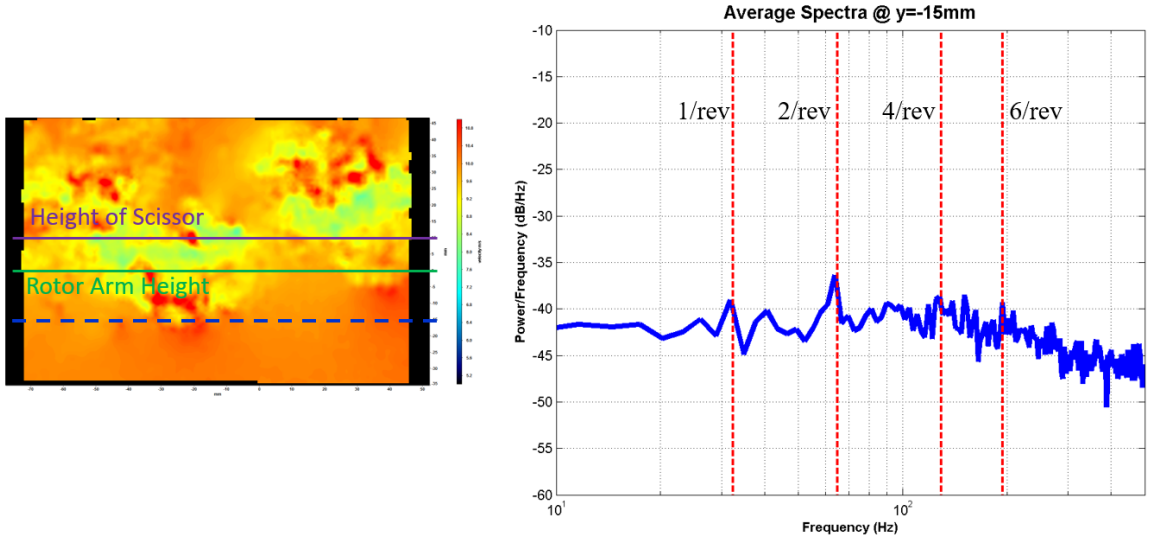

Figure C.3: Velocity Magnitude Spectra at y = -15 mm

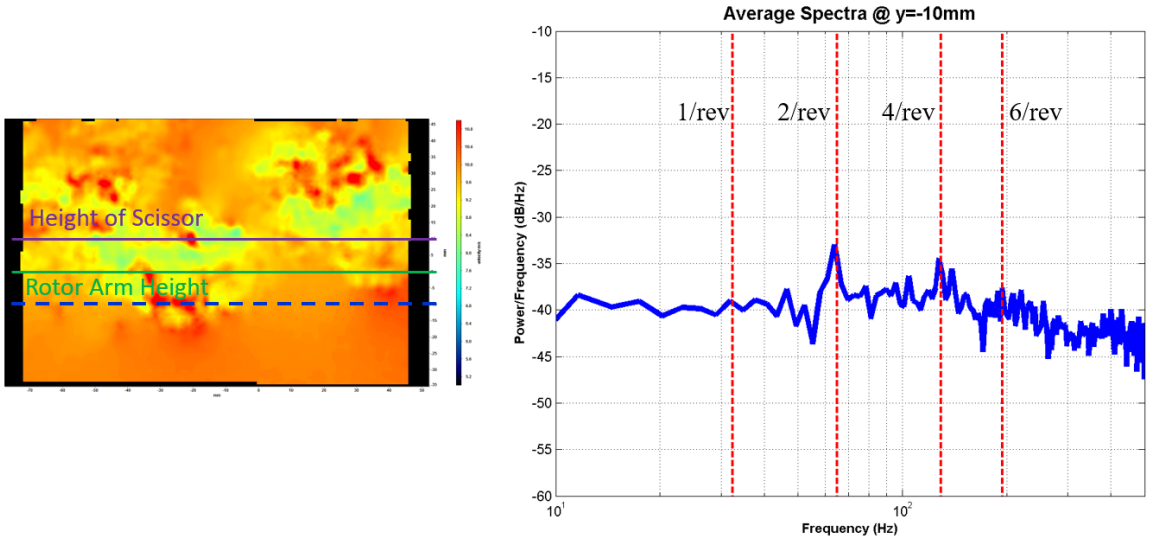

Figure C.4: Velocity Magnitude Spectra at y = -10 mm

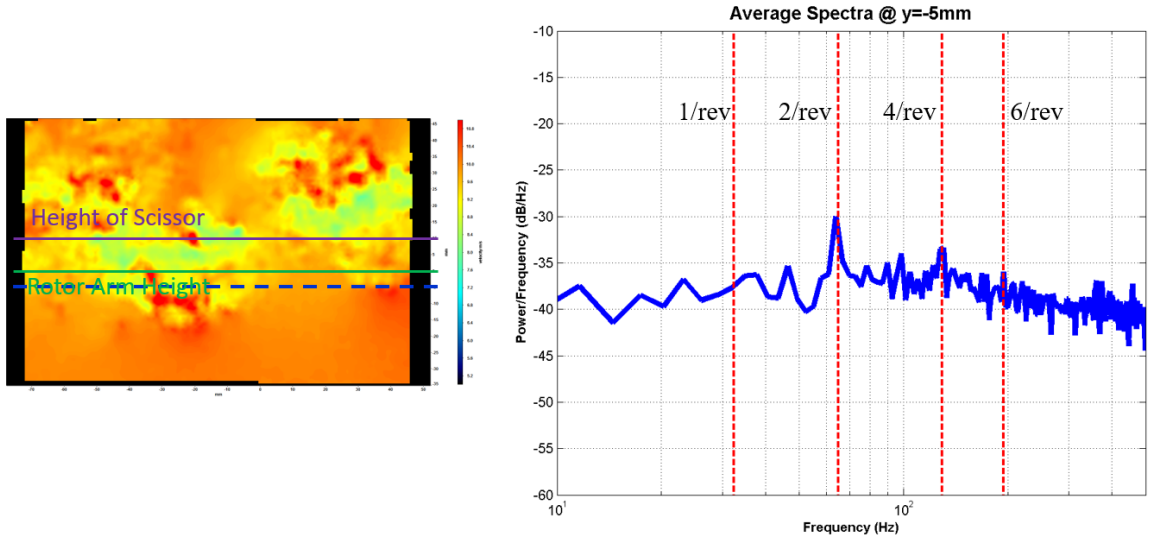

Figure C.5: Velocity Magnitude Spectra at y = -5 mm

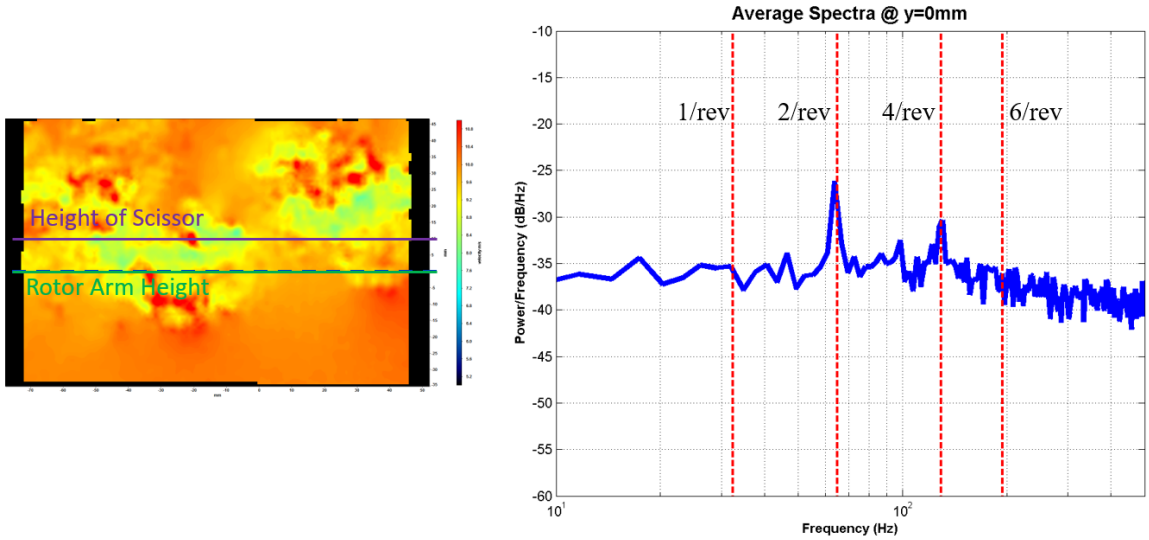

Figure C.6: Velocity Magnitude Spectra at y = 0 mm

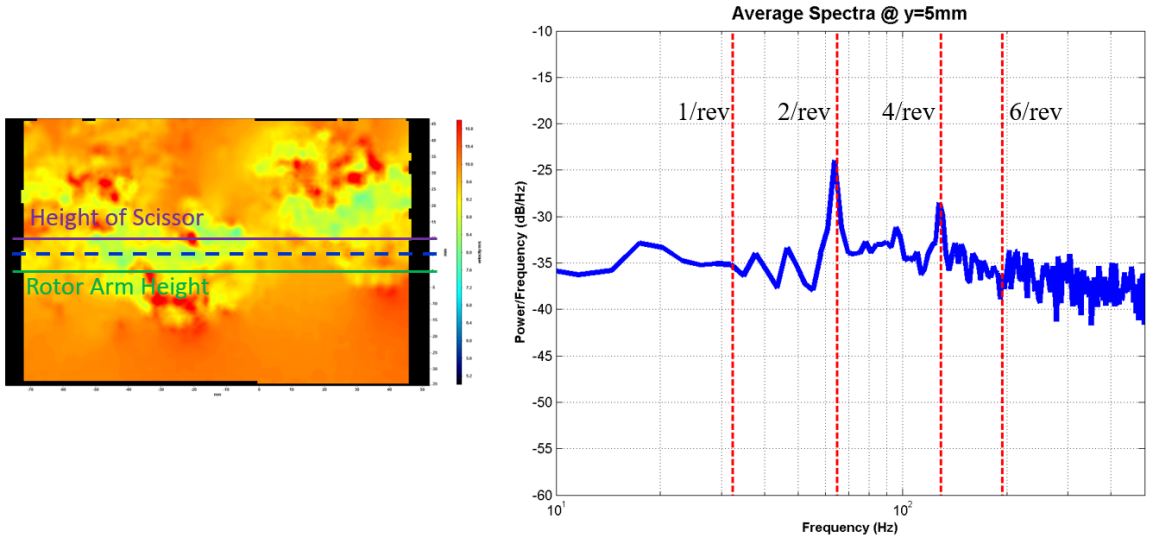

Figure C.7: Velocity Magnitude Spectra at y = +5 mm

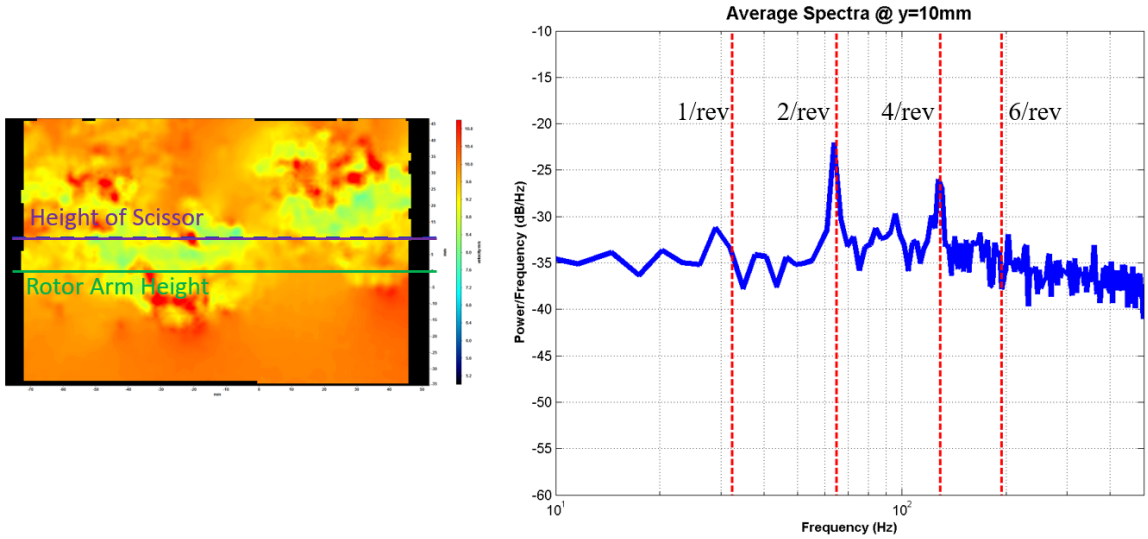

Figure C.8: Velocity Magnitude Spectra at y = +10 mm (Scissor Link Height)

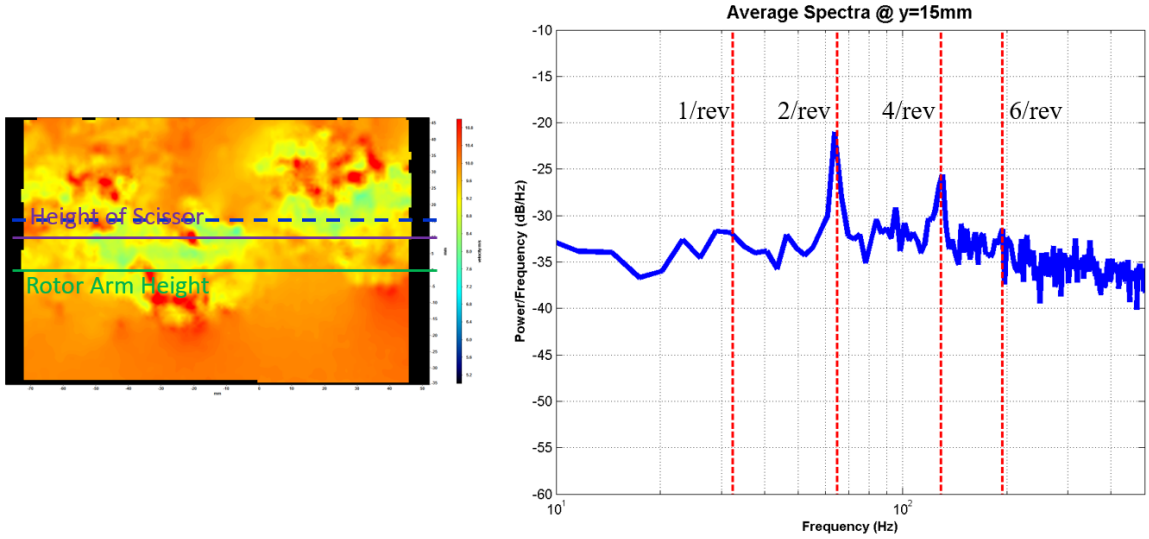

Figure C.9: Velocity Magnitude Spectra at y = +15 mm

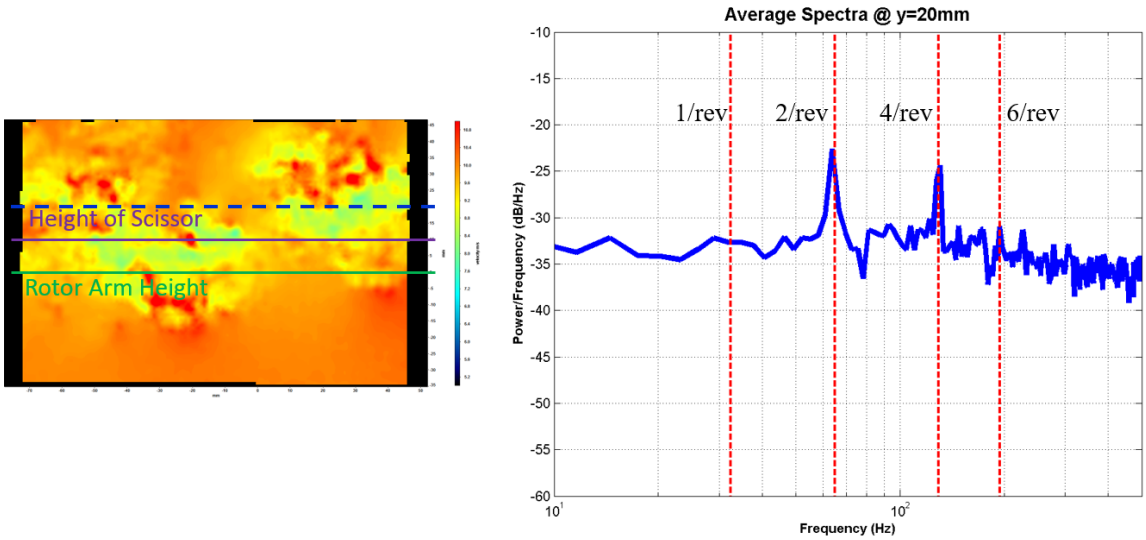

Figure C.10: Velocity Magnitude Spectra at y = +20 mm

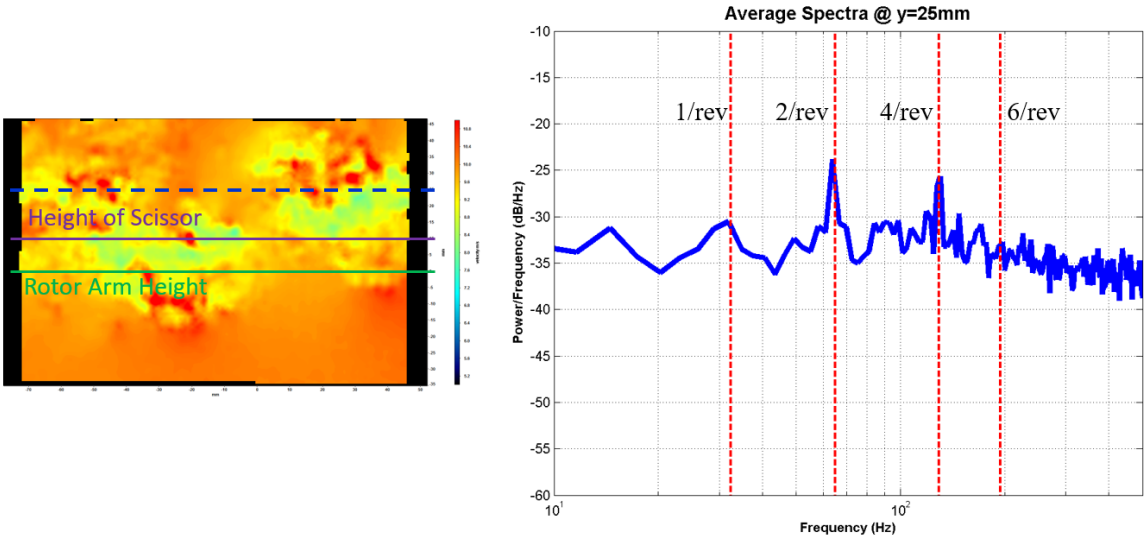

Figure C.11: Velocity Magnitude Spectra at y = +25 mm

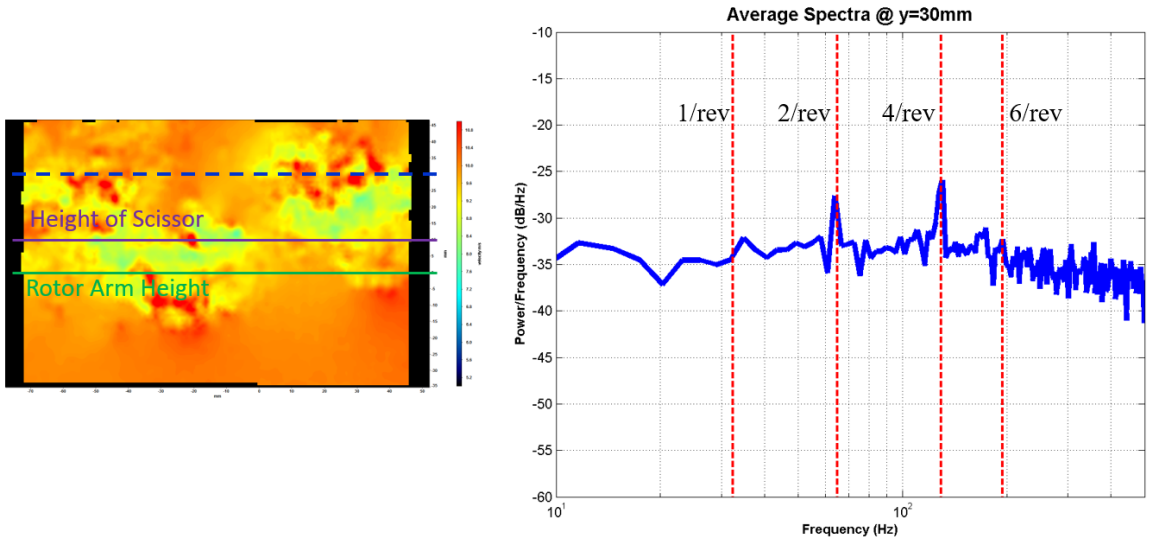

Figure C.12: Velocity Magnitude Spectra at y = +30 mm

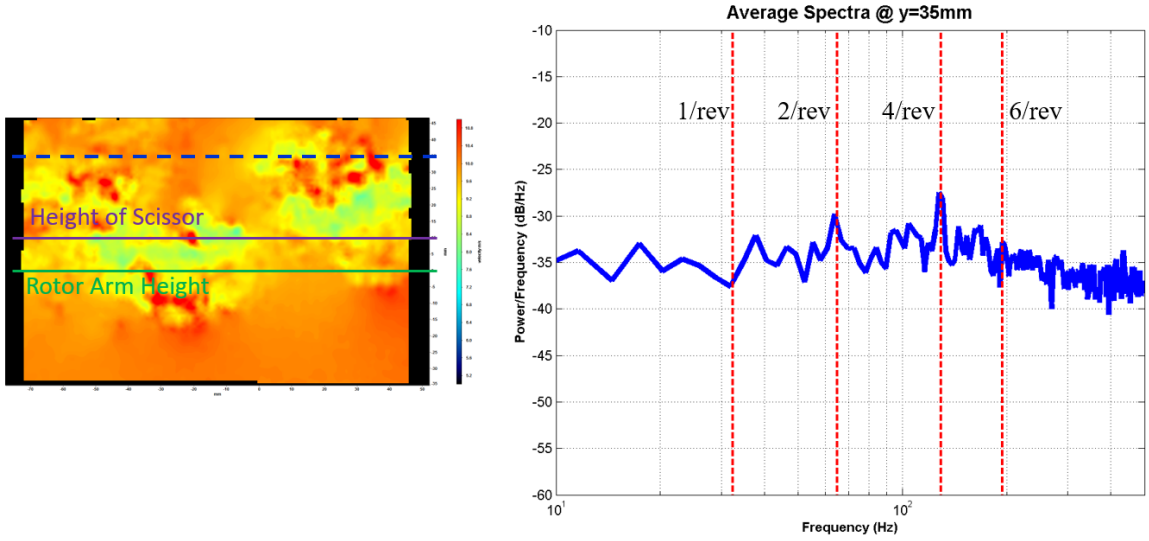

Figure C.13: Velocity Magnitude Spectra at y = +35 mm

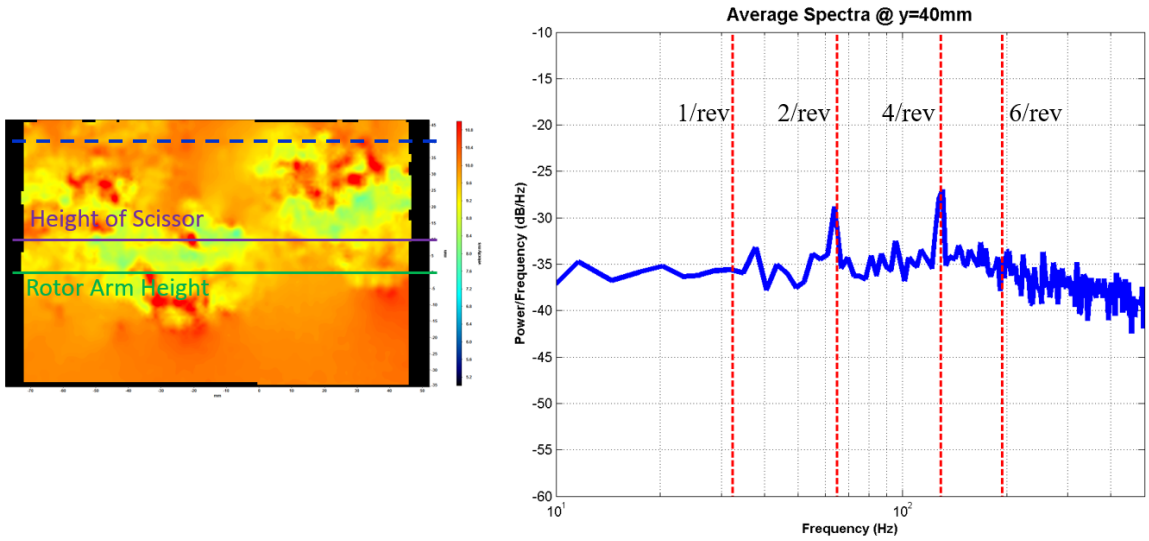

Figure C.14: Velocity Magnitude Spectra at y = +40 mm

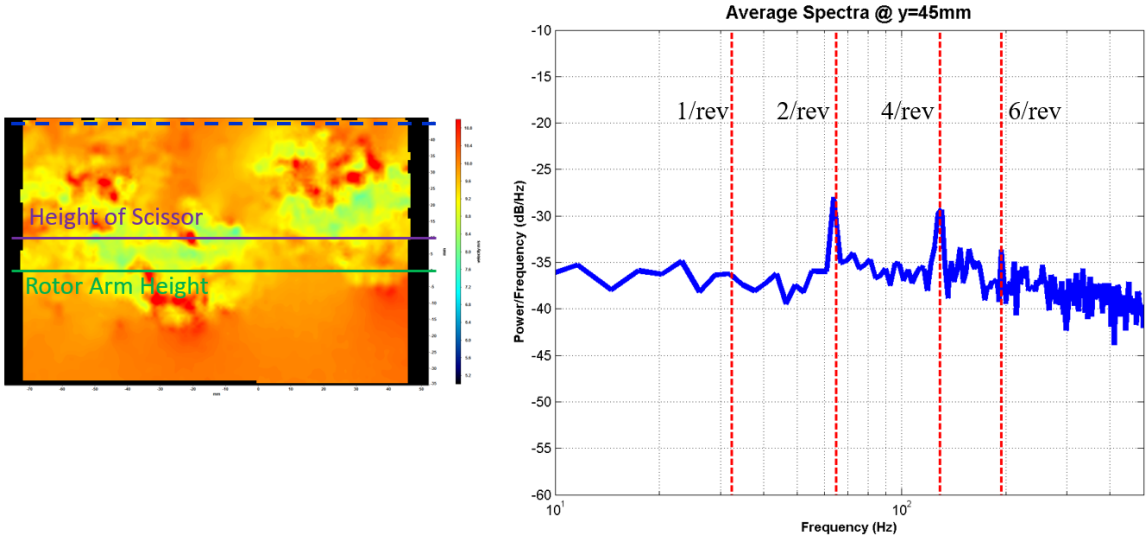

Figure C.15: Velocity Magnitude Spectra at y = +45 mm

BIBLIOGRAPHY

[1] C. N. Keys and R. Wiesner, "Guidelines for reducing helicopter parasite drag," *Journal of the American Helicopter Society*, vol. 20, no. 1, pp. 80–88, 1975.

[2] T. W. Sheehy, "A general review of helicopter rotor hub drag data," *Journal of the American Helicopter Society*, vol. 22, no. 2, pp. 2–10, 1977.

[3] J. P. Rabbott and R. H. Stroub, "Wasted fuel - another reason for drag reduction," in *31st American Helicopter Society National Forum*, (Washington, DC), March 6-7 1975.

[4] P. Roesch and A.-M. Dequin, "Experimental research on helicopter fuselage and rotor hub wake turbulence," *Journal of the American Helicopter Society*, vol. 30, pp. 43–51, January 1985.

[5] J. O. Bridgeman and G. T. Lancaster, "Physics-based analysis methodology for hub drag prediction," in *American Helicopter Society 66th Annual Forum*, (Phoenix, AZ), American Helicopter Society, May 11-13 2010.

[6] M. Dombroski and T. A. Egolf, "Drag prediction of two production rotor hub geometries," in *American Helicopter Society 68th Annual Forum*, (Fort Worth, TX), American Helicopter Society, May 11-13 2010.

[7] R. Shenoy, M. Holmes, M. J. Smith, and N. M. Komerath, "Scaling evaluations on the drag of a hub system," *Journal of the American Helicopter Society*, vol. 58, p. 032002, 2013.

[8] V. Raghav, R. Shenoy, M. Smith, and N. Komerath, "Investigation of drag and wake turbulence of a rotor hub," *Aerospace Science and Technology*, vol. 28, pp. 164–175, 2013.

[9] D. Reich, R. Shenoy, M. Smith, and S. Schmitz, "A review of 60 years of rotor hub drag and wake physics: 19542014," *Journal of the American Helicopter Society*, vol. 61, no. 2, p. 022007, 2016.

[10] J. D. Berry, "Measurements taken behind a model helicopter rotor hub in forward flight," Tech. Rep. TM-4738, NASA, 1997.

[11] J. D. Berry, "Description of the u.s. army small-scale 2-meter rotor test system," Tech. Rep. TM-87762, NASA, February 1987.

[12] D. Reich, B. R. Elbing, C. R. Berezin, and S. Schmitz, "Water tunnel flow diagnostics of wake structures downstream of a model helicopter rotor hub," vol. 59, p. 032001, 2014.

[13] D. Reich, R. Shenoy, S. Schmitz, and M. J. Smith, "An assessment of the long-age unsteady rotor hub wake physics for empennage analysis," in *American Helicopter Society 70th Annual Forum*, (Montréal, Québec), The American Helicopter Society, May 20-22 2014.

[14] D. Reich, "Water tunnel experiments on a model scale helicopter rotor hub," Master's thesis, The Pennsylvania State University, University Park, Pennsylvania, December 2013.

[15] D. Reich, S. Willits, and S. Schmitz, "Effects of reynolds number and advance ratio on the drag of a model helicopter rotor hub," in *American Helicopter Society 71st Annual Forum*, (Virginia Beach, Virginia), The American Helicopter Society, 2015.

[16] A. Roshko, "Perspectives on bluff body aerodynamics," *Journal of Wind Engineering and Industrial Aerodynamics*, vol. 49, pp. 79–100, 1993.

[17] C. H. K. Williamson, "Advances in our understanding of vortex dynamics in bluff body wakes," *Journal of Wind Engineering and Industrial Aerodynamics*, vol. 69, pp. 3–32, 1997.

[18] N. K. Delany and N. E. Sorensen, "Low-speed drag of cylinders of various shapes," Tech. Rep. TN 3038, NASA, 1953.

[19] W. C. Shih, C. Wang, D. Coles, and A. Roshko, "Experiments on flow past rough circular cylinders at large reynolds numbers," *Journal of Wind Engineering and Industrial Aerodynamics*, vol. 49, pp. 351–368, 1993.

[20] A. Fage and J. H. Warsap, "The effects of turbulence and surface roughness on the drag of a circular cylinder," Tech. Rep. TM-1283, NACA, 1929.

[21] Y. Nakamura, "Bluff-body aerodynamics and turbulence," *Journal of Wind Engineering and Industrial Aerodynamics*, vol. 49, pp. 65–78, 1993.

[22] A. Roshko, "Experiments on the flow past a circular cylinder at very high reynolds number," *Journal of Fluid Mechanics*, vol. 10, no. 3, pp. 345–356, 1961.

[23] A. Okajima, "Strouhal numbers of rectangular cylinders," *Journal of Fluid Mechanics*, vol. 123, pp. 379–398, 1982.

[24] C. Norberg, "Flow around rectangular cylinders: pressure forces and wake frequencies," *Journal of Wind Engineering and Industrial Aerodynamics*, vol. 49, pp. 187–196, 1993.

[25] G. Schewe, "Reynolds-number-effects in flow around a rectangular cylinder with aspect ratio 1:5," *Journal of Fluids and Structures*, vol. 39, pp. 15–26, 2013.

[26] L. Daniel, S. Mohaheghian, D. Dunlap, E. Ruhlmann, and B. R. Elbing, "Design of a recirculating water tunnel for the study of high-reynolds number turbulent boundary layers," in *Proceedings of the ASME 2015 Int. Mech. Eng. Congress and Expo.*, (Houston, TX), November 13-19 2015.

[27] Y. Farsiani and B. R. Elbing, "Characterization of the custom-designed, high reynolds number water tunnel," in *Proceedinsgs of the ASME 2016 Fluids Eng. Div. Summer Meeting*, (Washington, DC), July 10-14 2016.

[28] S. F. Hoerner, *Fluid Dynamic Drag: Practical Information on Aerodynamic Drag and Hydrodynamic Resistance*. Sighard F. Hoerner, 2nd ed., Jun 1965.

[29] G. I. Taylor, "The spectrum of turbulence," *Proc. of the Royal Society of London A: Mathematical, Physical and Engineering Sciences*, vol. 164, pp. 476–490, February 1938.

[30] S. B. Pope, *Turbulent Flows*. Cambridge University Press, New York: Cambridge University Press, 1 ed., 2000.

VITA

Christopher E. Petrin

Candidate for the Degree of

Master of Science

Thesis: FREQUENCY CONTENT IN THE WAKES OF ROTATING BLUFF BODY HELICOPTER HUB MODELS

Major Field: Mechanical and Aerospace Engineering

Biographical:

Personal Data: Born in Stillwater, Oklahoma on March 16th, 1993.

Education:

Completed the requirements for the degree of Bachelors of Science with a major in Mechanical and Aerospace Engineering at Oklahoma State University, Stillwater, Oklahoma in May 2014.